3 GHz Yb-Fiber Laser Based Femtosecond Sources and Frequency Comb

by

Hung-Wen Chen

B.S., Physics, National Taiwan University, 2004
M.S., Electro-Optical Engineering, National Taiwan University, 2006

Submitted to the Department of Electrical Engineering and Computer Science
in partial fulfillment of the requirements for the degree of

Doctor of Philosophy in Electrical Engineering and Computer Science

at the

MASSACHUSETTS INSTITUTE OF TECHNOLOGY

June 2014

Signature redacted

Author.....
Hung-Wen Chen
Department of Electrical Engineering and Computer Science
April 29th, 2014

Signature redacted

Certified by.....
Franz X. Kärtner
Professor of Electrical Engineering
Thesis Supervisor

Signature redacted

Certified by.....
Erich P. Ippen
Elihu Thomson Professor of Electrical Engineering, Professor of Physics
Thesis Supervisor

Signature redacted

Accepted by.....
Leslie A. Kolodziejski
Professor of Electrical Engineering
Chair, Department Committee on Graduate Theses

3 GHz Yb-Fiber Laser Based Femtosecond Sources and Frequency Comb

by

Hung-Wen Chen

Submitted to the Department of Electrical Engineering and Computer Science
on April 29th, 2014,
in partial fulfillment of the requirements for the degree of
Doctor of Philosophy in Electrical Engineering and Computer Science

Abstract

Many applications require femtosecond lasers of high repetition rate. In the time domain, a higher repetition rate means more pulses in a fixed time period. For nonlinear bio-optical imaging in which photoinduced damage is caused by pulse energy rather than average power, increasing pulse repetition-rate will improve signal-to-noise ratio and reduce data acquisition time. In the frequency domain, a higher repetition rate means the comb line spacing is larger. This permits access to and manipulation of each individual comb line. Such capabilities have opened numerous frequency-domain applications including optical arbitrary waveform generation, high-speed photonic analog-to-digital conversion, and high-resolution spectroscopy.

Femtosecond optical sources in the wavelength range between 0.7 μm and 1.55 μm have found many applications such as optical coherence tomography, high speed optical sampling, photonic analog-to-digital conversion, and multi-photon spectroscopy. To date, femtosecond solid-state lasers are mainly employed in these applications. Take two most common femtosecond solid-state lasers for example: a Ti:sapphire laser can cover 0.7–1.1 μm and is useful for optical coherence tomography and multi-photon biological imaging. A Cr:forsterite laser can operate in the wavelength range 1.15–1.35 μm, an important wavelength range for multi-photon microscopy because light in this wavelength range experiences lower scattering loss and higher penetration depth for most biology samples. Nonetheless, solid-state lasers are usually expensive, bulky, and prone to misalignment. The gain crystals often requires water cooling. These disadvantages hamper their wide usage outside the lab environment. The mentioned versatile applications can be even more widespread used if we are able to make the femtosecond laser sources less expensive, flexible, and easy to maintain.

In this dissertation, 3-GHz femtosecond laser sources are demonstrated. These sources are useful for applications in optical coherence tomography, optical frequency metrology, multi-photon biological imaging, photonic analog-to-digital conversion, etc. First, a 3-GHz fundamentally mode-locked Yb-fiber laser is demonstrated with the highest rep-rate among all femtosecond Yb-fiber lasers to date. We then numerically and experimentally study the optimization of femtosecond YDFAs in order to achieve both high-quality and high-power compressed pulses in the 3 GHz high power fiber laser system. Using the 3 GHz high power femtosecond Yb-fiber laser system, a few-cycle ultrafast source at the Ti:sapphire laser wavelength is demonstrated as a promising substitute of multi-GHz mode-locked Ti:sapphire lasers. In addition, a watt-level, femtosecond

Raman soliton source wavelength-tunable from 1.15 μm to 1.35 μm is implemented. Such a Raman soliton source exhibits both the highest repetition rate and highest average power to the best of our knowledge. Finally, preliminary work on a 3 GHz passive frequency comb via difference frequency generation at 1.5 μm is demonstrated. This is currently the highest rep-rate frequency comb in the telecommunication wavelength range.

Thesis Supervisor: Franz X. Kärtner
Title: Professor of Electrical Engineering

Thesis Supervisor: Erich P. Ippen
Title: Elihu Thomson Professor of Electrical Engineering, Professor of Physics

Acknowledgements

First of all, I would like to express my profound gratitude to my advisor Prof. Franz Kärtner for offering me the golden opportunity to be in OQE group. During my PhD career, he gave me a lot of freedom in research and was open-minded to my ideas and opinions. Whenever I faced challenges of any kind, he always provided invaluable suggestions. His exemplary guidance and encouragement constantly supported me so that I could accomplish many which I once thought impossible. I believe that his words will carry me a long way in my journey of life.

Also, I would like to thank Prof. Erich Ippen and Prof. Fujimoto for their precious time and all the advice, especially Prof. Fujimoto from whom I learned a lot as the 6.634 teaching assistant in my last semester. On his own feet, he showed me the importance of making contribution to the society and his respectable attitude toward education. While working with him, I had seen him spending enormous amount of time on the students and the course, which I truly admire.

I received so much help from many people, particularly those in OQE group. Every OQE member was always friendly and helpful when I encountered problems either in my research or daily life. I sincerely appreciate their assistance. Largely I would like to thank Dr. Guoqing Noah Chang who led me into the field of fiber laser technology. He played a very important role in my PhD life. He was not only a mentor to me but also a best friend of mine. His office door was always open for me. I could drop by his office and interrupt at any time when I had anything that I wanted to discuss with him. He was always willing to spare his time for me and to generously share his experiences and knowledge in any aspects. His mentoring and friendship made my PhD life pleasant and stress-free. The enjoyable moments we created together in his office will permanently exist in my heart. Moreover, I would like to thank for Jinkang Lim's help while we worked on the 3 GHz Yb-fiber laser system, and Duo Li's help while we worked closely on my last project, EPHI. Special thanks to the astro-comb team at Harvard University for letting me participate in one of the coolest projects in the world.

I also want to thank all the members in Republic of China (Taiwan) student association, mainly those in OQE group (Li-Jin Chen, Tsung-Han Tsai, Shu-Wei Huang, Chien-Jen Lai, Hsiang-Chieh Lee, and Jonathan Liu). Life in Boston was even more colorful with their company. Deeply I would like to convey my thankfulness to Li-Jin Chen who has helped me tremendously since the first day I got to know him. Many thanks to Prof. Chi-Kuang Sun, my former advisor at National Taiwan University, for the training and support before I came to the US.

Last but not least, I would like to greatly thank my dear family—my parents, Fu-Tien Chen and Nien-Yun Lin, my siblings, Yu-Chen Chen and Chiu-Ling Chen, and my wife, Ya-Hui Chang. Without their substantial backing up, I would not have gotten as far as I have. Mostly I'd like to thank my dearest wife, my soul mate, Ya-Hui. No matter what difficulties I face, she is always by my side. When I got the MIT admission, she was willing to give up her high salary and life in Taiwan and came to the US with me. I would say at least half of my PhD degree should belong to her. My appreciation toward my family is way beyond words. For that reason, I would like to dedicate this thesis to them and also to our incoming baby girl, Evelyn Chen.

Publication List

Referred Journal Publications

[1] J. Lim, **H.-W. Chen**, S. Xu, Z. Yang, F. X. Kärtner, and G. Chang, "3 GHz, Watt-level femtosecond Raman soliton source," Opt. Lett. 39, 2060-2063, 2014.

[2] **H.-W. Chen**, H. Zia, J. Lim, S. Xu, Z. Yang, F. X. Kärtner, and G. Chang, "3 GHz, Yb-fiber laser based, few-cycle ultrafast source at the Ti:sapphire laser wavelength," Opt. Lett. 38, 4927-4930, 2013. (**Top of Downloads in November 2013**)

[3] J. Lim, **H.-W. Chen**, G. Chang, and F. X. Kärtner, "Frequency comb based on a narrowband Yb-fiber oscillator: pre-chirp management for self-referenced carrier envelope offset frequency stabilization," Opt. Express 21, 4531-4538, 2013.

[4] **H.-W. Chen**, J. Lim, S.-W. Huang, D. N. Schimpf, F. X. Kärtner, and G. Chang, "Optimization of femtosecond Yb-doped fiber amplifiers for high-quality pulse compression," Opt. Express 20, 28672-28682, 2012.

[5] **H.-W. Chen**, G. Chang, S. Xu, Z. Yang, and F. X. Kärtner, "3 GHz, fundamentally mode-locked, femtosecond Yb-fiber laser," Opt. Lett. 37, 3522-3524, 2012.

[6] **H.–W. Chen**, T. Sosnowski, C.–H. Liu, L.-J. Chen, J. Birge, A. Galvanauskas, F. X. Kärtner, and G. Q. Chang, "Chirally-coupled-core Yb-fiber laser delivering 80-fs pulses with diffraction-limited beam quality warranted by a high-dispersion-mirror based compressor," Opt. Express 18, 24699, 2010.

[7] C.-M. Chiu, **H.-W. Chen**, Y.-R. Huang, Y.-J. Hwang, W.-J. Lee, H.-Y. Huang, and C.-K. Sun, "All-THz fiber-scanning near-field microscopy," Opt. Lett. 34, pp. 1084-1086, 2009.

[8] **H.-W. Chen**, C.-M. Chiu, J.-L. Kuo, P.-J. Chiang, H.-C. Chang, and C.-K. Sun, "Subwavelength dielectric-fiber-based terahertz coupler," J. Light. Technol. 27, 1489-1495, 2009.

[9] C.-H. Lai, Y.-C. Hsueh, **H.-W. Chen**, Y.-J. Huang, H.-C. Chang and C.-K. Sun, "Low-Index Terahertz Pipe Waveguides," Opt. Lett. 34, 3457-3459, 2009.

[10] J.-Y. Lu, C.-C. Kuo, C.-M. Chiu, **H.-W. Chen**, Y.-J. Hwang, C.-L. Pan, and C.-K. Sun, "THz interferomertric imaging using subwavelength plastic fiber based THz endoscope," Opt. Express 16, 2494-2501, 2008.

[11] J.-Y. Lu, C.-P. Yu, H.-C. Chang, **H.-W. Chen**, Y.-T. Li, C.-L. Pan, and C.-K. Sun, "THz Air-core Microstructure Fiber," Appl. Phys. Lett. 92, 064105, 2008.

[12] **H.-W. Chen**, Y.-T. Li, J.-L. Kuo, J.-Y. Lu, L.-J. Chen, C.-L. Pan, and C.-K. Sun, "Investigation on Spectral Loss Characteristics of Subwavelength Terahertz Fibers," Optics Lett. 32, 1017-1019, 2007.

[13] L.-J. Chen, **H.-W. Chen**, T.-F. Kao, J.-Y. Lu, and C.-K. Sun, "Low-loss Subwavelength Plastic Fiber for Terahertz Wave Guiding," Opt. Lett. 31, 308-310, 2006.

[14] J.-Y. Lu, L.-J. Chen, T.-F. Kao, H.-H. Chang, **H.-W. Chen**, A.-S. Liu, Y.-C. Chen, R.-B. Wu, W.-S. Liu, J.-I. Chyi, and C.-K. Sun, "Terahertz microchip for illicit drug detection," IEEE Photon. Technol. Lett. 18, 2254-2256, 2006.

Referred Conference Proceedings

[1] **H.-W. Chen**, J. Lim, S. Xu, Z. Yang, F. X. Kärtner, Guoqing Chang, "3-GHz, ultrafast Yb-fiber laser sources: filling spectral gap," SPIE Optical Engineering and Applications, manuscript in preparation. (**Invited**)

[2] **H.-W. Chen**, H. Zia, J. Lim, S. Xu, Z. Yang, and F. X. Kärtner, "3 GHz few-cycle ultrafast source at 850nm," in Frontiers in Optics 2013/Laser Science XXIX, OSA Technical Digest (CD) (Optical Society of America, 2013), FW6B.2. (**Postdeadline**)

[3] **H.-W. Chen**, J. Lim, S. Xu, Z. Yang, and F. X. Kärtner, "Yb-Fiber Oscillator Based, Few-Cycle Ultrafast Source At 850nm," in the 10th Conference on Lasers and Electro-Optics Pacific Rim and the 18th OptoElectronics and Communications Conference/Photonics in Switching 2013 (CLEO-PR & OECC/PS2013), CM2I.4. (**Best Paper Award**).

[4] **H.-W. Chen**, G. Chang, C. Zhu, X. Ma, A. Galvanauskas, and F. X. Kärtner, "Air-clad chirally-coupled-core Yb-fiber femtosecond oscillator with >10W average power," EPJ Web Conf. 41, 10006 (2013).

[5] **H.-W. Chen**, G. Chang, S.-W. Huang, D. N. Schimpf, and F. X. Kärtner, "High-quality pulse-compression of pre-chirped pulses in fiber-amplifiers," in 2012 Conference on Lasers and Electro-Optics (CLEO) (2012), CM4N.3.

[6] **H.-W. Chen**, T. Sosnowski, C.-H. Liu, L.-J Chen, J. R. Birge, A. Galvanauskas, F. X. Kärtner, and G. Q. Chang, "High-energy chirally-coupled-core Yb-fiber laser with high dispersion mirror compressor to achieve 1W-level, sub-100fs pulses with diffraction-limited beam quality," paper ATuC5, Advanced Solid-State Photonics (ASSP), Istanbul, Turkey, 2011.

[7] **H.-W. Chen**, C.-M. Chiu, Y.-R. Huang, C.-C. Kuo, Y.-J. Huang, W.-J. Lee, C.-K. Sun, "THz Subwavelength-Fiber-based Near-Field Microscope," CLEO/IQEC, paper CWM2, Baltimore, MD, U.S.A, 2009.

[8] **H.-W. Chen**, C.-M. Chiu, Y.-R. Huang, C.-C. Kuo, Y.-J. Huang, and C.-K. Sun, "Identifying Breast Cancer Section using a Fiber-Scanning Near-Field THz Microscope," in Conference Proceedings of International Conference on Optics and Photonics in Taiwan (OPT'08), paper Fri-P1-198, Taipei, Taiwan, 2008.

[9] **H.-W. Chen**, J.-Y. Lu, L.-J. Chen, P.-J. Chiang, H.-C. Chang, Y.-T. Li, C.-L. Pan, and C.-K. Sun, "THz Fiber Directional Coupler," Conference on Lasers and Electro-Optics/Quantum Electronics and Laser Science Conference/Conference on Photonic Applications, paper CThLL7, Baltimore, MD, USA, 2007.

[10] **H.-W. Chen**, J.-Y. Lu, L.-J. Chen, Y.-T. Li, C.-L. Pan, and C.-K. Sun, "Spectral Loss Characteristics of Subwavelength THz Fibers," Conference on Lasers and Electro-Optics/Quantum Electronics and Laser Science Conference/Conference on Photonic Applications, paper CJWA107, Baltimore, MD, US, 2007.

[11] **H.-W. Chen**, J.-Y. Lu, J.-L. Kuo, Y.-T. Li, C.-L. Pan, L.-J. Chen, and C.-K. Sun, "Study on attenuation spectrum of subwavelength-diameter THz fiber," The 1st Asian-Pacific Workshop on THz Photonics, pp. 27-28, Hsinchu, Taiwan, 2006.

[12] **H.-W. Chen**, J.-Y. Lu, J.-L. Kuo, Y.-T. Li, C.-L. Pan, L.-J. Chen, P.-J. Chiang, H.-C. Chang, and C.-K. Sun, "THz fiber-based coupler," The 1st Asian-Pacific Workshop on THz Photonics, pp. 23-24, Hsinchu, Taiwan, 2006.

[13] D. Li, M. Peng, **H.-W. Chen**, J. Lim, M. Watts, and F. X. Kärtner, "Fiber-Optic Demonstration of Optical Frequency Division for Erbium Silicon Photonics Integrated Oscillator," in 2014 Conference on Lasers and Electro-Optics (CLEO) (2014), SF1I.3.

[14] G. Zhou, L. Wei, J. Lim, **H.-W. Chen**, F. X. Kärtner, and G. Chang, "Relative intensity noise of Raman solitons" submitted to 6th EPS-QEOD EUROPHOTON CONFERENCE 2014.

[15] L. Wei, G. Zhou, J. Lim, **H.-W. Chen**, F. X. Kärtner, and G. Chang, "Relative intensity noise of Raman solitons: which one is more noisy? " in 2014 Conference on Lasers and Electro-Optics (CLEO) (2014), SM4N.7.

[16] N. Langellier, C.-H. Li, A. Glenday, G. Furesz, G. Chang, **H.-W. Chen**, J. Lim, A. Szentgyorgyi, D. Sasselov, D. Phillips, F. X. Kärtner, and R. L. Walsworth "Broadband astrocomb at the HARPS-N spectrograph for Earth-like exoplanet searches," SPIE Astronomical Telescopes and Instrumentation Proceedings SPIE, 9147-326, 2014.

[17] G. Chang, **H.-W. Chen**, J. Lim, S. Xu, Z. Yang, and F. X. Kärtner, "3 GHz, femtosecond Raman soliton source," in 2013 Conference on Lasers and Electro-Optics (CLEO) (2013), CM2I.4.

[18] J. Lim, **H.-W. Chen**, G. Change, and F. X. Kärtner, "Stable frequency comb derived from a narrowband Yb-fiber laser: pre-chirp management for self-referenced f_{CEO} stabilization," in 2013 Conference on Lasers and Electro-Optics (CLEO) (2013), CM2I.7.

[19] J. Lim, **H.-W. Chen**, A.-L. Calendron, G. Chang, and F. X. Kärtner, "Optimization of ultrafast Yb-doped fiber amplifiers to achieve high-quality compressed pulses," EPJ Web Conf. 41, 10020 (2013).

[20] A. Glenday, C.-H. Li, N. Langellier, G. Furesz, G. Chang, **H.-W. Chen**, J. Lim, F. Kärtner, D. Phillips, A. Szentgyorgyi, and R. Walsworth, "A high accuracy FTS for laser frequency combs, lamps and other sources," in Bulletin of the American Physical Society (American Physical Society, 2013), Volume 58, Number 6.

[21] N. Langellier, A. Glenday, C.-H. Li, G. Furesz, G. Chang, **H.-W. Chen**, J. Lim, F. Kärtner, D. Phillips, A. Szentgyorgyi, and R. Walsworth, "Green Astro-comb for exoplanet searches," in Bulletin of the American Physical Society (American Physical Society, 2013), Volume 58, Number 6.

[22] D. Phillips, C.-H. Li, A. Glenday, N. Langellier, G. Furesz, G. Chang, **H.-W. Chen**, J. Lim, F. Kärtner, A. Szentgyorgyi, and R. Walsworth, "Green Astro-comb for exoplanet searches at HARPS-N," in Bulletin of the American Physical Society (American Physical Society, 2013), Volume 58, Number 6.

[23] G. Chang, C.-H. Li, A. Glenday, G. Furesz, N. Langellier, L.-J. Chen, M. W. Webber, J. Lim, **H.-W. Chen**, D. F. Phillips, A. Szentgyorgyi, R. L. Walsworth, and F. X. Kärtner, "Spectrally flat, broadband visible-wavelength astro-comb," in 2012 Conference on Lasers and Electro-Optics (CLEO) (2012), CF2C.4.

[24] Y. Zhou, G. Chang, **H.-W. Chen**, P. C. Chui, K. K.-Y. Wong, and F. X. Kärtner, "Nonlinear-polarization-evolution mode-locking in a hybrid cavity: A route toward low repetition-rate fiber lasers," in 2012 Conference on Lasers and Electro-Optics (CLEO) (2012), CF3L.3.

[25] G. Chang, **H.-W. Chen**, S. Xu, Z. Yang, and F. X. Kärtner, "2.46-GHz, fundamentally mode-locked, femtosecond Yb-fiber oscillator," in 5th EPS-QEOD EUROPHOTON CONFERENCE 2012, WeC.3.

[26] C.-H. Li, A. Glenday, N. Langellier, G. Furesz, M. Webber, G. Chang, L.-J. Chen, **H.-W. Chen**, J. Lim, F. Kärtner, D. Phillips, A. Szentgyorgyi, and R. Walsworth, "Green astro-comb for exoplanet searches," in Bulletin of the American Physical Society (American Physical Society, 2012), Volume 57, Number 5.

[27] D. Phillips, A. Glenday, C.-H. Li, G. Furesz, N. Langellier, M. Webber, G. Chang, L.-J. Chen, **H.-W. Chen**, J. Lim, F. Kärtner, A. Szentgyorgyi, and R. Walsworth, "Generation of a green astro-comb using tapered photonic crystal fibers," in Bulletin of the American Physical Society (American Physical Society, 2012), Volume 57, Number 5.

[28] A. Glenday, C.-H. Li, M. Webber, N. Langellier, G. Furesz, G. Chang, L.-J. Chen, **H.-W. Chen**, J. Lim, F. Kärtner, D. Phillips, A. Szentgyorgyi, and R. Walsworth, "Characterization of a green astro-comb using a Fourier Transform Spectrometer," in Bulletin of the American Physical Society (American Physical Society, 2012), Volume 57, Number 5.

[29] A. Szentgyorgyi, A. J. Benedick, G. Q. Chang, **H.-W. Chen**, L.-J. Chen, G. Furesz, A. Glenday, F. X. Kärtner, S. Korzennik, C.-H. Li, D. Phillips, R. L. Walsworth "Progress Toward Laser Calibration of Ultra-Precise Radial Velocity Measurements," Conf. on Astronomy of Exoplanets with Precise Radial Velocities, Penn State University, University Park, PA, USA, 2010.

[30] G. Chang, **H.-W. Chen**, T. Sosnowski, C.-H. Liu, L.- J. Chen, J. Birge, A. Galvanauskas, and F. Kärtner, "High-energy Chirally-coupled-core Yb-fiber Oscillator with High-dispersion-mirror Compressor: Generation Of ~1w, 80-fs Pulses With Diffraction-limited Beam Quality," in Frontiers in Optics 2010/Laser Science XXVI, OSA Technical Digest (CD) (Optical Society of America, 2010), PDPC3.

[31] A. J. Benedick, G. Q. Chang, **H.-W. Chen**, L.-J. Chen, G. Furesz, A. Glenday, F. X. Kärtner, S. Korzennik, C.-H. Li, A. Szentgyorgyi, D. Phillips, R. Walsworth, "Astro-comb calibration of the TRES spectrograph at visible wavelengths," Conf. on Astronomy of Exoplanets with Precise Radial Velocities, Penn State University, University Park, PA, USA, 2010.

[32] H. Chen, C.-C. Kuo, C.-Y. Chen, Y.-W. Hwang, **H.-W. Chen**, Y.-J. Hwang, and C.-K. Sun, "Attenuation Measurement of Breast Cancer in Nude Mice in Terahertz Frequency Range," 6th Asian Conference on Ultrafast Phenomena, paper P60, pp. 166-167, Taipei, Taiwan, 2010.

[33] Y.-C. Hsueh, C.-H. Lai, **H.-W. Chen**, Y-J Huang, C.-C. Chang, and C.-K. Sun, "THz Anti-Resonant Reflecting Tube Waveguide," CLEO/IQEC, paper CThQ5, Baltimore, MD, U.S.A, 2009.

[34] H. Chen, C.-C. Kuo, C.-Y. Chen, Y.-W. Hwang, **H.-W. Chen**, Y.-J. Hwang, and C.-K. Sun, "Attenuation measurement of breast cancer in nude mice in the terahertz frequency range," Proceeding of Optics and Photonics in Taiwan, paper FP022, Taipei, Taiwan, 2009.

[35] J.-Y. Lu, C.-C. Kuo, C.-M. Chiu, **H.-W. Chen**, C.-L. Pan, and C.-K. Sun, "THz interferometric imaging using subwavelength plastic fiber based THz endoscopes," Conference on Lasers and Electro-Optics/Quantum Electronics and Laser Science Conference/Conference on Photonic Applications, paper CThN5, San Jose, CA, USA, May 2008.

[36] C.-C. Kuo, C.-Y. Chen, Y.-W. Hwang, **H.-W. Chen**, Y.-J. Hwang, F.-H. Chang, and C.-K. Sun, "In-vivo measurement of THz absorption constants of the skin and xenografted colon cancer on nude

mice," in Conference Proceedings of International Conference on Optics and Photonics in Taiwan (OPT'08), paper Fri-P1-210, Taipei, Taiwan, 2008.

[37] J.-Y. Lu, **H.-W. Chen**, L.-J. Chen, and C.-K. Sun, "Sub-Wavelength THz Plastic Fibers," Photonics West, paper 6472-7, San Jose, CA, USA, 2007.

[38] J.-Y. Lu, C.-P. Yu, H.-C. Chang, **H.-W. Chen**, Y.-T. Li, C.-L. Pan, and C.-K. Sun, "Air-core microstructure fiber for terahertz radiation waveguiding," Conference on Lasers and Electro-Optics/Quantum Electronics and Laser Science Conference/Conference on Photonic Applications, paper CThLL5, Baltimore, MD, USA, 2007.

[39] C.-K. Sun, L.-J. Chen, **H.-W. Chen**, and J.-Y. Lu, "Subwavelength plastic fiber for terahertz wave guiding," Optics East/ Conference on Terahertz Physics, Devices, and Systems, paper 6373-12, Boston, MA, Oct. 2006.

[40] L.-J. Chen, **H.-W. Chen**, T.-F. Kao, J.-Y. Lu, and C.-K. Sun, "Low-loss subwavelength THz plastic fibers," Conference on Lasers and Electro-Optics/Quantum Electronics and Laser Science Conference/Conference on Photonic Applications, paper CMS1, Long Beach, CA, USA, 2006.

[41] C.-K. Sun, J.-Y. Lu, L.-J. Chen, T.-F. Kao, **H.-W. Chen**, A.-S. Liu, Y.-C. Yu, R.-B. Wu, W.-S. Liu, and J.-I. Chyi, "THz microchip for instant illicit drug identification," The 1st Asian-Pacific Workshop on THz Photonics, pp. 17-18, Hsinchu, Taiwan, 2006.

[42] J.-Y. Lu, Y.-T. Li, C.-L. Pan, C.-P. Yu, H.-C. Chang, **H.-W. Chen**, and C.-K. Sun, "Air-core microstructure fiber for terahertz radiation waveguiding," The 1st Asian-Pacific Workshop on THz Photonics, pp. 25-26, Hsinchu, Taiwan, 2006.

Patents

[1] C.-K. Sun, L.-J. Chen, and **H.-W. Chen**, "Plastic waveguide for terahertz wave," USA patent US7,409,132 B2, Aug. 2008.

[2] Y.-H. Chang and **H.-W. Chen**, "Necktie and Stickpin," Taiwan Patent D134917, May 21, 2010.

[3] Y.-C. Chen and **H.-W. Chen**, "Direction Pointer," Taiwan Patent M318168, Sep 1, 2007.

Other Publications

[1] H.-W. Chen, and C.-K. Sun, "Terahertz technology- fiber scanning imaging system," Physics Bimonthly, vol. 31, 2009. **(Invited Paper)**

[2] H.-W. Chen, J.-Y. Lu, P.-J. Chiang, L.-J. Chen, H.-C. Chang, Y.-T. Li, C.-L. Pan, J.-L. Kuo, C.-K. Sun, "Loss spectrum of sub-wavelength THz fiber and its application," Journal of Optical Engineering, vol. 97, pp. 42-52, 2007. **(Invited Paper)**

Contents

Publication List 7
Chapter 1 Introduction 17
1.1. Background 17
1.2. Overview of the Thesis 20
Chapter 2 3-GHz Modelocked Yb-Fiber Oscillator 23
2.1. Background of High Repetition Rate Lasers 23
2.2. Key Components in Building a High Rep-rate Oscillator 25
2.2.1 Heavily Yb-doped Phosphate Glass Fiber 26
2.2.2 High-Dispersion Output Coupler 27
2.3. Experimental Setup 29
2.4. Laser Characterization 30
2.5. Summary 33
Chapter 3 Optimization of Femtosecond Nonlinear Yb-Fiber Amplifiers based on a Narrowband Oscillator 35
3.1. Motivation 35
3.2. Modeling Nonlinear Amplification of Femtosecond Pulses in YDFAs 36
3.3. Optimization of Different Amplifier Parameters 41
3.3.1 Optimization of the Input Pulse Pre-Chirp 41
3.3.2 Optimization of the Input Power and Optical Bandwidth 44
3.3.3 Optimization of the Yb-ion Doping Concentration 45
3.4. Summary 47
Chapter 4 Frequency Comb based on a 280-MHz Narrowband Yb-fiber Oscillator 49
4.1. Motivation 49
4.2. Background of High Rep-rate Frequency Comb 49
4.3. Narrowband 280 MHz Yb-Fiber Oscillator 52
4.4. Experimental Results on Pre-Chirp Management for Optimizing Compressed Pulse Quality 54
4.5. Frequency Comb based on the narrowband Yb-fiber oscillator 58
4.5.1 Pre-chirp Management for Spectral Broadening and Pulse Compression 59
4.5.2 Supercontinuum Generation and f_{CEO} Detection 61
4.5.3 Stabilization of f_{rep} and f_{CEO} 62
4.6. Summary 64
Chapter 5 3 GHz High Power Femtosecond Laser System 65

5.1. Introduction 65
5.2. Experimental Setup 65
5.2.1 Pre-Chirp Management on High Power Yb-Fiber Amplifier 66
5.2.2 Optimized 3-GHz High Power Laser System 68
5.3. Noise Performance 69
5.3.1 Relative Intensity Noise 69
5.3.2 Timing Jitter and f_{rep} Locking 70
5.4. Summary 73
Chapter 6 Application I: 3 GHz Yb-fiber Laser Based Few-Cycle Source at the Ti:sapphire Wavelength 75
6.1. Motivation 75
6.2. Frequency Up-Conversion using Fiber-Optic Cherenkov Radiation 76
6.3. Proof-of-Principle Experiment with a 29 MHz Yb-Fiber Laser 79
6.4. Experiment with the 3-GHz Yb-Fiber Laser System 84
6.5. Summary 89
Chapter 7 Application II: 3 GHz, Watt-Level Femtosecond Raman Soliton Source 91
7.1. Motivation 91
7.2. 3 GHz Raman Soliton Femtosecond Source Generation 92
7.2.1 Experimental Setup 92
7.2.2 Simulation of Raman soliton in Three Different PCFs 93
7.2.3 Experimental Results 95
7.2.4 Relative Intensity Noise of Different Order Raman Solitons 98
7.3. Summary 98
Chapter 8 3 GHz Passive Frequency Comb via Difference Frequency Generation 101
8.1. Motivation 101
8.2. Investigation of Supercontinuum Coherence 103
8.3. Passive Frequency Comb based on Difference Frequency Generation 107
8.3.1 Passive Frequency Comb ($f_{CEO} = 0$) 107
8.3.2 Experimental Setup and Results 108
8.3.3 Optical Linewidth of the 3 GHz passive comb 111
8.4. Summary 112
Chapter 9 Conclusion and Future Work: Towards a 3-GHz Yb-Fiber Astro-Comb 113
9.1. Conclusion 113
9.2. Current Issues 114
9.3. Future Work 115
9.3.1 Optical Linewidth Improvement 115

9.3.2 A Simpler Way to Build the 3 GHz Frequency Comb 116
9.3.3 Blue and Green Astro-Comb 116
9.3.4 All-fiber 10-GHz Yb-fiber Oscillator 116
Appendix A Chirally-Coupled-Core Modelocked Yb-Fiber Oscillator 119
A.1. Introduction 119
A.2. Key elements: 3C LMA fiber and HDMs 121
A.3. Experimental Setup and Results 123
A.4. Discussion 128
A.5. Further Power Scaling with Air-clad CCC Fiber 129
Appendix B Modeling of Femtosecond Yb-Fiber Oscillators 133
B.1. Introduction 133
B.2. Numerical Solution to the NLSE 134
B.2.1 Fourth-order Runge-Kutta Method in the Interaction Picture 135
B.2.2 Adaptive Method 136
B.3. Modeling of a Yb-fiber Oscillator Configured in a Ring Cavity 137
B.4. Simulation of an Yb-fiber Oscillator in Three Different Regimes 139
B.4.1 Stretched-pulse Regime ($GDD_{net} = -0.025$ ps^2) 140
B.4.2 Self-similar Regime ($GDD_{net} = +0.025$ ps^2) 143
B.4.3 All-normal Dispersion Regime ($GDD_{net} = +0.06$ ps^2) 144
B.5. Conclusion 148
Bibliography 149

Chapter 1

Introduction

1.1. Background

Many applications require femtosecond lasers with high repetition rate. A higher repetition rate means a shorter laser cavity. As illustrated in Fig. 1-1, in the time domain, a higher repetition rate means more pulses in a fixed time period. For nonlinear bio-optical imaging [1] (e.g., two-photon fluorescence excitation microscopy) in which photoinduced damage is caused by pulse energy rather than average power, increasing pulse repetition-rate will improve signal-to-noise ratio and reduce data acquisition time [2,3]. In the frequency domain, a higher repetition rate means the comb line spacing is larger. This permits access to and manipulation of each individual comb line. Such capabilities have opened numerous frequency-domain applications including optical arbitrary waveform generation [4–6], and high-resolution spectroscopy [7].

On the other hand, femtosecond optical sources in the optical spectrum range between 0.7 μm and 1.55 μm have found many applications such as optical coherence tomography [8–10], high speed optical sampling [11,12], photonic analog-to-digital conversion [13], and multi-photon spectroscopy [14], to name a few. To date, femtosecond solid-state lasers are mainly employed in these applications. Figure 1-2 shows the wavelength coverage of different solid-state lasers and

the wavelength range required for various applications. Take the two most common femtosecond solid-state lasers for example: a Ti:sapphire laser [15–17] can cover 0.7–1.1 μm and is useful for optical coherence tomography and multi-photon biological imaging. A Cr:forsterite laser [18–20] can operate in the wavelength range from1.15 to 1.35 μm, an important wavelength regime for multi-photon microscopy because light in this wavelength range experiences lower scattering loss and higher penetration depth for most biology samples. The generated two-photon and three-photon signals in the visible range facilitate the signal detection. Nonetheless, solid state lasers are usually expensive, bulky, and prone to misalignment. The gain crystals often requires water cooling. These disadvantages hamper their wide usage outside the lab environment. The mentioned versatile applications can be even more practical if we are able to make the overall system less expensive, flexible, and easy to maintain.

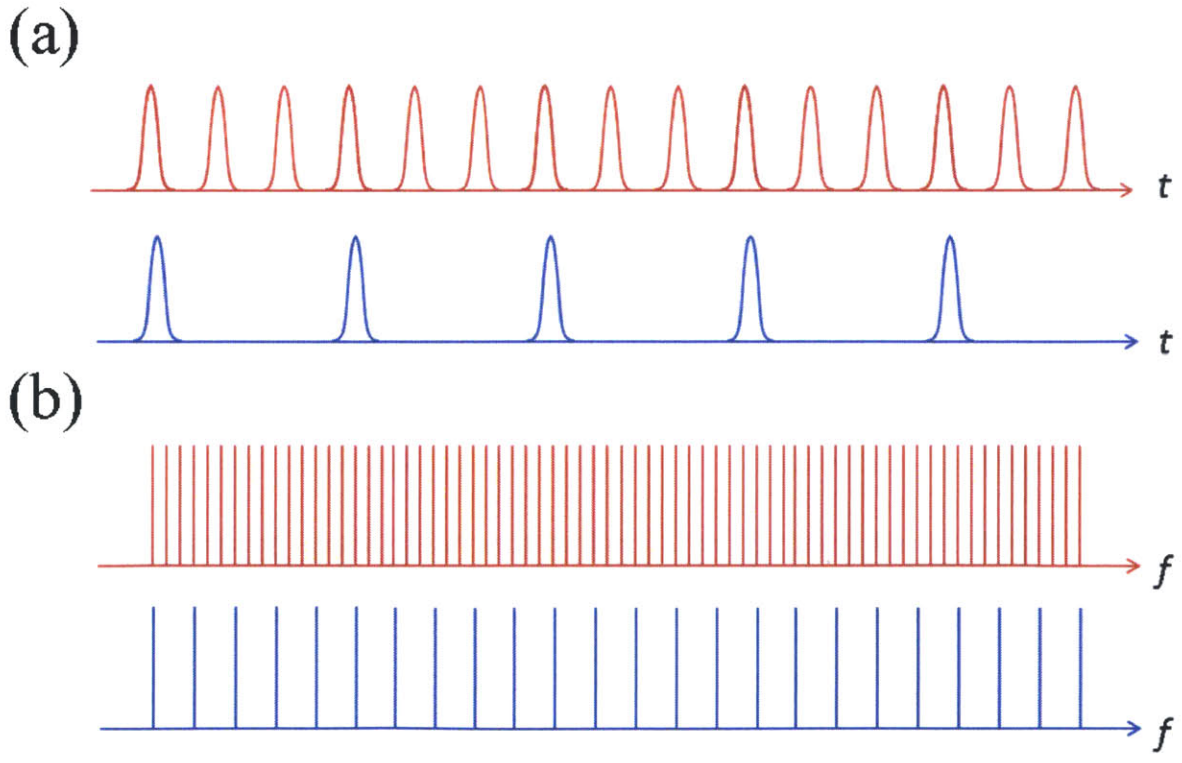

Fig. 1-1. Comparison of a low rep-rate laser (blue) and a higher rep-rate laser (red, 3 times higher rep-rate) in (a) the time domain and (b) the frequency domain.

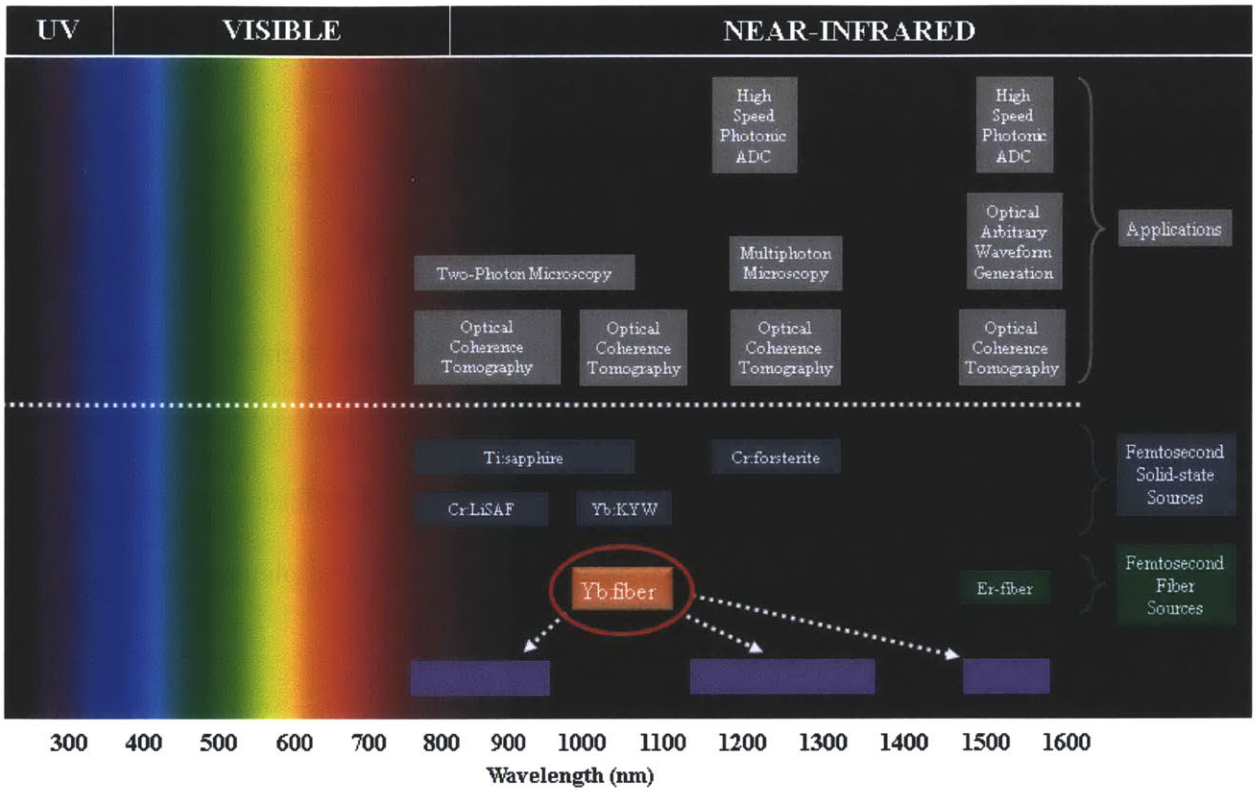

Fig. 1-2. The femtosecond sources and applications with their corresponding optical spectral range.

To solve the issues of cost, portability, and the cooling of the gain crystal in the wavelength range of 0.7 μm to 1.35 μm, we resort to fiber laser technology. Due to the large surface-to-volume ratio of the gain fiber, the intrinsically efficient heat dissipation requires no extra cooling. Among well-developed active fibers (e.g., Yb-fiber, Er-fiber, Tm-fiber, Ho-fiber, etc.), Yb-fiber excels for its excellent power scalability. Compared with other active fibers, the pump wavelength (915 nm or 976 nm) of the Yb-fiber is close to the gain wavelength (1030 nm) such that quantum efficiency is high and therefore greatly reduces the accumulated heat in a high-power Yb-fiber laser. In addition, Yb-fiber lasers provide wavelength coverage of 1.01–1.08 μm (Fig. 1-2) making them good candidates to perform broadband frequency upconversion to generate a femtosecond source at Ti:sapphire wavelengths or perform frequency down-conversion to the wavelength range from 1.1 μm to 1.35 μm as an alternative source to the Cr:forsterite laser. Furthermore, we can also use

difference frequency generation to develop an alternative source to Er:fiber laser. Note that if we choose an Er-fiber laser instead, whose wavelength coverage is around 1.55 μm, the frequency upconversion to the Ti:sapphire wavelength range would be unrealistic and challenging.

1.2. Overview of the Thesis

In this dissertation, we start with the demonstration of a 3 GHz high power Yb-fiber laser system and develop alternative femtosecond sources to Ti:sapphire laser, Cr:forsterite laser, and Er:fiber laser. These high repetition-rate sources will be versatile for different applications shown in Fig. 1-2. Our ultimate goal is to achieve a 3-GHz source comb to implement next-generation astro-combs.

The thesis is organized as follows. In Chapter 2, a 3-GHz fundamentally mode-locked, femtosecond Yb-fiber laser is demonstrated [21]. In Chapter 3, we numerically study the optimization of femtosecond Yb-doped fiber amplifiers (YDFAs) in order to achieve both high-quality and high-power compressed pulses [22]. In Chapter 4, we apply the proposed optimization method to a narrowband 280-MHz oscillator, validate the feasibility of pre-chirp management, and construct the 280 MHz frequency comb through conventional f_{CEO} detection and stabilization [23]. In Chapter 5, we then apply the optimization method to the 3 GHz Yb-fiber oscillator to achieve a 3 GHz high power femtosecond Yb-fiber laser system. On top of this system, in Chapter 6 we demonstrate a few-cycle ultrafast source at the Ti:sapphire laser wavelength as a promising substitute of multi-GHz mode-locked Ti:sapphire lasers [24] and in Chapter 7 we demonstrate a watt-level, femtosecond Raman soliton source wavelength-tunable from 1.15 μm to 1.35 μm [25]. These sources will be useful for applications in optical frequency metrology and multi-photon coherent microscopy. In Chapter 8, a preliminary 3 GHz passive fiber laser frequency comb at 1.5 μm via difference frequency generation is demonstrated. Finally, in Chapter 9

the thesis is concluded by discussing current issues and possible solutions are suggested. In Appendix A, other research results on high power Chirally-Coupled-Core Yb-doped modelocked lasers are introduced [26,27]. In Appendix B, the pulse dynamics of the modelocked Yb-fiber oscillator in different regimes is investigated through numerical simulation.

Chapter 2

3-GHz Modelocked Yb-Fiber Oscillator

2.1. Background of High Repetition Rate Lasers

High repetition rate (>1 GHz) lasers with femtosecond pulse duration are required in many applications. For nonlinear bio-optical imaging (e.g., two-photon fluorescence excitation microscopy) in which photoinduced damage is caused by pulse energy rather than average power, increasing pulse repetition rate will improve signal-to-noise ratio and reduce data acquisition time [2,3]. Frequency combs — achieved by fully stabilizing both the repetition rate and the carrier-envelope offset frequency of multi-GHz lasers — exhibit large line spacing (equal to the laser's repetition rate) that may permit access to and manipulation of each individual comb line. Such capabilities have opened numerous frequency-domain applications including optical arbitrary waveform generation [4], high-speed analog-to-digital conversion [13], and high-resolution spectroscopy [7]. Of particular importance is precision calibration of astronomical spectrographs to search for Earth-like exoplanets, which normally requires femtosecond laser frequency combs with >15-GHz line spacing ("astro-comb") [28–33]. Current implementation of an astro-comb relies on using multiple Fabry-Perot (FP) filtering cavities to multiply the line spacing of a frequency comb based on low repetition rate lasers. For example, the astro-comb system in Ref. [32] employs a 250-MHz Yb-fiber laser as the front end, followed by three cascaded

FP filtering cavities for line-space multiplication. Stabilizing these FP cavities, locking them to the frequency comb, and preventing parasitic cavities between two FP cavities constitute the major challenge in constructing a practical astro-comb. Such an issue can be alleviated by employing a frequency comb based on a femtosecond laser operating at much higher repetition rate (e.g., 3-10 GHz). The significantly simplified astro-comb requires only one FP cavity and becomes more reliable.

Several types of femtosecond mode-locked lasers have demonstrated operation with >1 GHz repetition rate [34–39]. Up to date, however, fully-stabilized frequency combs with >1 GHz comb-spacing are only implemented based on Ti:Sapphire lasers (10 GHz) [34], Yb-fiber lasers (1 GHz) [39], and most recently Er-fiber lasers (1 GHz) [40]. Among them, Yb-fiber laser frequency combs possess superior power scalability thanks to the rapid development of double-clad Yb-fibers and high-brightness pump diodes as well as the Yb-fiber's high pump-to-signal conversion efficiency (~80%). For example, Yb-fiber laser frequency combs with 80-W average power has been demonstrated, albeit at lower repetition rate of 154 MHz [41]. Such power scalability is critical for multi-GHz frequency combs involved in nonlinear optical applications (e.g., wavelength conversion into the visible-wavelength range) where pulse energies of several nano-joules are nominally required.

We have developed a green astro-comb composed of >7000 lines spaced by 16 GHz from 500-620 nm with homogeneous line power (variation <8 dB). The green astro-comb is generated from a 1 GHz Ti:sapphire octave-spanning comb laser, a tapered PCF that coherently blue-shifts comb lines to 500 nm, and two broadband Fabry-Perot cavities (FPCs) that increase the line spacing to 16 GHz. This green astro-comb has been deployed as a wavelength calibrator for the HARPS-N spectrograph at the TNG telescope. Operating and stabilizing the two FPCs of this

astro-comb constitute major technical challenges for this green astro-comb. Such issues can be lessened by employing a frequency comb based on a femtosecond laser operating at much higher repetition rate (e.g., 3-10 GHz). In this work, we demonstrate the most critical component for constructing 3 GHz source comb—a fundamentally mode-locked Yb-fiber oscillator with 3-GHz repetition rate [21].

2.2. Key Components in Building a High Rep-rate Oscillator

Constructing fundamentally mode-locked Yb-fiber lasers with >1-GHz repetition rate and femtosecond pulse duration demands two crucial elements: (1) a short (<10 cm), highly doped Yb-fiber to provide enough round-trip gain and self-phase modulation, and (2) a dispersion compensating device to provide enough negative group-delay dispersion (GDD) to compensate for the positive GDD from the Yb-fiber and other intra-cavity components (e.g., lens). A laser cavity with net negative GDD is necessary to ensure soliton-like pulse formation that serves as the main pulse shortening mechanism for high repetition rate fiber lasers to generate femtosecond pulses [42]. Recently, Ingmar Hartl et al. demonstrated 1.04-GHz Yb-fiber lasers (fully stabilized) using 6-cm gain fiber spliced to a fiber Bragg grating for dispersion compensation [39]. By further shortening the gain fiber (down to 4 cm) and employing a Martinez compressor for dispersion compensation, the same group has increased the repetition rate up to 1.6-GHz [43]. Further repetition rate scaling apparently demands shrinking the laser cavity by shortening the gain fiber and avoiding bulky free-space devices (e.g., diffraction gratings) for dispersion compensation. Here, we present a 3-GHz femtosecond Yb-fiber laser incorporating two key technologies: (1) a 1-cm, heavily Yb-doped phosphate glass fiber as the gain medium and (2) a high-dispersion output-coupler for dispersion compensation.

2.2.1 Heavily Yb-doped Phosphate Glass Fiber

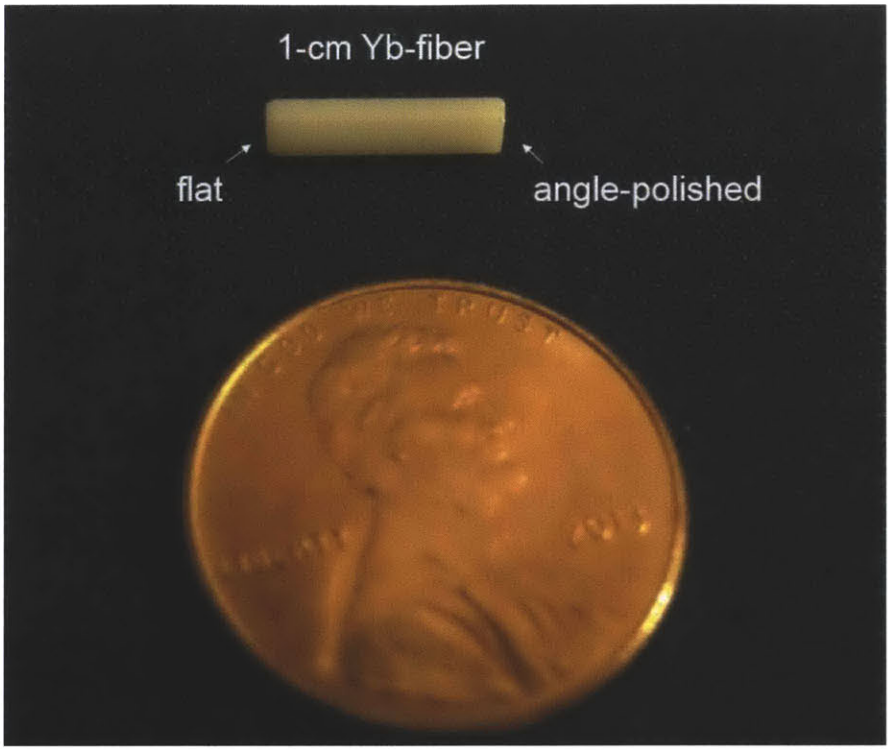

Fig. 2-1. The photo of 1-cm long Yb-doped phosphate fiber encapsulated in a ceramic ferrule.

The highly doped gain fiber is provided by our collaborator, Prof. Zhongmin Yang's group at South China University of Technology. The Yb-doped phosphate glass fiber has the highest reported Yb^{3+} concentration of 15.2 wt% and exhibits 46-dB/cm absorption at 976 nm. The net gain coefficient of the phosphate glass fiber was measured to be 5.7 dB/cm [44]. Other important parameters are 1.84-ms upper-state lifetime, 5-μm core diameter, and numerical aperture of 0.14. The 1-cm long fiber is encapsulated in a ceramic ferrule as shown in Fig. 2-1. A penny is placed below to compare with the size of the fiber. Due to the large surface-to-volume ratio for the fiber, the resulting intrinsically efficient heat dissipation requires no extra cooling. During the experiments, thermal damage of the fiber is absent. The polished end of the fiber is directly attached to an output coupler.

2.2.2 High-Dispersion Output Coupler

The specification of the specially designed coating on the output coupler is shown in Fig. 2-2. It is customized to compensate the normal dispersion from a 7-cm long fused silica fiber and allows >97% pump transmission at 976 nm and 10% ± 2% signal transmission at 1010-1050 nm. The calculated reflectivity and dispersion are shown in Fig. 2-2 as the solid blue line and the green line, respectively. It is designed to provide -1000 fs^2 ± 200 fs^2 GDD at 1010-1050 nm, when attached to fused silica (i.e. input medium: fused silica), in order to render a negative-dispersion laser cavity for soliton pulse formation. The thickness of the coating is ~10 um with alternating layers of Ta_2O_5 and SiO_2.

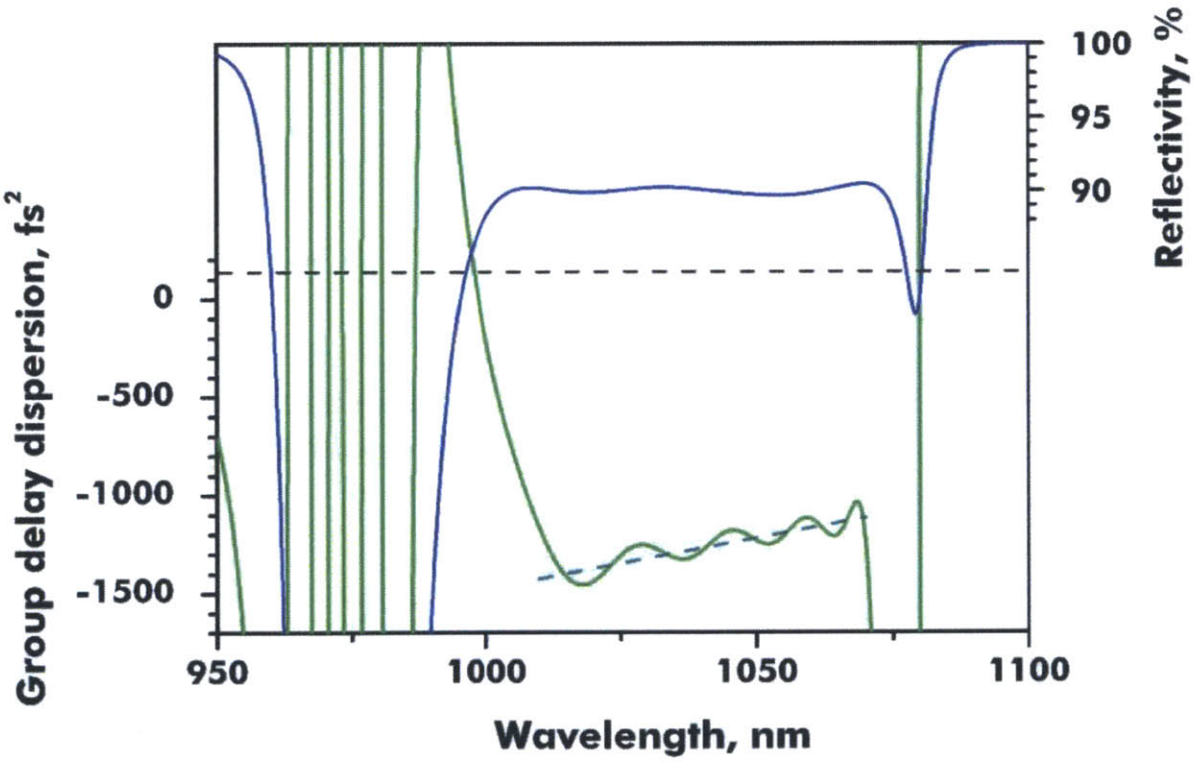

Fig. 2-2. Reflectivity and dispersion of the specially designed coating on the output coupler when attached to fused silica. Theoretical curves of reflectivity and dispersion are solid blue line and green line, respectively. Target value for compensating dispersion from a 7-cm fused silica fiber: dashed dotted grey line.

Because the output coupler is designed for fused silica as the input medium, the measurement of the reflectivity and the dispersion curve with the output coupler attached to the fused silica is challenging. To test the fabrication quality, we measure the transmission of the output coupler with air as the input medium. Figure 2-3 plots the measured transmission spectra of 30 one-inch output couplers. The transmission at 976 nm pump wavelength varies dramatically from 44% to 98% and the transmission at 1030 nm signal wavelength varies from 4% to 13%, which indicates there are considerable fabrication errors. Also, the overall spectrum can drastically shift by as much as ~15 nm.

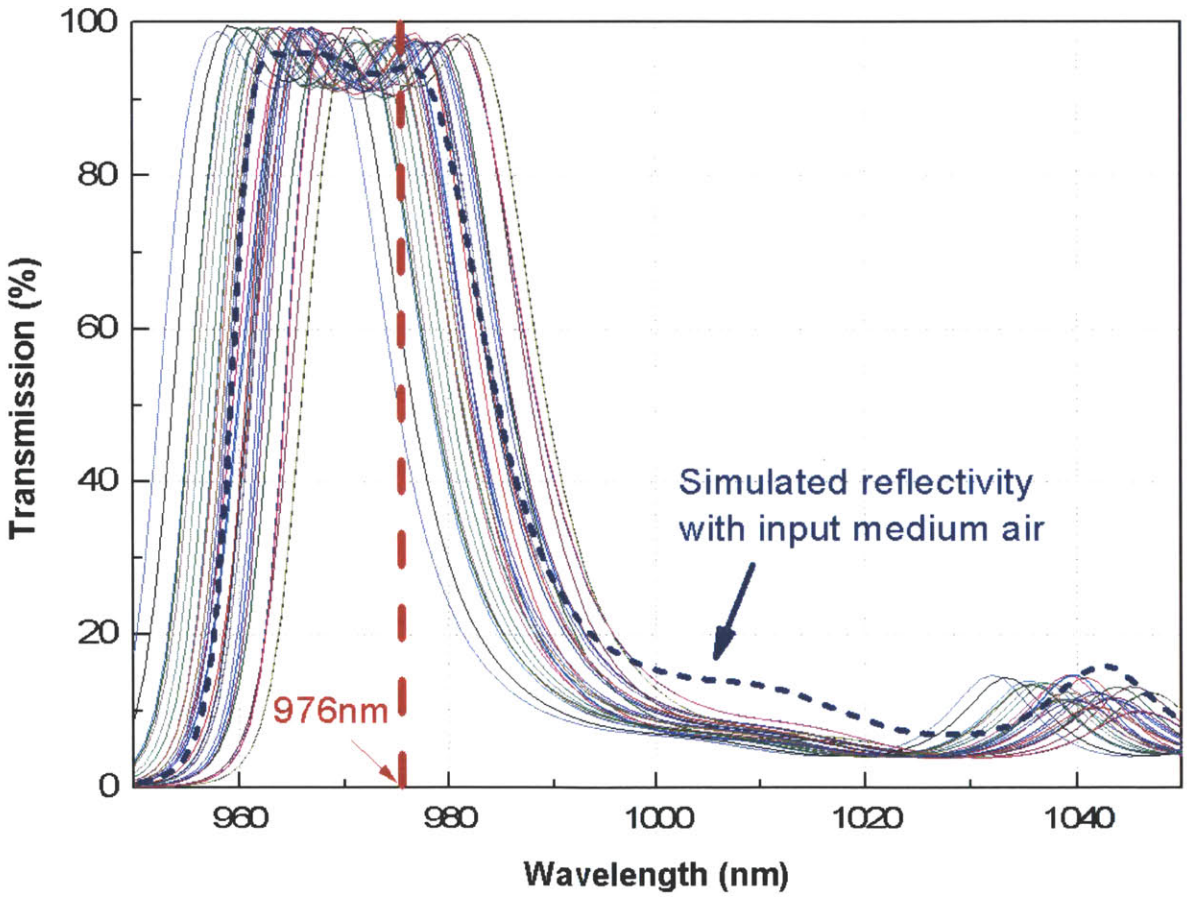

Fig. 2-3. Transmission measurement of 30 one-inch output couplers. The dotted blue line shows the simulated reflectivity with input medium air of the designed coating.

As a matter of fact, such a coating design is inevitably prone to fabrication errors because the pump window is so close to the signal window. The fabricated output couplers deviate a lot from the theoretical design, which leads to difficulties when building the first 3-GHz Yb-fiber oscillator.

2.3. Experimental Setup

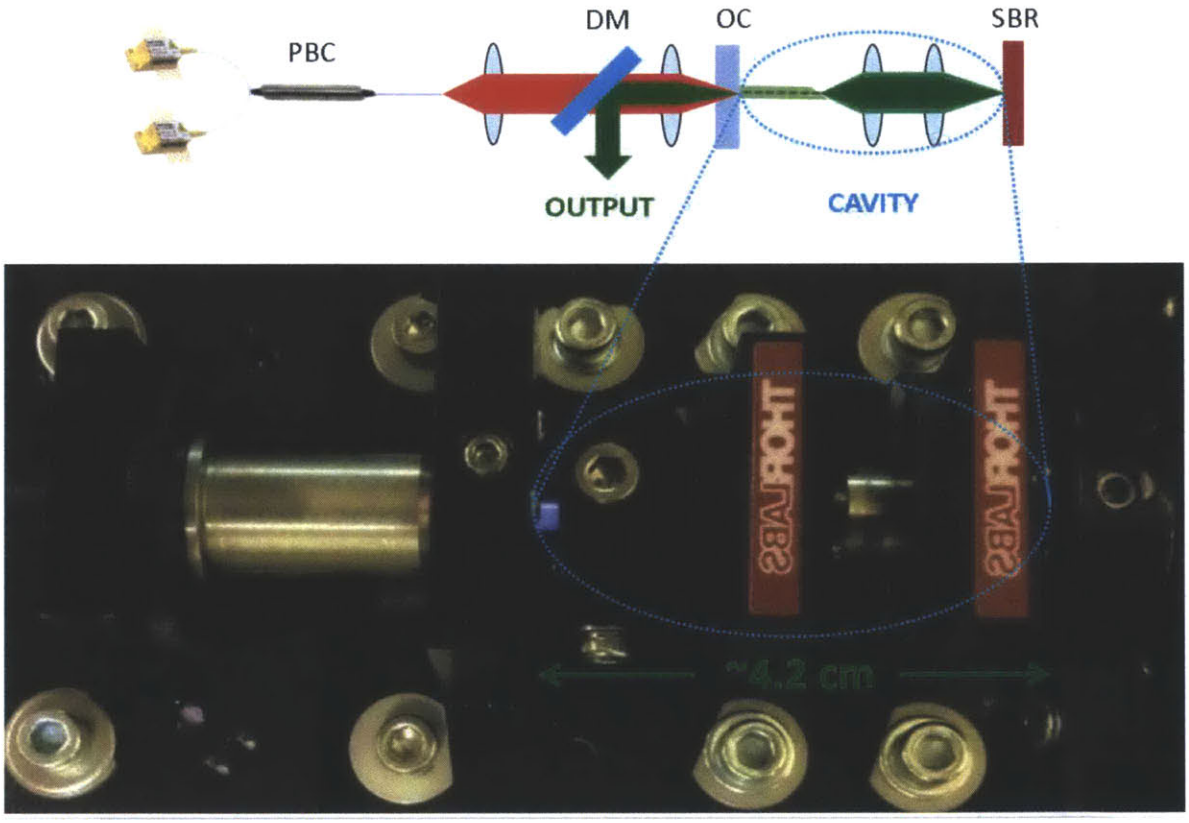

Fig. 2-4. (Top) schematic setup of the 3-GHz Yb-fiber oscillator. PBC: polarization beam combiner, DM: dichroic mirror, OC: output coupler, and SBR: saturable Bragg reflector. (Bottom) Photos of the oscillator cavity.

As shown in Fig. 2-4, the laser is configured as a linear cavity (indicated by the blue dotted circle) with a total length of ~4.2 cm. Two fiber-coupled pump diodes are power combined using a fiber-based polarization beam combiner, providing up to 1.2-W average power centered at 976 nm. A 22.5° incident angle dichroic mirror inserted between the combiner and the laser cavity separates the output laser power from the pump. The fiber is held by a specially-designed strain-

relief clamp. During the experiment, thermal damage of the fiber is absent. Due to the large surface-to-volume ratio of the fiber, the resulting intrinsically efficient heat dissipation requires no extra cooling. The polished end of the fiber is directly attached to an output coupler. The pump beam after the dichroic mirror will be focused first, propagate through the output coupler, and then coupled into the polished end of the fiber. The other end of the Yb-fiber is angle polished (~8 degree) to avoid back reflection. Two aspheric lenses are used to re-image the fiber output onto a saturable absorber reflector (SBR) in order to initiate the mode-locking. The commercially available SBR (from BATOP, model: SAM-1040-8-1ps) has a non-saturable loss of 3%, a modulation depth of 5%, a saturation fluence of 40 $\mu J/cm^2$, and recovery time 1 ps. The spot size on the SBR is ~13 μm in diameter.

2.4. Laser Characterization

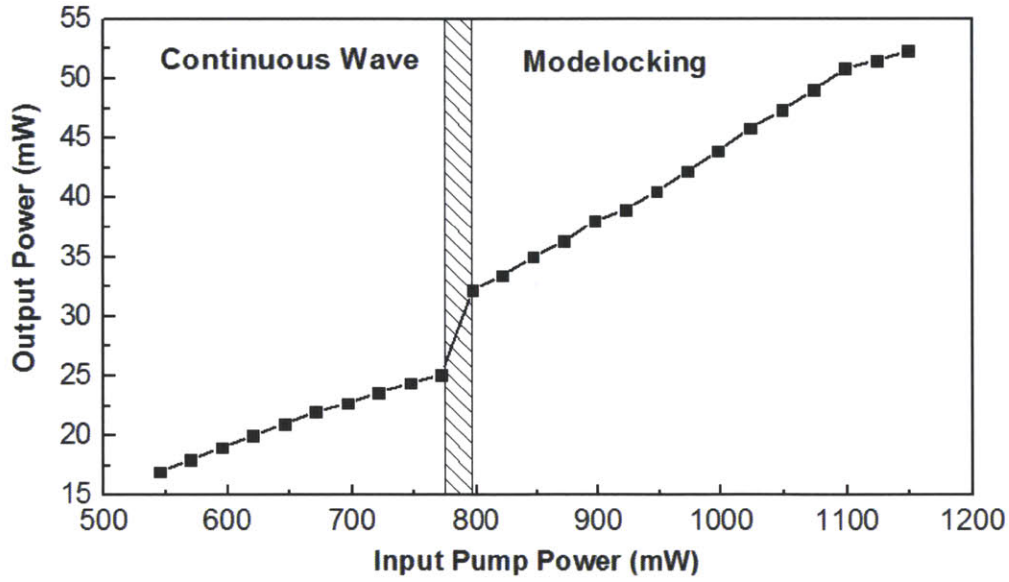

Fig. 2-5. Output power vs. input pump power. Mode-locking self-starts as the input pump power exceeds 800 mW.

The dependence of output power on the input pump power is illustrated in Fig. 2-5 for different operation regimes. At relatively low pump power, the oscillator operates at continuous

wave (CW) mode. Mode-locking self-starts as the pump power reaches ~800 mW. With increasing pump power from 800 mW to 1.15 W, the modelocked output power grows accordingly from 32 mW to 53 mW.

We characterized the laser at 1073-mW input pump power, corresponding to a laser power of 49 mW. The measured optical spectrum, shown in Fig. 2-6(a), has 5.5-nm bandwidth at full width at half maximum (FWHM). The RF spectrum recorded in Fig. 2-6(b) indicates a 3-GHz repetition rate with signal to background ratio >60 dB. The output pulse duration is also measured by a background free autocorrelator; the resulting autocorrelation trace plotted in Fig. 2-7(a) shows a 319-fs FWHM duration (black line). As a comparison, the autocorrelation trace of the transform limited pulse calculated from the optical spectrum in Fig. 2-6(a) is plotted in Fig. 2-7(a) as the red dashed line. With a de-convolution factor of 1.54 (assuming a hyperbolic secant pulse profile), the pulse duration is estimated to be ~206 fs. It is about 56-fs longer than the calculated transform-limited duration shown in Fig. 2-7(b) (i.e. 150 fs), showing that the optical pulses are slightly chirped.

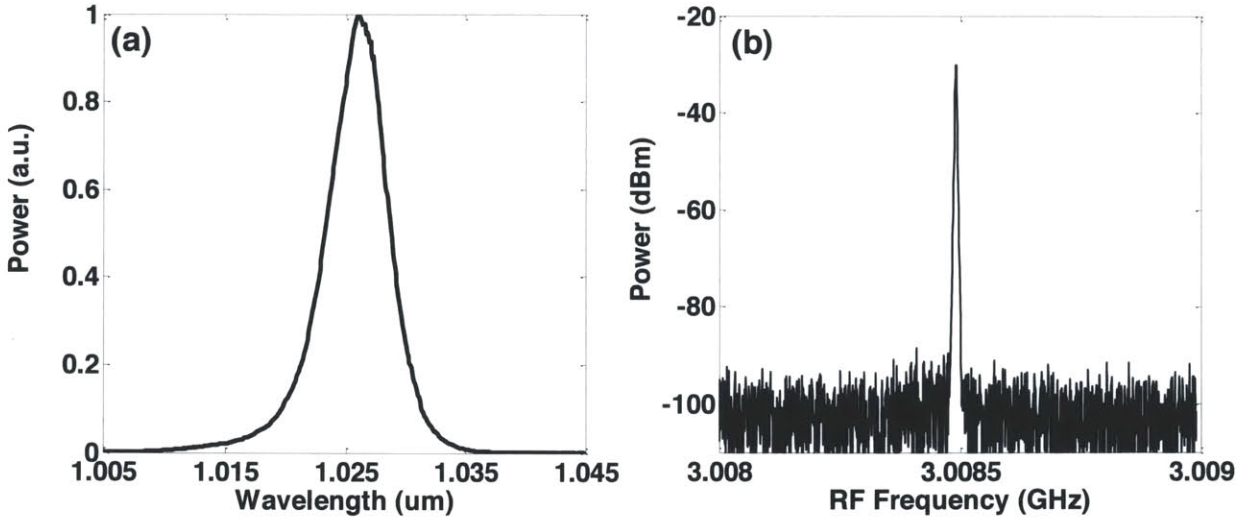

Fig. 2-6. (a) Optical spectrum of the output pulse with 1073-mW pump power. (b) The RF spectrum with a resolution bandwidth of 3 kHz.

Without any enclosure of the laser or any other means to prevent ambient disturbances (e.g., air current, vibration, temperature fluctuation, etc.), we measured the relative intensity noise (RIN) of the 3-GHz laser running at the input pump power of 1073 mW. It is shown as the blue curve in Fig. 2-8. Also plotted in the same figure (green dashed curve) is the integrated RIN. Integration between 10 Hz to 10 MHz results in an integrated RIN of 0.14%.

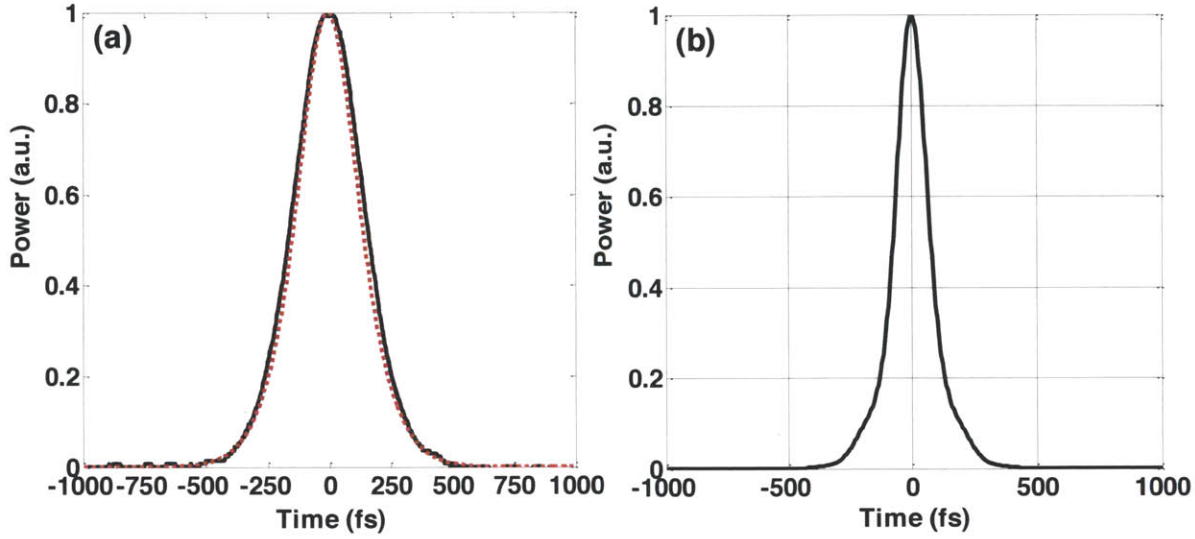

Fig. 2-7. (a) The measured autocorrelation trace of the output pulse (black line) and the calculated autocorrelation trace of the transform-limited pulse (red dashed line). (b) The transform limited pulse.

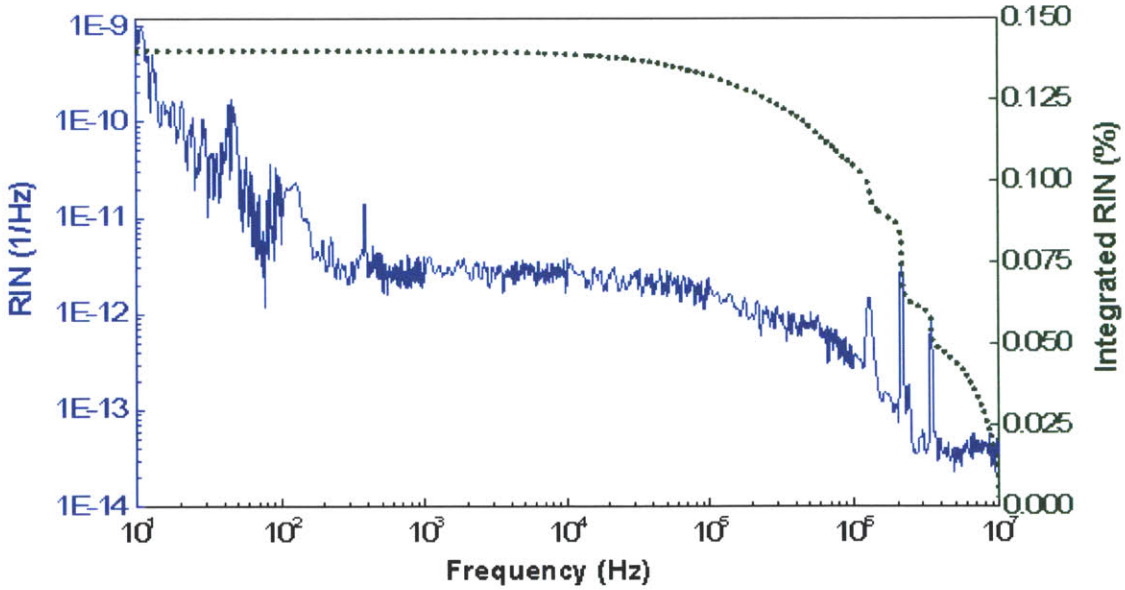

Fig. 2-8. Relative intensity noise (RIN) (blue curve) of the mode-locked 3-GHz Yb-fiber laser and the integrated RIN (green dashed curve).

Without any polarizing element in the cavity, the output pulses might exhibit polarization evolution or the laser might emit stable elliptically polarized-solitons, called polarization-locked vector solitons (PLVS's) [45–51] due to the slight birefringence in the fiber. To produce the linearly polarized output pulses, we insert a thin-film Polarcor polarizer (0.5 mm thick) between two aspheric lenses in the cavity.

2.5. Summary

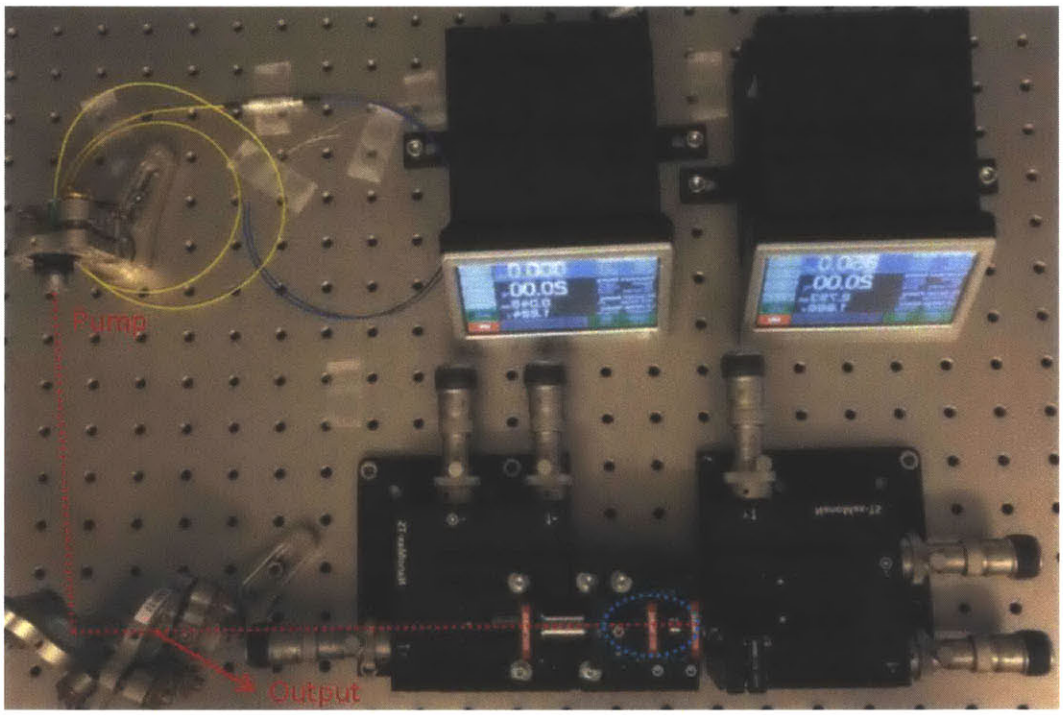

Fig. 2-9. The photo of the third 3-GHz Yb-fiber oscillator setup built in 49D in Center for Free-Electron Laser Science, DESY, Germany in January 2014.

We have demonstrated a fundamentally mode-locked, femtosecond (~206 fs) Yb-fiber laser with, to the best of our knowledge, the highest repetition rate of 3 GHz among reported femtosecond Yb-fiber lasers. With a 1-cm heavily Yb-doped phosphate glass fiber as the gain medium and a high-dispersion output coupler for dispersion compensation, the laser self-starts and produces up to 53-mW average power. The mode-locking usually lasts for about three days to one

week until the focusing spot on the SBR is damaged. Shifting to a different spot immediately recovers the mode-locking. Use of a back-thinned SBR facilitates heat dissipation and helps prevent thermal damage. With this method, the modelocking can last for more than 30 days. The current intra-cavity loss is estimated to be ~50%, which allows us using an output coupler with larger output coupling ratio (e.g., 10%) to increase the output power (and thus the power efficiency) of the laser without losing the mode-locking. We have built three 3 GHz Yb-fiber oscillators in total. Figure 2-9 shows the photo of the third 3-GHz Yb-fiber oscillator setup built in the Center for Free-Electron Laser Science, DESY, Germany in January 2014. Ongoing work includes further repetition rate scaling up to 10 GHz by directly sandwiching the 1-cm Yb-fiber between the output coupler and the SBR while maintaining femtosecond pulse duration.

Chapter 3

Optimization of Femtosecond Nonlinear Yb-Fiber Amplifiers based on a Narrowband Oscillator

3.1. Motivation

Yb-doped fiber amplifiers (YDFAs) feature superior power scalability, large single-pass gain (~30 dB), high electrical-to-optical conversion efficiency, excellent beam quality, as well as compactness and robustness. To avoid detrimental effects from fiber nonlinearities (e.g., self-phase modulation (SPM), stimulated Raman scattering etc.) when amplifying ultrashort pulses, YDFAs normally operate in a low-nonlinearity regime using chirped pulse amplification (CPA) [52,53], in which the spectral bandwidth of the amplified pulse only changes slightly during the amplification.

For some applications, strong nonlinear effects are preferred in YDFAs such that the amplified pulse acquires substantial extra bandwidth, and therefore can be compressed to be much shorter than the pulse prior to the amplification. This operation regime is of particular importance for implementing high repetition-rate (>1 GHz) master-oscillator-power-amplification (MOPA) systems with applications including optical arbitrary waveform generation, high-resolution spectroscopy, high-speed analog-to-digital conversion [13], and precision calibration of

astronomical spectrographs to search for earth-like extra-solar planets [7], to name a few. The ideal front-end of such a MOPA laser system is a fundamentally mode-locked fiber oscillator with multi-GHz repetition rate. Primarily limited by the available pump power (~1 W) from single-mode laser diodes and low intra-cavity pulse energy, these multi-GHz fiber oscillators typically produce sub-picosecond/picosecond pulses with <100 mW average power. The poor performance on pulse duration and average power prevents multi-GHz fiber oscillators from most nonlinear optical applications that usually demand femtosecond (~100 fs) pulses of several nano-joules for pulse energy. Such a limitation can be overcome by nonlinear amplification in YDFAs which broadens the input pulse spectrum. The spectrally-broadened, power amplified pulses are then de-chirped by a subsequent optical compressor to much shorter pulse duration. However, relatively narrow gain bandwidth (~40 nm) of Yb-doped fibers and the gain narrowing effect during the power amplification usually generate compressed pulses >100-fs with considerable pedestal. In this chapter we both numerically and experimentally study the dependence of the compressed pulse quality on the parameters of the fiber amplifier (e.g., doping concentration and length of the gain fiber) and the input pulse (e.g., pre-chirp, duration, and power) from the fiber oscillator. The results from detailed numerical modeling are presented in Section 3.2 and 3.3. We find that the input pulse pre-chirp—a quantity that can be easily tuned in experiments—is critical for optimizing the system to achieve high-quality compressed pulses. Section 3.4 presents the experimental results confirming the existence of an optimum *negative* pre-chirp that leads to the best-quality compressed pulses, as predicted by numerical modeling. Finally Section 3.5 concludes the chapter.

3.2. Modeling Nonlinear Amplification of Femtosecond Pulses in YDFAs

Amplification of femtosecond pulses in an YDFA involves nonlinear interaction among the pump, signal (i.e., the input pulses to be amplified), and Yb-fiber. The process can be accurately

modeled by coupling two sets of eqs. [54–56]: (1) the steady-state propagation rate eqs. that treat the Yb-fiber as a two-level system and (2) the generalized nonlinear Schrödinger equation (GNLSE) that describes the evolution of the amplified pulses. Such a model, with all the modeling parameters experimentally determined, enables us to study and therefore optimize a femtosecond MOPA system.

The YDFA can be pumped in the co-propagating scheme (i.e., pump and signal propagate in the same direction.), counter-propagating scheme (i.e., pump and seed propagate in the opposite direction.), or both. In this chapter, we focus on the co-propagating pumping scheme which is normally adopted in monolithic femtosecond nonlinear fiber amplifiers. Under this scenario and with amplified spontaneous emission (ASE) neglected, the model includes the following steady-state-propagation rate eqs. [57–59] and the GNLSE [60]:

$$\begin{aligned}
\frac{\partial N_2(t,z)}{\partial t} &= [R_{12}(\lambda,z)+W_{12}(\lambda,z)]N_1(t,z)-[R_{21}(\lambda,z)+W_{21}(\lambda,z)+1/\tau_{21}]N_2(t,z)\\
\frac{\partial N_1(t,z)}{\partial t} &= [R_{21}(\lambda,z)+W_{21}(\lambda,z)+1/\tau_{21}]N_2(t,z)-[R_{12}(\lambda,z)+W_{12}(\lambda,z)]N_1(t,z)\\
\frac{\partial P_p(\lambda,z)}{\partial z} &= \Gamma_p(\lambda)[\sigma_e(\lambda)N_2(z)-\sigma_a(\lambda)N_1(z)]\rho P_p(\lambda,z)\\
\frac{\partial P_s(\lambda,z)}{\partial z} &= \Gamma_s(\lambda)[\sigma_e(\lambda)N_2(z)-\sigma_a(\lambda)N_1(z)]\rho P_s(\lambda,z).
\end{aligned} \tag{1}$$

$$\begin{aligned}
\frac{\partial A}{\partial z} &= \int_0^\infty g(\omega)\tilde{A}(\omega)e^{-i\omega T}d\omega-\frac{\beta_2}{2}\frac{i\partial^2 A}{\partial T^2}+\frac{\beta_3}{6}\frac{\partial^3 A}{\partial T^3}\\
&\quad +i\gamma(1+\frac{i}{\omega_0}\frac{\partial}{\partial T})(A(z,T)\int_0^\infty R(t')\left|A(z,T-t')\right|^2 dt')
\end{aligned} \tag{2}$$

In Eq. (1), the amplifier is treated as a homogeneously broadened two-level system. ρ accounts for the ion density per unit volume. N_2 and N_1, satisfying $N_2(t,z)+N_1(t,z)=1$, denote the ion fraction for the upper state and the ground state. $P_s(\lambda,z)$ and $P_p(\lambda,z)$ represent the signal and pump power at position z for wavelength λ. Γ_p (Γ_s) corresponds to the modal overlap factor

between the pump (signal) mode and the ion distribution [61]. σ_e and σ_a denote the emission and absorption cross-sections. The spontaneous decay rate from level 2 to 1 is $1/\tau_{21}$; τ_{21} is the characteristic fluorescence lifetime. The stimulated absorption/emission rate and pumping rate for a fiber core-area A are $W_{ij}=\Gamma_s(\lambda)\sigma_{e,a}P_s/h\upsilon_s A$ and $R_{ij}=\Gamma_p(\lambda)\sigma_{e,a}P_p/h\upsilon_p A$, respectively. For the steady-state solution, by setting $\partial N_2(t,z)/\partial t = 0$, we then obtain

$$N_2(z)=[R_{12}(\lambda,z)+W_{12}(\lambda,z)]/[R_{12}(\lambda,z)+R_{21}(\lambda,z)+W_{12}(\lambda,z)+W_{21}(\lambda,z)+1/\tau_{21}]. \quad (3)$$

When writing Eq. (3), we assume that the inverse of the pulse's repetition-rate is much shorter than the relaxation time of the upper level (~1 ms), which holds for our devices.

The nonlinear propagation of the signal pulse is governed by the standard GNLSE (i.e., Eq. (2)), taking into account the gain, dispersion, self-phase modulation, self-steepening, and stimulated Raman scattering. $A(z,t)$, β_n, γ, and ω_0 are the amplitude of the slowly varying envelope of the pulse, n-th order fiber dispersion, fiber nonlinearity, and central frequency of the pulse, respectively. $R(t)$ denotes both the instantaneous electronic and delayed molecular responses of silica molecules, and is defined as $R(t)=(1-f_R)\delta(t)+ f_R(\tau_1^2+ \tau_2^2)/(\tau_1\tau_2^2)exp(-t/\tau_2)sin(t/\tau_1)$ where f_R, τ_1, and τ_2 are 0.18, 12.2 fs, and 32 fs, respectively [60]. The GNLSE is solved by the split-step Fourier method implemented using the fourth-order Runge-Kutta method in the interaction picture [62] with adaptive step-size control [63].

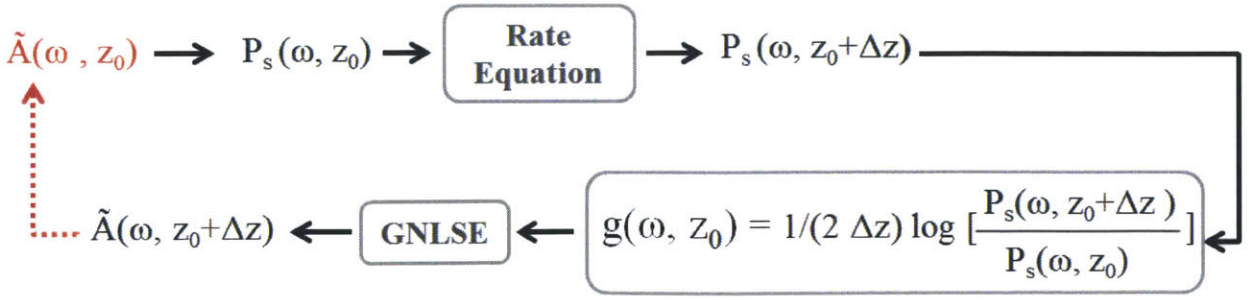

Fig. 3-1. Iteration flow chart of the modelling.

Flow chart in Fig. 3-1 illustrates the iteration in numerically solving Eq. (1) and (2). In each step, the signal power spectrum $P_s(\omega,z_0)$ is first calculated from $\tilde{A}(\omega,z_0)$ and then substituted into the rate equation Eq. (1) to obtain the signal power $P_s(\omega,z_0+\Delta z)$ at the next position. The gain spectrum $g(\omega,z_0)$ is derived from $P_s(\omega\ ,\ z_0+\Delta z)$ and $P_s(\omega,z_0)$, and fed into Eq. (2) to derive $\tilde{A}(\omega,\ z_0+\Delta z)$ from $\tilde{A}(\omega,z_0)$. Repeating this iteration generates the longitudinal distribution of pump power and population inversion as well as the nonlinear evolution of the seed-pulse along the gain fiber.

Table 3-1. Amplifier parameters used in the simulation

Pump Wavelength	**Core Diameter (a)**	**Core Numerical Aperture (N.A.)**	**Fluorescence Lifetime (τ_{21})**	β_2	β_3	γ
976 nm	5 μm	0.13	1.4 ms	23 fs^2/mm	30 fs^3/mm	0.0047 $(Wm)^{-1}$

Table 3-1 lists the key simulation parameters. For a single-mode step-index fiber with its fundamental mode approximated by a Gaussian, the overlap of the optical mode and ion distribution becomes $\Gamma=1-exp(-2a^2/w^2)$. a is the ion dopant radius or core radius and w the mode field radius at $1/e^2$ power intensity approximated by the Whitely model: $w=a(0.616+1.66/V^{1.5}+0.987/V^6)$ [41], where V is the normalized frequency. The wavelength dependent emission cross-section σ_e and absorption cross-sections σ_a are adapted from Fig. 2 in Ref. 30.

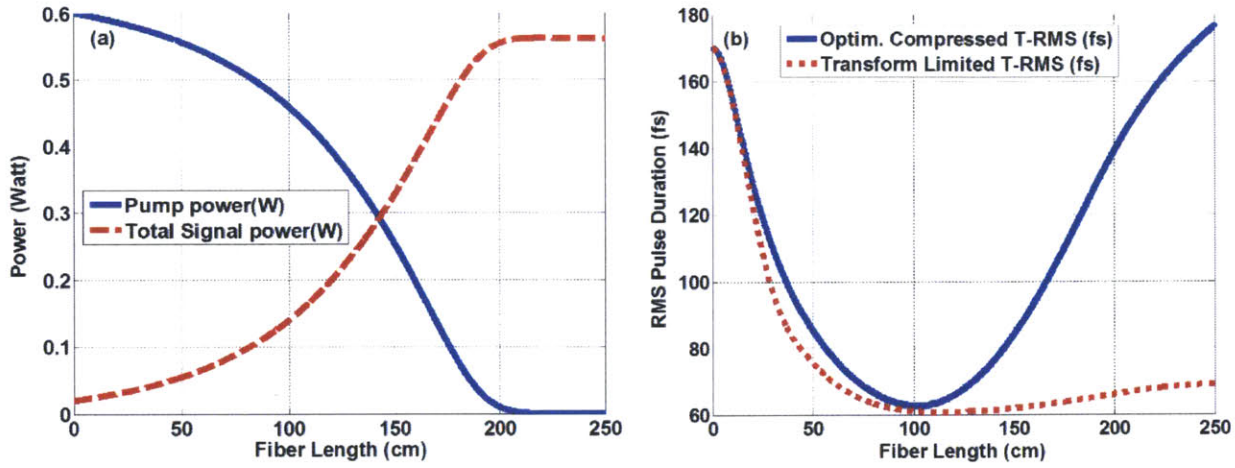

Fig. 3-2. (a) Pump and signal power as a function of Yb-fiber length. (b) RMS duration of the optimum compressed- pulse and the transform-limited pulse as a function of Yb-fiber length.

As an example, we study a YDFA seeded with an 80-MHz pulse train centered at 1.03 μm with 20-mW average power corresponding to 0.25-nJ pulse energy. The amplifier is constructed from a single-mode Yb-fiber with the ion density of 1025 m^{-3} pumped by a 976-nm diode with 600-mW average power. The amplified pulse is then compressed using a pair of diffraction-gratings (600 grooves/mm for line density) operating at 45° incident angle which introduces a negative group-delay dispersion (GDD) of -1408 fs^2/mm and a third order dispersion of 2180 fs^3/mm. For the simulation results in Fig. 3-2, the input signal is a transform-limited Gaussian pulse of 170-fs root-mean-square (RMS) (or 200-fs full width at half maximum (FWHM)) duration. Figure 3-2(a) plots the absorption of pump (blue, solid line) and amplification of signal (red, dashed line) as a function of Yb-fiber length. For a 2-m Yb-fiber, the pump is almost completely absorbed and the signal power reaches the maximum of 560 mW. Note that in this chapter, the input pulse is characterized by FWHM duration which is normally used for a Gaussian-shaped pulse. For a compressed pulse, we use RMS duration which provides better information on both the compression quality and the pulse pedestal. At each Yb-fiber length, the grating-pair separation is adjusted to compress the amplified pulse to the optimum (i.e., shortest)

RMS duration, plotted in Fig. 3-2(b). As a comparison, the corresponding transform-limited RMS duration is plotted in the same figure as well. While the transform-limited duration monotonically decreases due to the continuous increase of the pulse's bandwidth, the optimum compressed duration reaches a minimum value of 63-fs at the Yb-fiber length of 100-cm. At this length, the compressed duration coincides with the transform-limited duration indicating a close-to-perfect compression. Nonetheless, the signal power is only amplified to 140 mW.

3.3. Optimization of Different Amplifier Parameters

As shown above, although a longer Yb-fiber length leads to higher amplified power, the compressed-pulse duration deviates farther away from the transform-limited duration, implying a worse compressed pulse quality. Therefore, achieving both high amplified power and good compressed-pulse quality requires optimizing more parameters (e.g., input pulse chirp, bandwidth, and power, Yb-fiber length and doping concentration, and grating pair separation, etc.).

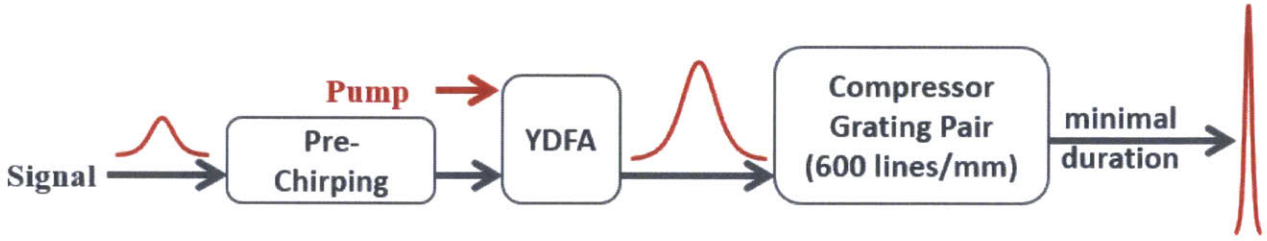

Fig. 3-3. The typical experimental scheme for further optimization.

3.3.1 Optimization of the Input Pulse Pre-Chirp

We first use our model to investigate the effect of the input pulse chirp on the pulse compression with the Yb-fiber length fixed at 2-m. As shown in Fig. 3-3, the signal pulse is pre-chirped, then amplified by a YDFA, and finally compressed to its minimal RMS duration by a diffraction-grating pair. The positive pre-chirp is introduced by propagating the pulse through fused silica with β_2 = 18.9 fs^2/mm and β_3 = 16.5 fs^3/mm; the negative pre-chirp is generated from

a diffraction-grating pair the same as the one in the previous section, with β_2 = -1408 fs^2/mm and β_3 = 2180 fs^3/mm. In the simulation, other parameters remain unchanged from Section 3.2.

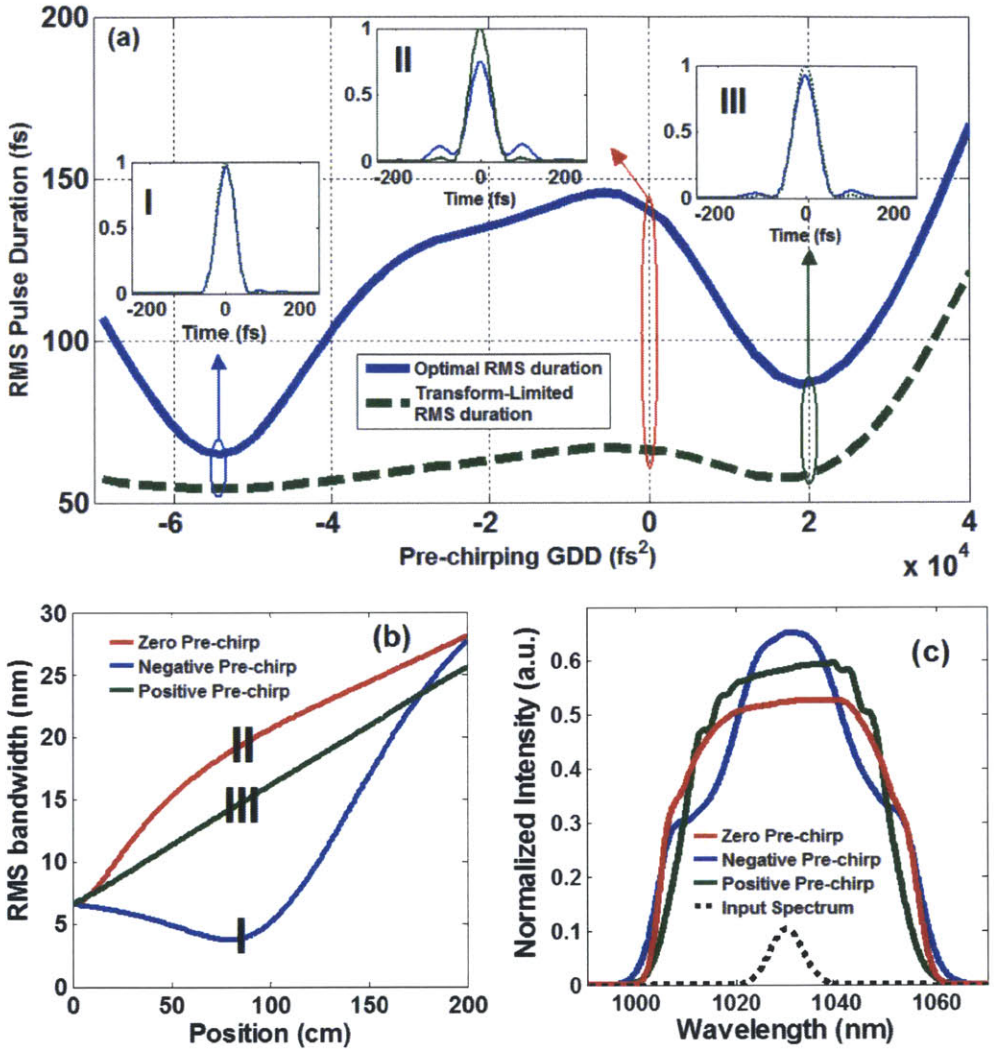

Fig. 3-4. (a) Optimum RMS duration of the compressed-pulse and the corresponding transform- limited RMS duration as a function of pre-chirping GDD for the input pulse. Insets: compressed pulses and transform-limited pulses for three different pre-chirp. (b) bandwith evolution inside the Yb-fiber amplifier. (c) output sepctra for three different pre-chirp.

Figure 3-4 summarizes the simulation results with the total GDD varying from -7×10^4 to 4×10^4 fs^2 for pre-chirping the input signal pulse prior to amplification; hereafter, we refer to such GDD as pre-chirping GDD. While the transform-limited RMS duration (green, dashed line in Fig. 4(a)) slightly varies, the optimum RMS duration for the compressed pulse strongly depends

on the pre-chirping GDD. Insets of Fig. 3-4(a) show the compressed pulse (blue, solid line) and transform-limited pulse (green, dashed line) for three different GDD: (I) -5×10^4 fs^2, (II) 0 fs^2, and (III) 1.9×10^4 fs^2. Figure 3-4(b) illustrates the evolution of RMS bandwidth along the Yb-fiber for these three pre-chirping cases. The characteristics of spectral evolution in the three different GDD cases can be seen more clearly in Fig. 3-5. For a negatively pre-chirped input-pulse (e.g., case I), its spectrum (blue line) experiences an initial spectral compression [55,56] and then subsequent spectral broadening. While the case II (i.e., zero pre-chirp) generates the broadest spectrum in terms of RMS bandwidth, both its transform-limited pulse and the optimum compressed-pulse are longer than the other two cases due to the existence of strong pedestals. This simulations suggests that varying the input pulse pre-chirp leads to different spectra, some of which exhibit considerable temporal pedestals that severely limit the quality of the compressed pulse. This can be clearly seen in Fig. 3-4(c), in which the output spectrum corresponding to negative pre-chirp (shown as blue curve) exhibits less steep wings than the other two cases; the resulting transform-limited pulse has minimal pedestals in general. In this case, there exists an optimum negative pre-chirping GDD that leads to a compressed pulse with the shortest duration close to its transform-limited duration (see case I inside Fig. 3-4(a)).

In fact, this phenomenon appears in mode-locked Yb-fiber oscillators as well. Depending on the amount of net cavity GDD, an Yb-fiber oscillator may operate in different mode-locking regimes (i.e., stretched-pulse, similariton, and dissipative soliton) [64]. For a stretched-pulse Yb-fiber oscillator that features a net cavity GDD close to zero, the intra-cavity pulse prior to entering the gain fiber acquires negative chirp from dispersion over-compensation by optical elements with negative GDD (e.g., diffraction-grating pair, chirped fiber Bragg grating, and hollow-core photonic-crystal fiber). On the contrary, the intra-cavity pulse in similariton or

dissipative soliton Yb-fiber oscillators exhibits positive chirp before entering the gain fiber. Our simulation results presented in Fig. 3-4, despite modeling a single-pass Yb-fiber amplifier, explain why stretched-pulse mode-locking produces better pulse quality than the other two regimes of mode-locking.

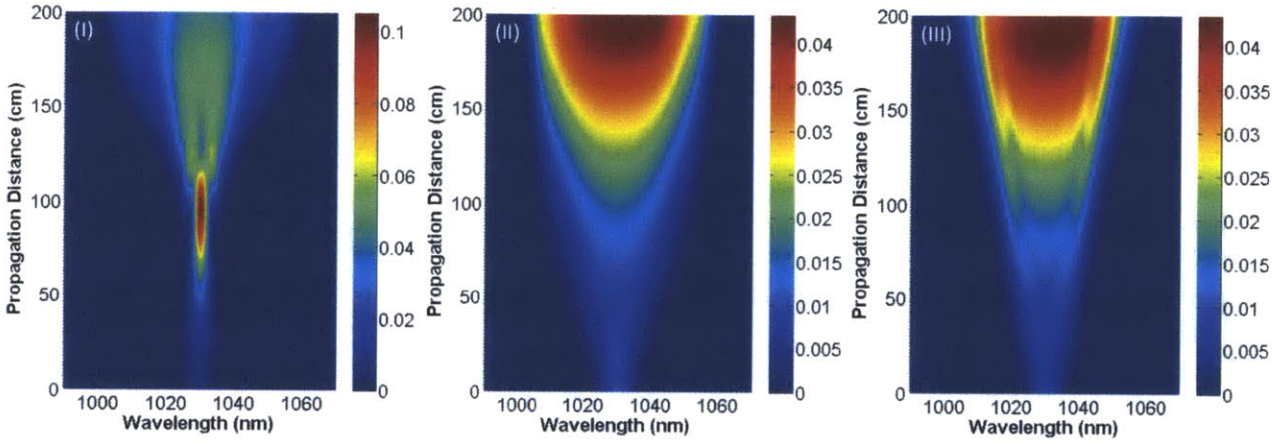

Fig. 3-5. Spectral evolution for three different pre-chirping GDD:
(I) -5×10^4 fs^2, (II) 0 fs^2, and (III) 1.9×10^4 fs^2.

3.3.2 Optimization of the Input Power and Optical Bandwidth

In this subsection, we study the compressed pulse quality as we vary the FWHM duration from 200 fs to 600 fs (i.e., different input optical bandwidth) for an input gaussian pulse before being pre-chirped. The input RMS duration can be calculated from the input FWHM duration by $\tau_{FWHM} = 1.178\tau_{RMS}$. Other parameters such as the fiber length are the same as those in the previous section. For every input power and input transform-limited pulse duration, we scan the pre-chirp to find the optimum compressed-pulse duration.

Figure 3-6 illustrates the optimum compressed duration versus input power for an input pulse with different transform-limited duration. The optimum compressed RMS duration occurs at ~20-mW input power, corresponding to a pulse energy of ~0.25 nJ. For an input power less than 20mW, the optimum compressed duration starts to increase significantly because the accumulated

nonlinearity is too small to broaden the spectrum enough for achieving substantial pulse compression. Even for an input pulse duration of 500 fs, it can be compressed to 63 fs, a factor of 6.7 in RMS duration shortening. That is, as long as we apply a suitable pre-chirp, the RMS duration of the compressed pulse varies slightly as the transform-limited input pulse duration changes from 200 fs to 500 fs. These results indicate that, while the amplified output power is nearly the same (slight difference due to wavelength dependent emission/absorption cross-section) for all cases (~560 mW), the best compressed pulse is achieved by optimizing both the pre-chirp and the input power.

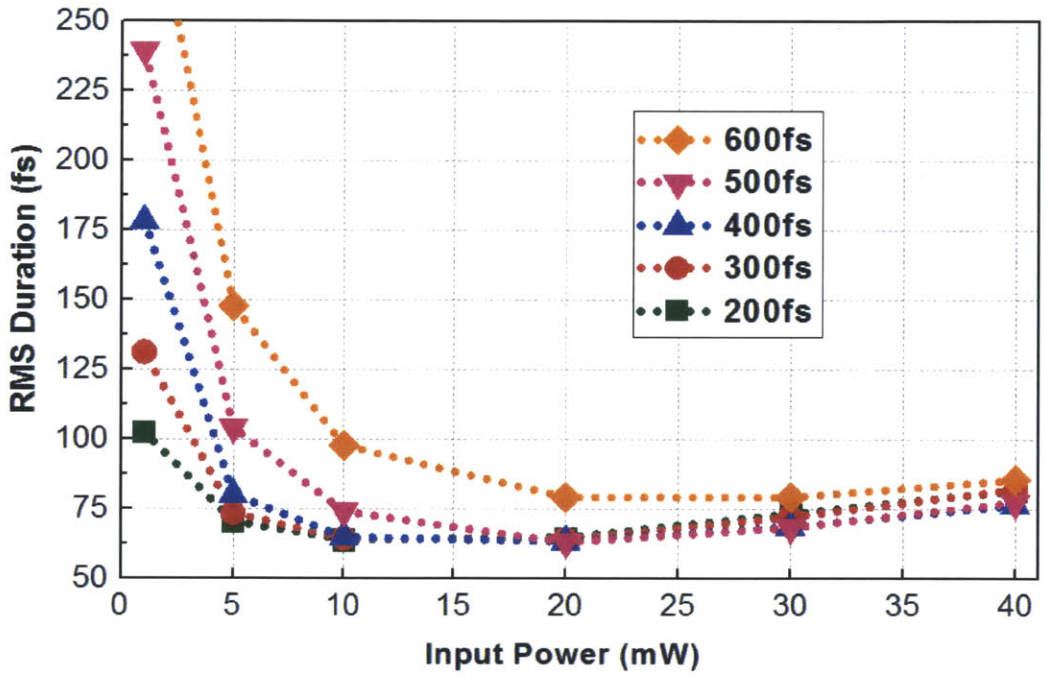

Fig. 3-6. Calculated RMS duration for the optimum compressed-pulse as a function of input signal power for five different spectral bandwidths corresponding to transform-limited pulse FWHM duration of 200 fs, 300 fs, 400 fs, 500 fs, and 600fs.

3.3.3 Optimization of the Yb-ion Doping Concentration

Furthermore, at 20-mW input seed power and 600-mW pump power, we study the effect of three different Yb-ion doping concentrations: $10^{25}/3$ m^{-3}, 10^{25} m^{-3}, and 3×10^{25} m^{-3}. Varying the doping concentration allows us to better understand the interplay between nonlinearity and the

amplifier gain. To get the same amplified power for these three cases, the fiber lengths are chosen to be 6 m, 2 m, 2/3 m, respectively since the amplified power is determined by the product of the Yb-fiber length and its doping concentration. Figure 3-7 shows that, for different transform-limited input-pulse duration, the optimized compressed pulse duration depends on Yb-fiber doping concentration. For a higher doping concentration with shorter fiber-length, the accumulated nonlinearity is reduced. This is a consequence of the reduced effective length of the amplifier. In general, Yb-fiber with higher doping concentration is preferred for the input signal pulse with shorter transform-limited duration.

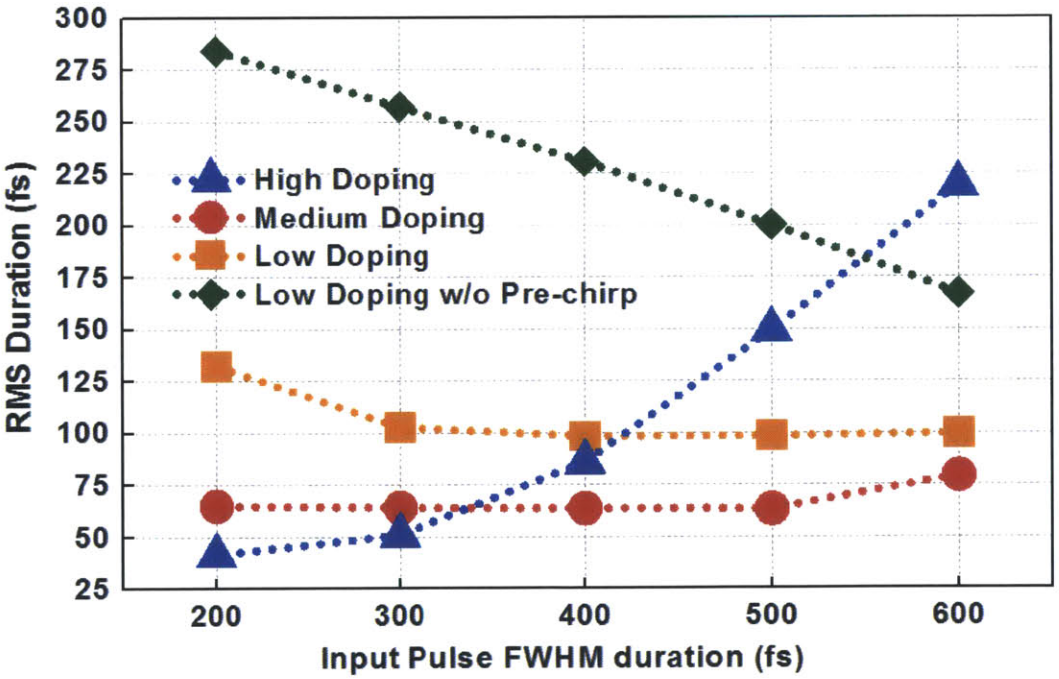

Fig. 3-7. Calculated RMS duration of the optimum compressed pulse as a function of the FWHM pulse duration of the transform-limited Gaussian input pulse for three doping levels: blue-triangle curve for high doping at $10^{25}/3$ m^{-3}; red-circle curve for medium doping at 10^{25} m^{-3}; and black-square curve for low doping at 3×10^{25} m^{-3}. The purple-diamond curve shows the compressed-pulse RMS duration obtained with a low-doping Yb-fiber amplifer seeded with transform-limited pulses.

For a long Yb-fiber (here 6 meters) with low doping concentration, the resulting nonlinear fiber amplifier works in a well-studied regime known as parabolic similariton

amplification; that is, any input pulse to an amplifier constructed from sufficiently long Yb-fiber will asymptotically evolve into a positively chirped pulse with a parabolic temporal profile and propagates inside the fiber amplifier self-similarly [65,66]. Most existing investigations employed a transform-limited pulse at the input, corresponding to the purple-diamond curve in Fig. 3-7. The curve shows that achieving shorter compressed pulses prefers longer transform-limited pulses at the fiber input for low-doped Yb-fibers. The compressed pulse duration can be further reduced if the input pulses are optimally pre-chirped; see the black-square curve in Fig. 3-7. Note that parabolic similariton amplification suffers from limited gain bandwidth and stimulated Raman scattering [67]. These limitations have been numerically studied assuming a finite Lorentzian gain bandwidth [68,69]. With the gain derived from the rate eq. in our model, we can perform a more accurate optimization of parabolic similariton amplification.

3.4. Summary

We use a model —which couples the steady-state-propagation rate eqs. and the GNLSE—to study nonlinear amplification of femtosecond pulses in Yb-fiber amplifiers configured in the co-propagating pump scheme. We investigated these femtosecond Yb-fiber amplifiers to achieve better compressed pulse quality by optimizing the parameters, such as the input pulse pre-chirp and power, input pulse bandwidth, and Yb-fiber doping concentration. The results show that, in general, a negative pre-chirp achieves the best compression, as is verified experimentally.

The presented study has practical applications. For example, we have demonstrated a fundamentally mode-locked Yb-fiber oscillator emitting ~206 fs pulses with 15-pJ pulse energy and 3-GHz repetition rate [21]. Stabilization of the oscillator's repetition rate and the carrier-envelope phase offset will result in a femtosecond frequency comb with 3-GHz line spacing. Such a large line spacing is desired in many spectral-domain applications, e.g., frequency combs

optimized for precision calibration of astronomical spectrographs [28–33]. Stabilization of the carrier-envelope phase offset using the well-known 1f-2f heterodyne detection technique involves generation of low-noise supercontinuum using ~100-fs (or even shorter) pulses with ~1-nJ pulse energy. Both our theoretical and experimental results enable us to construct an optimized Yb-fiber amplifier followed by a proper compressor to achieve these pulse requirements from the initially long (~206 fs) and weak (15 pJ) oscillator pulses.

Chapter 4

Frequency Comb based on a 280-MHz Narrowband Yb-fiber Oscillator

4.1. Motivation

To experimentally validate the pre-chirp management method introduced in Chapter 3, we build a 280-MHz narrowband Yb-fiber oscillator and tried to achieve high pulse energy and short compressed pulse duration after YDFAs with the aid of the pre-chirp management. Furthermore, based on this method we couple the optimal compressed pulse into a highly nonlinear fiber to generate octave-spanning SC for further f_{CEO} detection. Finally, a 280-MHz frequency comb based on a narrowband Yb-fiber oscillator is demonstrated. The demonstrated 280-MHz frequency comb based on a narrowband oscillator should lay the basis for building the 3-GHz fiber laser frequency comb.

4.2. Background of High Rep-rate Frequency Comb

Femtosecond laser frequency combs are femtosecond mode-locked lasers with their repetition rate (f_{rep}) and carrier-envelope offset frequency (f_{CEO}) phase-stabilized to a frequency standard [7]. Many applications (e.g., optical arbitrary waveform generation and calibration of astronomical spectrographs) demand frequency combs with line spacing >10 GHz such that each individual comb-line can be accessed. Such a requirement has stimulated recent research

endeavors in developing femotosecond lasers with >1 GHz repetition rate. Although 10 GHz repetition-rate operation has been achieved in a Kerr-lens mode-locked Ti:sapphire laser (and frequency comb) [34], scaling up repetition-rate is being intensively pursued in femtosecond lasers incorporating Yb-doped gain materials which can be directly diode-pumped and exhibit excellent power scalability [21,36,37,70–74].

Table 4-1. A survey of diode pumped, mode-locked Yb femtosecond lasers with >1 GHz repetition rate. SBW: spectral bandwidth at FWHM, τ_p (T_L): transform-limited pulse duration (assuming sech^2 pulse), SAM: saturable absorber mirror.

f_{rep}	SBW	τ_p (T_L)	Mode-locker	Gain medium	Year	Reference
1.0 GHz	4.8 mm	240 fs	SBR	Yb:KYW	2009	[70]
1.0 GHz	7.0 nm	160 fs	SBR	Yb:fiber	2012	[39]
1.0 GHz	3.8 nm	280 fs	SBR	Yb:KYW	2012	[72]
2.8 GHz	7.5 nm	150 fs	SBR	Yb:KYW	2012	[36]
4.6 GHz	11.0 nm	105 fs	Kerr-lens	Yb:KYW	2012	[73]
4.8 GHz	4.1 nm	396 fs	SBR	Yb:KGW	2009	[37]
4.9 GHz	2.1 nm	800 fs	SBR	Yb:glass	2013	[74]
15 GHz	2.1nm	811 fs	SBR	Yb:glass	2012	[75]

A survey of high repetition-rate (>1 GHz) femtosecond lasers with Yb-doped gain media (Table 4-1) shows that most of these lasers are of relative narrow bandwidth supporting pulse durations well-exceeding 100 fs. The only exception is the Kerr-lens mode-locked Yb:KYW laser reported in Ref. 8, which produces 105 fs pulses. In addition to the lack of self-starting, such a laser employs minimal output coupling in favor of Kerr-lens mode-locking and thus produces only 6 pJ pulse energy [8]. Other femtosecond lasers in Table 4-1 are all capable of self-starting with mode-locking initiated and stabilized by a saturable absorber mirror (SAM); however the produced

pulses feature narrowband and long transform-limited pulse duration as a result of reduced nonlinear effects due to the lower intra-cavity pulse energy for GHz repetition rate. Especially for repetition rates ≥3 GHz, the SAM mode-locked lasers produce optical bandwidths of ≤5.5 nm, corresponding to ≥200 fs transform-limited pulses.

In implementing a self-referenced frequency comb, stabilization of f_{CEO} is rather challenging. It normally involves nonlinearly broadening the laser spectrum inside a highly nonlinear fiber to generate supercontinuum (SC) spanning an octave. f_{CEO} is then detected by heterodyning the short-wavelength edge of the SC with a frequency-doubled copy of the long-wavelength edge. A high-quality SC featuring excellent coherence is crucial to achieve a low-noise f_{CEO} that ensures a stable frequency comb. Detailed experiments and numerical simulations have found that the SC coherence is primarily determined by the input pulse duration coupled into the nonlinear optical fiber [11]. As a rule of thumb, pulses of 100 fs (or even shorter) produce SC with good coherence to detect and stabilize f_{CEO}. Therefore, it is not surprising that most demonstrated frequency combs are based on lasers with direct output of <100 fs pulses. As for multi-GHz lasers featuring long output pulses (≥200 fs), the following question naturally arises: is it possible to fully stabilize narrowband lasers to achieve self-referenced frequency combs possessing multi-GHz line spacing?

This question has been partly addressed in Ref. [76] by comparing f_{CEO} detection using octave-spanning SC generated by pulses of different duration. The SC generated from 290 fs pulses exhibits poor coherence and f_{CEO} is not detectable. As the 290 fs pulses are first spectrally broadened and then compressed to 100 fs using a passive fiber-compressor, the spectral coherence of the resulting SC is substantially improved, and consequently f_{CEO} is detected showing a signal-to-noise ratio (SNR) >27 dB at 100 kHz resolution bandwidth (RBW) [76]. However the

authors did not reference the f_{CEO} to a frequency standard to demonstrate a fully stabilized frequency comb.

In this chapter, using the pre-chirp management method, a self-referenced frequency comb based on a 280 MHz narrowband Yb-fiber oscillator which is intentionally mode-locked with output spectral bandwidth of 5-nm corresponding to 415 fs transform-limited pulses. Differently from the passive compression of the long pulses, we employ a nonlinear Yb-fiber amplifier which amplifies the narrowband pulses as well as broadens their optical spectrum. The power amplified and spectrally broadened pulses are then compressed prior to SC generation. To optimize the f_{CEO} signal, we optimize the nonlinear pulse amplification by pre-chirping the pulses at the amplifier input. An optimum negative pre-chirp exists that produces the best-quality compressed pulse for SC generation and leads to a detected f_{CEO} signal with 35 dB SNR measured with 100 kHz RBW. We phase stabilize the f_{CEO} using a frequency shifting method [77], which results in 0.64-rad (integrated from 1 Hz to 10 MHz) phase noise for the in-loop error signal.

4.3. Narrowband 280 MHz Yb-Fiber Oscillator

The 280 MHz Yb-fiber oscillator, schematically shown in Fig. 4-1, is configured as a linear cavity pumped by a 976-nm single-mode laser diode up to 600 mW average power (JDSU 30-7602-660). The laser cavity consists of an 8.3-cm highly doped Yb-fiber (Coractive SCF-YB550-4/125-19) to provide gain and three dispersion-compensating mirrors (DCM) for managing the cavity dispersion. The flat end of the gain fiber is firmly attached to a dichroic mirror that transmits pump and reflects the intra-cavity lasing beam. The wave plates and polarization beam cubes allow six bounces of the optical beam from the DCMs per round trip; each bounce leads to a negative group velocity dispersion of -2000 fs^2/mm [51]. A SAM with < 1 ps recovery time and 15% modulation depth initiates and stabilizes the mode-locking.

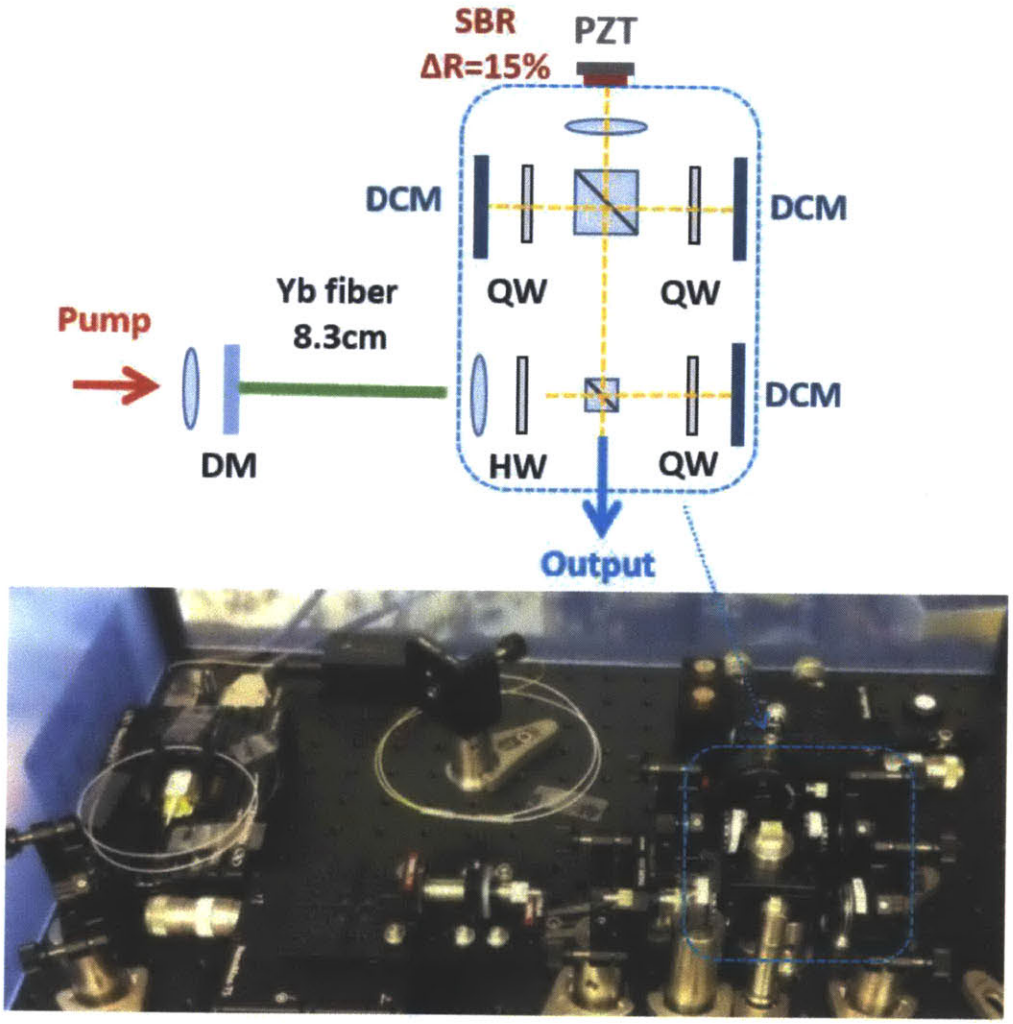

Fig. 4-1. (Top) Schematic setup of the 280MHz Yb-fiber oscillator. DM: dichroic mirror, HW: half-wave plate, QW: quarter-wave plate, DCM: dispersion compensating mirror, PZT: piezo-electric transducer, and SBR: saturable Bragg reflector. (Bottom) Photo of the 280MHz Yb-fiber oscillator.

Mode-locking self-starts at a pump power of 250 mW. With 350 mW pump power, the oscillator outputs 90 mW average power with 5 nm bandwidth (FWHM) centered at 1028 nm, shown as the black curve in Fig. 4-2. This spectrum supports 415 fs transform-limited pulses. We measured the relative intensity noise (RIN) of the oscillator in a coarse enclosure. The integrated RIN (often referred to as instability) from 1 Hz to 10 MHz is 0.3%. The RIN of the laser oscillator showed considerable environmental disturbances (e.g. mechanical resonance, air current,

temperature drifting) which, however, can be effectively suppressed using better isolation of the laser from the environment.

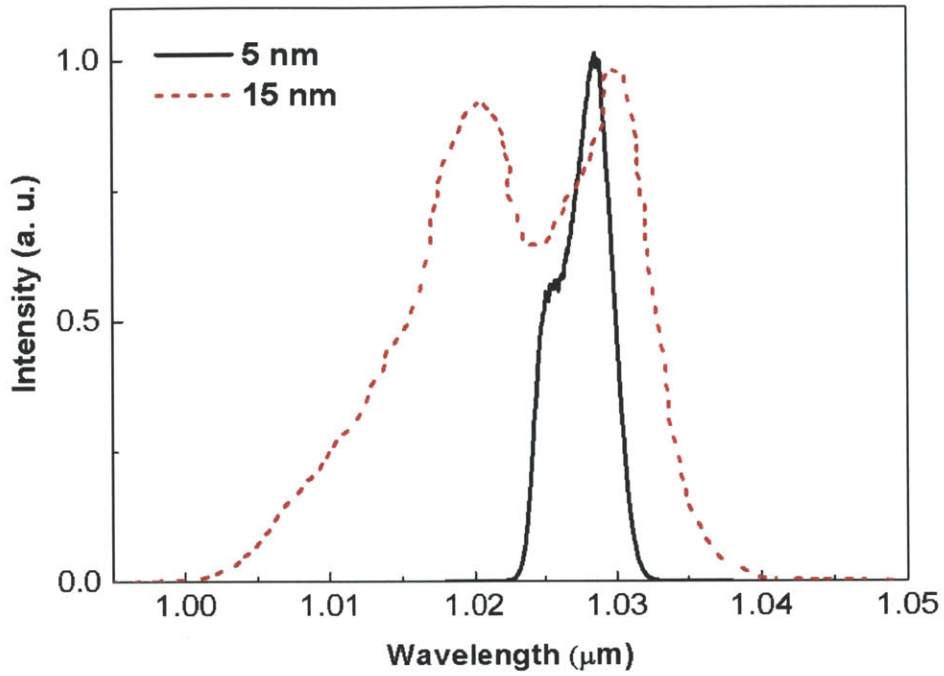

Fig. 4-2. Narrowband (black solid curve) and broadband (red dotted curve) spectra of the modelocked 280 MHz Yb-fiber oscillator.

By adjusting the output coupling ratio with the half-wave plate and choosing different SAMs, we can mode-lock the oscillator with different output bandwidths. For example, use of a different SAM generates a 15-nm bandwidth shown as the red-dotted curve in Fig. 4-2. To demonstrate the feasibility of achieving frequency combs from narrowband oscillators, we intentionally run the oscillator with 5-nm bandwidth during our experiments.

4.4. Experimental Results on Pre-Chirp Management for Optimizing Compressed Pulse Quality

To validate the pre-chirp management method experimentally, Fig. 4-3 shows the experimental setup, consisting of a 280 MHz oscillator serving as a seed source, a diffraction grating pair to adjust the pre-chirp of the input pulse at the input of the Yb-doped fiber amplifier,

and finally another diffraction-grating pair to compress the amplified pulse to the shortest pulse duration. The output pulse from the oscillator has a duration of 2.1 ps with ~6 nm FWHM bandwidth centered at 1030 nm. Since the pulse is positively chirped, use of a grating pair (600 grooves/mm) providing negative chirp allows to continuously tune the input-pulse pre-chirp from positive to negative by changing the separation of the grating pair. The pre-chirped pulses are coupled into the YDFA including a 2-m Yb-fiber (Nufern SM-YSF-LO) pumped by two laser diodes (Oclaro LU962UF76-20R) combined with a polarization beam combiner. The amplified pulses are compressed by the second grating pair to the shortest pulse duration.

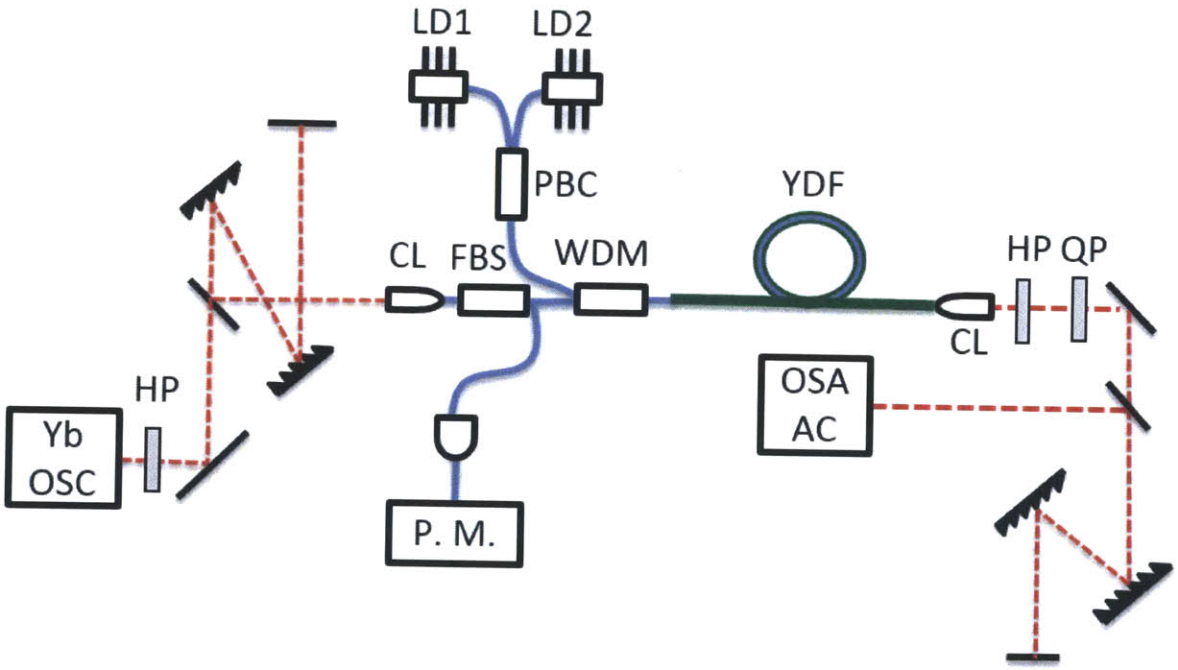

Fig. 4-3. Experimental set-up. OSC: oscillator, HP: half-wave plate, QP: quarter-wave plate, CL: Coupling lens, FBS: fiber beam splitter, LD: laser diode, PBC: polarization beam combiner, WDM: wavelength division multiplexer, YDF: Yb doped fiber, OSA: optical spectrum analyzer, AC: autocorrelator, and P.M.: power meter.

With the fixed 20-mW input power, we achieved amplified pulses of 600-mW average power at 1-W pump power. We varied the pre-chirp by changing the separation of the first grating pair and then adjusted the second grating pair to compress the amplified pulses to its shortest FWHM

duration measured by an autocorrelator. We recorded the compressed-pulse spectra as we varied pre-chirp and then calculated from these spectra the RMS duration of the transform-limited pulses. Such a RMS duration was plotted in Fig. 4-4 as a function of pre-chirping GDD. Figure 4-4(b) plots the input pulse spectrum (black dashed curve) and three compressed-pulse spectra corresponding to different pre-chirping GDD: -6.3×10^4 fs^2 (orange curve), -1.8×10^4 fs^2 (blue curve), and 1.0×10^4 fs^2 (red curve).

For all three cases, the input spectrum is broadened from ~6 nm to >20 nm. However, the shape of the amplified pulse spectrum varies substantially with different pre-chirp, and in turn supports a different transform-limited pulse duration. The black scattered curve shows that the minimum duration is achieved at a negative pre-chirping GDD of -6.3×10^4 fs^2. Also plotted in Fig. 4-4(a) are the autocorrelation traces for the three compressed pulses corresponding to these three pre-chirping GDDs. The FWHM of these autocorrelation traces are 134 fs, 149 fs, and 169 fs, respectively. Apparently, the best compression quality occurs at the pre-chirping GDD of -6.3×10^4 fs^2 with a measured autocorrelation trace of 134-fs, suggesting a de-convolved pulse of ~100 fs. Deviation from this optimum pre-chirp degrades the compressed-pulse quality featuring an increased temporal pedestal. The spectra in Fig. 4-4(b), similar to the results shown in Fig. 3-4(c), show that, as we vary the pre-chirping GDD from the optimum value of -6.3×10^4 fs^2 to -1.8×10^4 fs^2 and then to 10^4 fs^2, the corresponding spectra start to develop sharper edges, which leads to larger pedestal for the compressed pulses. Note that there are two sections of HI1060 single mode fibers before (2.45m) and after (0.33 m) the YDFA. These two fibers would introduce excessive nonlinearity. Hence further optimization of parameters other than pre-chirp is needed to achieve even shorter pulse duration.

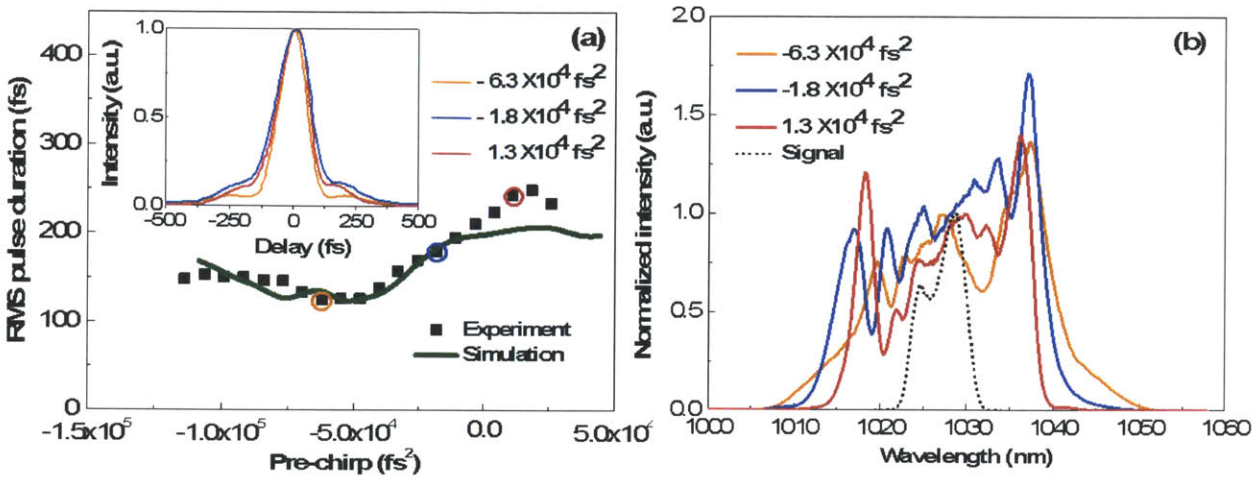

Fig. 4-4. (a) Calculated RMS pulse duration of optimum compressed pulses from the measured spectrum (black scattered) and simulated curve (green line). The shortest autocorrelation (AC) trace is achieved at the lowest RMS pulse duration. τ_{AC} (FWHM) =134 fs for a pre-chirping GDD of -6.3×104 fs², τ_{AC} (FWHM) =149 fs for -1.8×10⁴ fs², and τ_{AC} (FWHM) =169 fs for 1×10⁴ fs² respectively. (b) The spectra corresponding to three AC traces in (a). The pulse has the largest spectral bandwidth and smoothest edge for the pre-chirping GDD of -6.3×104 fs².

The green curve in Fig. 4-4(a) shows the simulation results from numerically modeling of the experimental setup. It can be seen that the modeling and experimental measurements agree well for the negative pre-chirp regime. The difference between experiment and simulation can be mainly attributed to the fact that the emission/absorption cross-section, the doping concentration, and the modal overlap factors of the pump/signal mode, Γ_p and Γ_s, are just assumed rather than experimentally derived. In the simulation, we neglected the higher-order (>2) spectral phase of the initial 2.1-ps pulse. Nevertheless, our model correctly predicts the overall tendency of the measurements: there exists an optimum pre-chirp that results in the shortest compressed pulse.

4.5. Frequency Comb based on the narrowband Yb-fiber oscillator

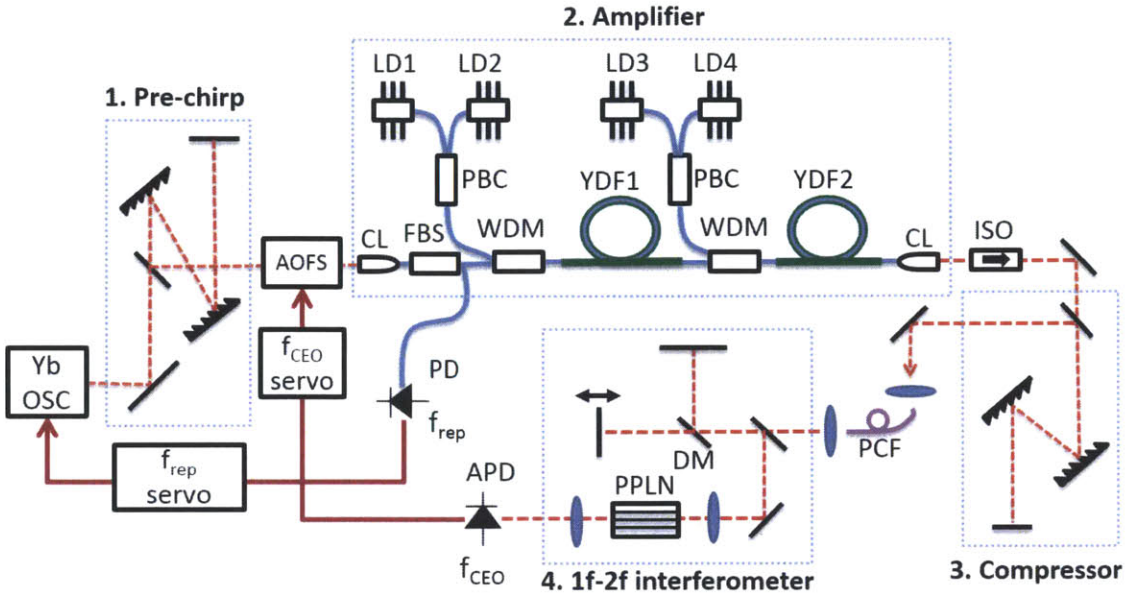

Fig. 4-5. Fully stabilized frequency comb based on a 280-MHz narrowband Yb-fiber oscillator. OSC: oscillator, AOFS: acousto-optic frequency shifter, PD: photo-detector, CL: collimating lens, PBC: polarization beam combiner, WDM: wavelength division multiplexer, YDF: Yb-doped fiber, ISO: isolator, DM: dichroic mirror, PCF: photonic crystal fiber, PPLN: periodically poled lithium niobate, and APD: avalanche photo-detector.

Having demonstrated the pre-chirp management method theoretically and experimentally, we move on to construct a frequency comb out of this 280-MHz narrow bandwidth oscillator. This experimental part was mostly done by a postdoc, Jinkang Lim, in our group. Figure 4-5 shows the setup of the self-referenced frequency comb by stabilizing the repetition rate f_{rep} and the carrier-envelope offset frequency f_{CEO} of the narrowband Yb-fiber oscillator. The stabilization is achieved by four optical building blocks: (1) a grating pair for pre-chirp management prior to the nonlinear amplification, (2) a 2-stage Yb-fiber nonlinear amplifier to boost power and broaden the optical spectrum, (3) another grating pair for pulse compression of the amplified pulses, and (4) a 1f-2f interferometer to generate the f_{CEO} signal which is stabilized using a feed-forward method based on an acousto-optic frequency shifter (AOFS) [52].

4.5.1 Pre-chirp Management for Spectral Broadening and Pulse Compression

In general, one needs >1 nJ pulses with <100 fs duration for low-noise SC generation in a highly nonlinear optical fiber to detect the f_{CEO} signal with high enough SNR. Here we employ a 2-stage Yb-fiber amplifier to amplify the oscillator pulses as well as spectrally broaden their optical spectrum. This nonlinear amplification, however, may add strong nonlinear phase shift causing optical pulse break-up and phase noise owing to amplitude-to-phase noise conversion and amplified spontaneous emission. Therefore the amplifier has to be optimized for improving the compressed pulse quality. In Chapter 3, we have investigated, by detailed numerical modeling, the dependence of compressed pulse quality on the fiber amplifier parameters including input pulse chirp, duration, and power, and the gain fiber's doping concentration and length [22]. The simulation results verified by experiments indicate that pre-chirping the oscillator pulse prior to the nonlinear amplification plays a critical role for optimizing the system to achieve high-quality compressed pulses. In particular, an optimum negative pre-chirp exists for the best pulse compression quality.

In Fig. 4-5, the diffraction-grating (groove density of 600 lines/mm) pair before the Yb-doped fiber amplifier (YDFA) provides a variable pre-chirp for the pulses to be amplified. The grating pair has a dispersion of -1500 fs^2/mm with 60% transmission efficiency at the Littrow incident angle. Each of the 2-stage YDFA is constructed with a 2-m Yb-fiber forward-pumped by two 650 mW laser diodes (centered at 976 nm) combined with a polarization beam combiner. The pre-chirped oscillator pulses are amplified up to 1.4 W and become 1 W after the isolator, and then 550 mW after the grating-pair compressor.

Because SC generation is extremely sensitive to the intensity noise of the driving pulses [78–80], we measured the RIN of the amplified pulses at different pre-chirp settings. Figure 4-6(a) shows the integrated RIN from 100 Hz to 10 MHz as a function of the group-delay dispersion (GDD) for pre-chirping the oscillator pulses. Indeed, the integrated RIN reaches a minimum of 0.075% at the pre-chirp GDD of -0.09 ps^2 (indicated by the blue circle in Fig. 4-6(a)). For comparison, it increases to 0.093% at the pre-chirp GDD of 0.01 ps^2 (red circle in Fig. 4-6(a)). Figure 4-6(b) plots the RIN spectra corresponding to these two pre-chirp GDDs (i.e., -0.09 ps^2 versus 0.01 ps^2), indicating that the RIN is considerably reduced especially at higher frequency (>10 kHz) for the pre-chirp GDD at -0.09 ps^2 (blue curve in Fig. 4-6(b)) compared with the case of applying 0.01 ps^2 GDD (green curve in Fig. 4-6(b)).

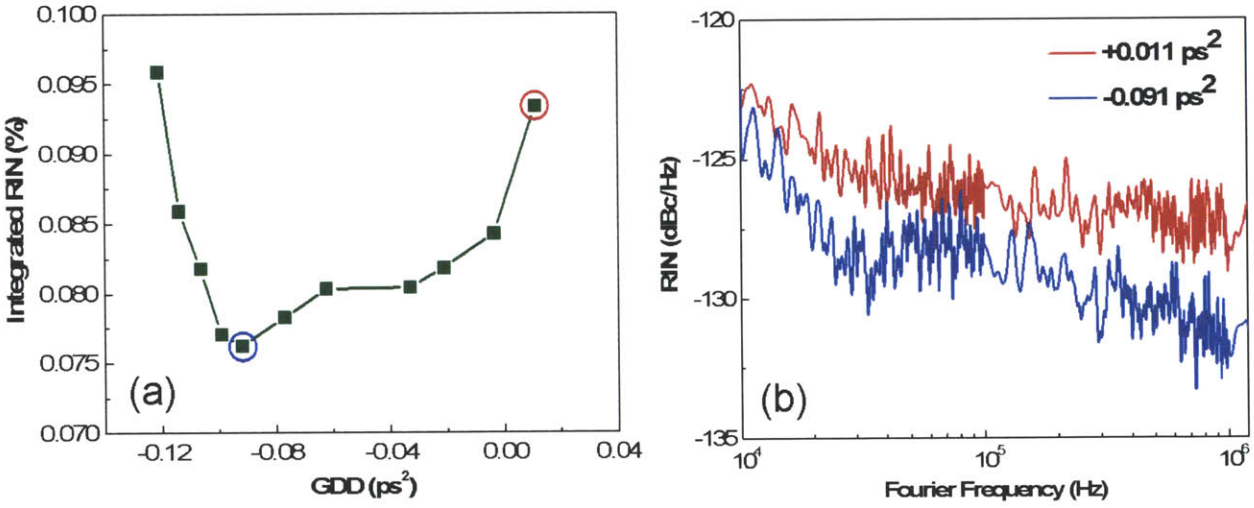

Fig. 4-6. (a) Instability (i.e., integrated RIN) for the amplified pulses as a function of pre-chirping GDD. Black-dotted line: oscillator instability. (b) RIN for different pre-chirp GDD: +0.01 ps^2 (red curve) and -0.09 ps^2 (blue curve).

With the pre-chirp GDD of -0.09 ps^2 where the minimum RIN is achieved for the amplified pulses, the compressed pulses reach the minimum duration as well. The red curve in Fig. 4-7(a) shows the corresponding optical spectrum at the amplifier output, showing that the nonlinear amplification broadens the oscillator spectrum (blue dashed curve in Fig. 4-7(a)) from 5 nm to

>15 nm; such a broadened spectrum accommodates a transform-limited pulse of 90 fs. We measured the resulting compressed pulse using an autocorrelator and the autocorrelation trace is shown in Fig. 4-7(b) as the red curve. For comparison, the autocorrelation trace of the transform-limited pulse calculated from the broadened spectrum is plotted in the same figure as the blue curve. The good overlap between the two autocorrelation traces indicates that the compressed pulse has 86% pulse energy in the main peak.

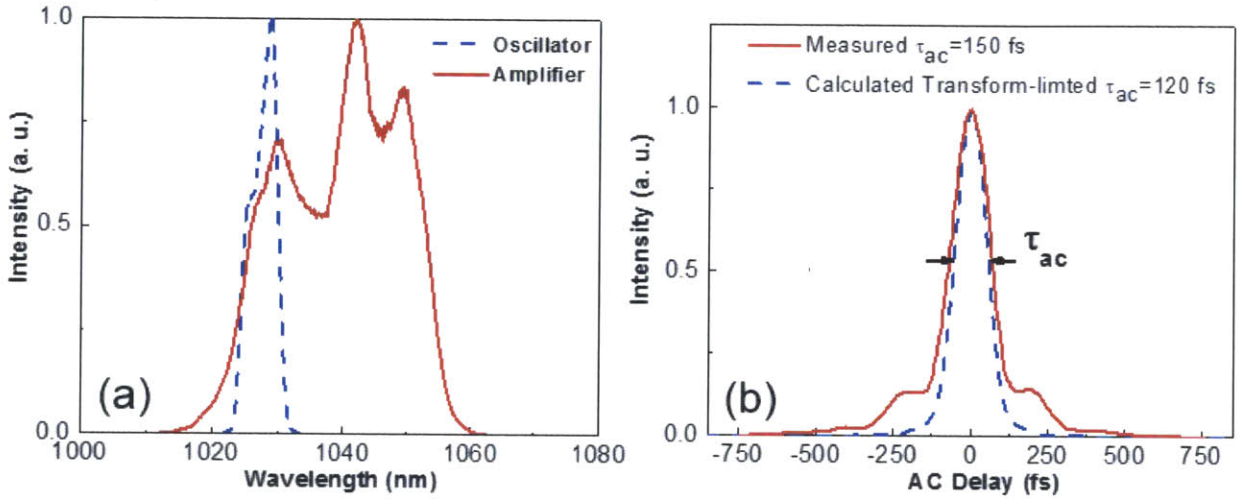

Fig. 4-7. (a) Oscillator spectrum (blue-dashed curve) and spectrum after the amplifier (red curve). (b) Experimentally measured autocorrelation trace for the amplified pulses (red curve). Blue curve shows the autocorrelation trace of the transform-limited pulse calculated from the amplified spectrum in (a).

4.5.2 Supercontinuum Generation and f_{CEO} Detection

The pre-chirp optimized compressed pulses with >15 nm bandwidth were coupled into 40-cm long photonic crystal fiber (NKT photonics NL-3.2-945) with 1-nJ input pulse energy. The generated SC spans from 660 nm to 1400 nm as shown in Fig. 4-8(a). The SC is launched into a 1f-2f interferometer which includes a periodically-poled lithium niobate (PPLN) crystal for second harmonic generation (SHG) of the 1360 nm wavelength range. The group delay mismatch between the fundamental frequency and the SHG frequency was compensated by a tunable delay path. Figure 4-8(b) shows the heterodyned f_{CEO} beat-note detected by a Si-avalanche photo-detector.

With a SNR of ~40 dB, the f_{CEO} signal exhibits a Lorentzian line-shape with a free-running linewidth of <140 kHz (FWHM), which is typical for fiber laser combs [81].

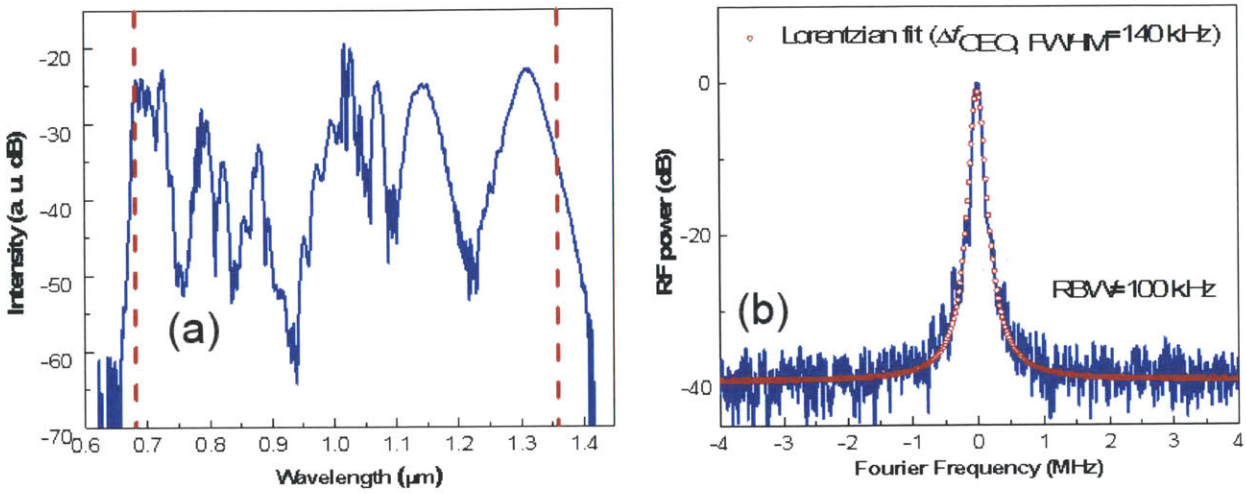

Fig. 4-8. (a) Octave spanning supercontinuum generation using 40-cm PCF. The two dashed red lines indicate the wavelengths for 1f-2f interferometer. (b) Measured f_{CEO} (x-axis: f_{CEO} −190 MHz) and its linewidth with RBW=100 kHz.

4.5.3 Stabilization of f_{rep} and f_{CEO}

f_{rep} is stabilized by controlling the cavity length using a fast single stack PZT attached to the back of the SAM. Long-term f_{rep} stabilization is ensured using a slow PZT to move the translation stage on which the SAM is mounted. To control f_{CEO}, we implement a frequency shifting technique via an AOFS in feedback configuration, providing broader control bandwidth than that of pump power modulation and allowing for decoupling of the f_{CEO} stabilization [77,82] from the laser dynamics and repetition rate lock. The first order diffracted beam is shifted by applying a RF signal which is generated from a voltage controlled oscillator and then amplified by a linear RF power amplifier. For f_{CEO} stabilization, the f_{CEO} beat-note was bandpass-filtered, amplified, and then heterodyned with a local RF synthesizer; the resulting heterodyned signal was bandpass-filtered, divided with a pre-scaler, and fed into a digital phase detector which is able to track a $\pm 32\pi$ phase

difference. The signal was finally compared with another local RF synthesizer in the phase detector to generate the error signal to control the AOFS for a complete feedback loop.

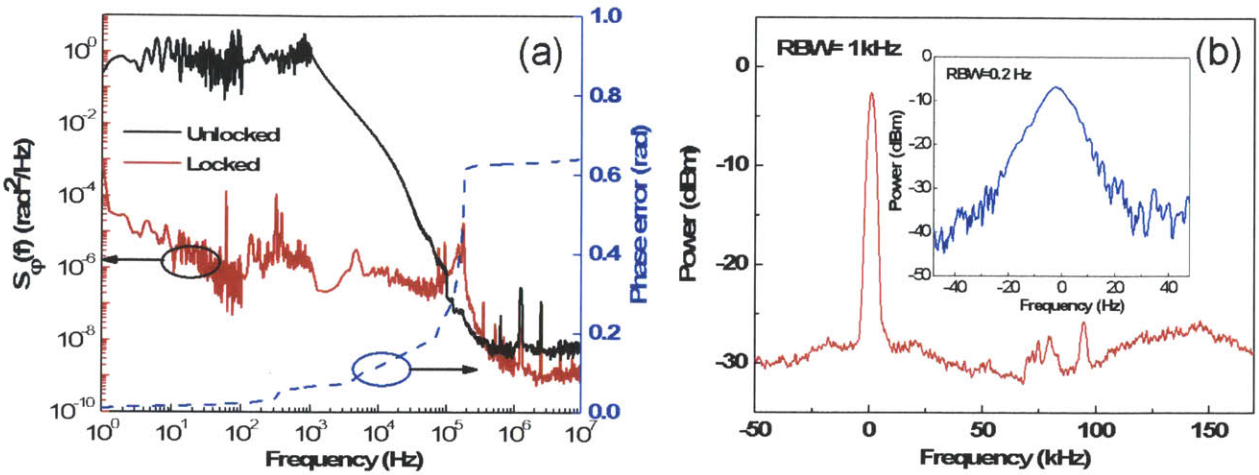

Fig. 4-9 (a) Power spectral density (PSD) and the RMS integrated phase noise; unlocked (black), locked (red), Phase error calculated by integrating noise PSD from 1 Hz to 10 MHz (blue). (b) Measured f_{CEO} linewidth (x-axis: f_{CEO} - 190 MHz) with 1 kHz RBW; Inset with 0.2 Hz RBW.

Figure 4-9(a) presents the noise power spectral density, $S_\varphi(f)$ [rad^2/Hz], of the in-loop error signal when f_{CEO} is locked (red curve) or unlocked (black curve). With the phase-locked loop closed, the frequency noise of the error signal is substantially suppressed, showing a locking bandwidth of 150 kHz. The integrated RMS phase noise from 1 Hz to 10 MHz is 0.64 rad. As Fig. 4-9(b) shows, the corresponding f_{CEO} linewidth is <10 Hz with the resolution bandwidth of 0.2 Hz. The frequency shifting method suppresses broadband technical noise and further noise suppression can be achieved by isolating the comb from environmental disturbances, by implementing an active intensity noise eater in the oscillator [82], or by adding a phase compensation circuit to increase the servo-bandwidth.

4.6. Summary

In conclusion, based on the experimentally validated pre-chirp management method we have demonstrated a well-stabilized frequency comb by phase-stabilizing a 280 MHz narrowband Yb-fiber laser. The narrowband output pulses were pre-chirped, then spectrally broadened in an Yb-fiber amplifier, and finally compressed to ~100 fs in duration. Also, based on the experience and techniques building this 280 MHz frequency comb, we should be able to apply these techniques to building a self-referenced Yb-fiber laser frequency comb based on the 3 GHz, fundamentally mode-locked Yb-fiber oscillator introduced in Chapter 2 [21].

Chapter 5

3 GHz High Power Femtosecond Laser System

5.1. Introduction

In this chapter, we employ the pre-chirp management for building a >12 W high power 3-GHz femtosecond laser system. Such a laser system enables us to demonstrate an ultrafast few-cycle source at the Ti:sapphire wavelength (Chapter 6), a Watt-level femtosecond tunable Raman soliton source (Chapter 7), and a 3 GHz fiber laser frequency comb via difference frequency generation.

5.2. Experimental Setup

Figure 5-1 shows the schematic setup of the high power 3-GHz laser source, mainly consisting of: 1) a 3-GHz fundamentally mode-locked Yb-fiber oscillator [21], 2) a two-stage polarization-maintaining (PM) fiber amplifier to pre-amplify the oscillator pulses, 3) a diffraction-grating pair for pre-chirp management prior to further power amplification [22], 4) a double-clad Yb-fiber power amplifier, and 5) a transmission-grating pair to compress the amplified pulses.

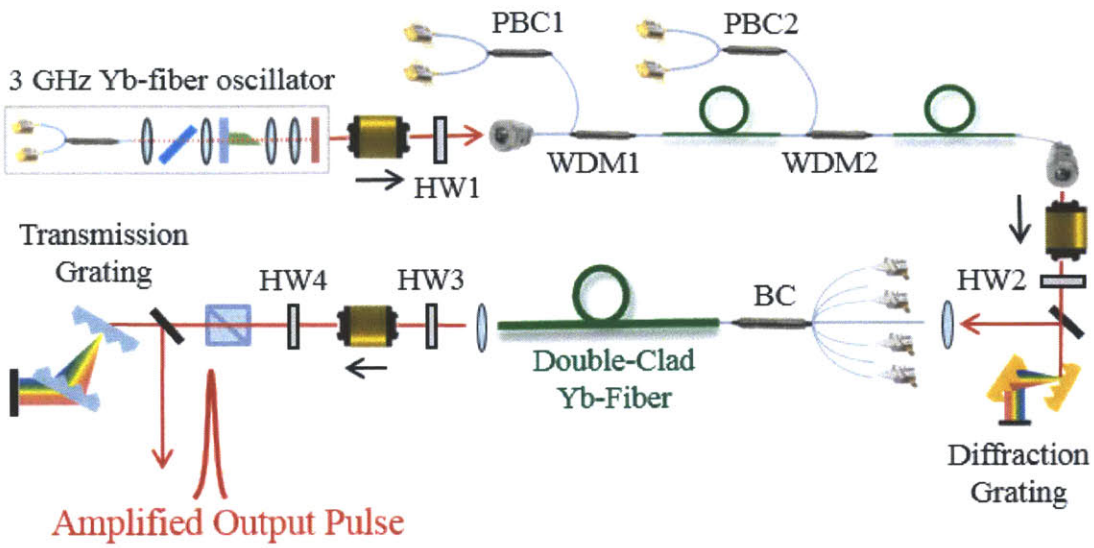

Fig. 5-1. Schematic setup of the 3-GHz high power femtosecond laser system. HW: half-wave plate; PBC: polarization beam combiner; BC: (6+1) x 1 beam combiner; SPF: short-wavelength-pass optical filter that only transmits wavelength components below 950 nm; and DCM: double-chirped mirror.

The 3-GHz Yb-fiber oscillator, centered at 1027 nm with 3.5 nm bandwidth (blue line in Fig. 5-2), produces 32 mW average power. The design and implementation of such a 3-GHz Yb-fiber oscillator has been described in Ref. 13. The output pulses are amplified to 1.05 W by a two-stage pre-amplifier constructed from single-mode PM fibers; the resulting optical spectrum is broadened to 7 nm (red line in Fig. 5-2).

5.2.1 Pre-Chirp Management on High Power Yb-Fiber Amplifier

Before the pre-amplified pulses enter the power amplifier, we employ the pre-chirp management method to achieve high-quality compressed pulses after the power amplifier. The pulses are pre-chirped by a diffraction-grating (600 line/mm) pair, and then amplified by a power amplifier constructed from 2.4-m double-clad PM Yb-fiber (LIEKKI Yb1200-10/125) spliced to a PM (6+1) x 1 beam combiner. In the beginning, the amplifier optimization is done with 12W output power. A 600 line/mm gold reflection grating pair as a pre-chirper and a 1250 line/mm transmission grating pair as a compressor.

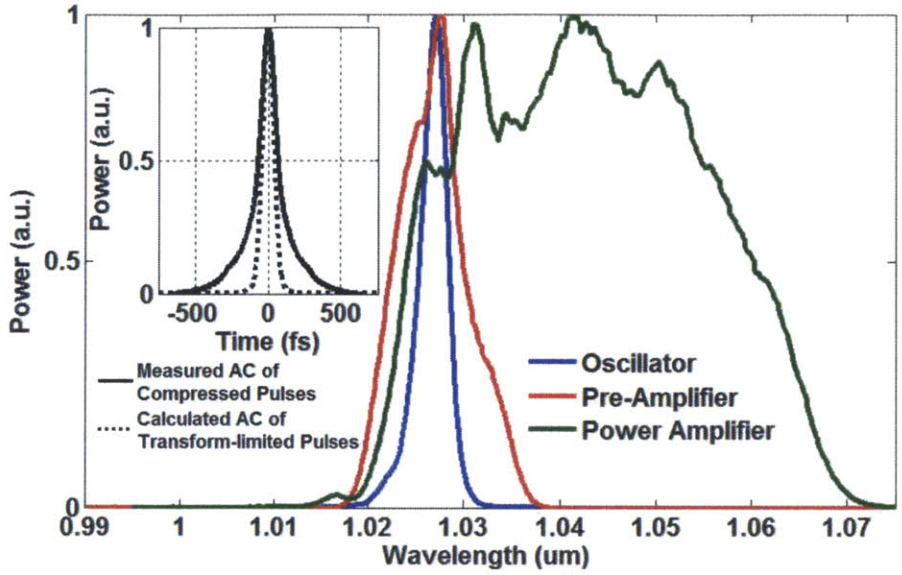

Fig. 5-2. Optical spectra at the output of the 3-GHz oscillator (blue line), pre-amplifier (red line), and power amplifier (green line), respectively. Inset: measured autocorrelation (AC) trace of the optimal compressed pulses after the power-amplifier (black solid line) and the calculated autocorrelation trace of the transform-limited pulse (black dotted line).

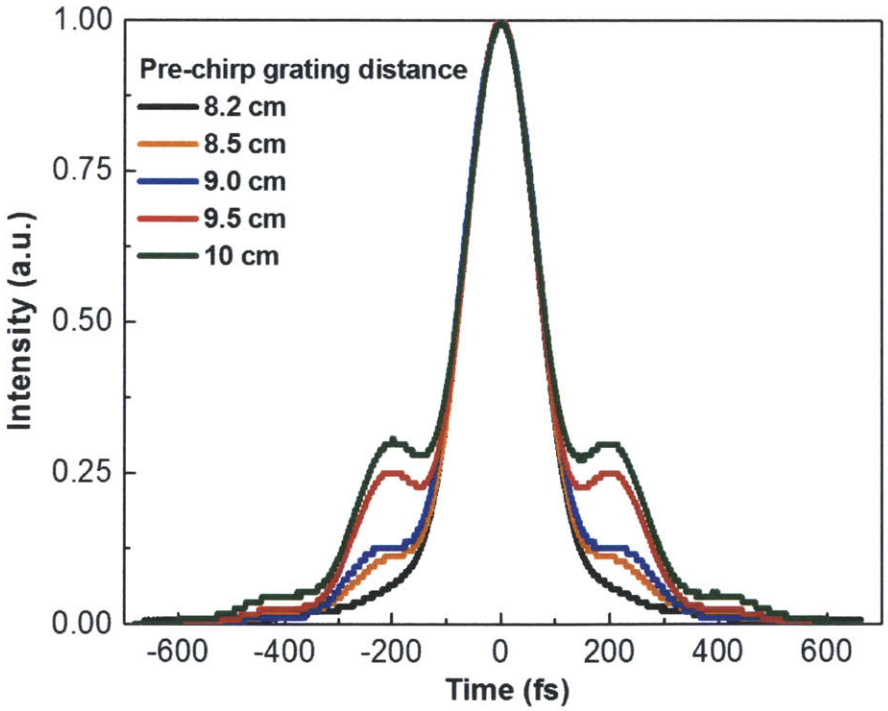

Fig. 5-3. The shortest autocorrelation traces at different pre-chirp grating distance.

Figure 5-3 shows the shortest autocorrelation traces at different pre-chirp grating distances. It is clearly seen that even though the FWHMs of the autocorrelation traces are similar (~158 fs),

the pedestals can be reduced dramatically by the pre-chirp management method. This again significantly shows the benefit from the pre-chirp management method.

5.2.2 Optimized 3-GHz High Power Laser System

To further achieve even better compressed pulse quality, the compressor is replaced by a 1000 line/mm transmission-grating pair which has a transmission efficiency >85%. By further optimizing the input power and pre-chirping the pre-amplified pulses, we achieve compressed pulses with 12-W average power and the measured autocorrelation trace is 140 fs in duration shown as the solid curve in the inset of Fig. 5-2. The amplified pulses are spectrally broadened to 30-nm bandwidth (green line in Fig. 5-2) during the amplification and are then compressed by a 1000 line/mm transmission-grating pair (LightSmyth LSFSG-1000). As a comparison, the autocorrelation trace of the transform-limited pulse calculated from the optical spectrum is plotted as the dotted curve, showing an autocorrelation duration of 95 fs. Figure 5-4 shows the output power of the power amplifier after the compressor vs. the pump power.

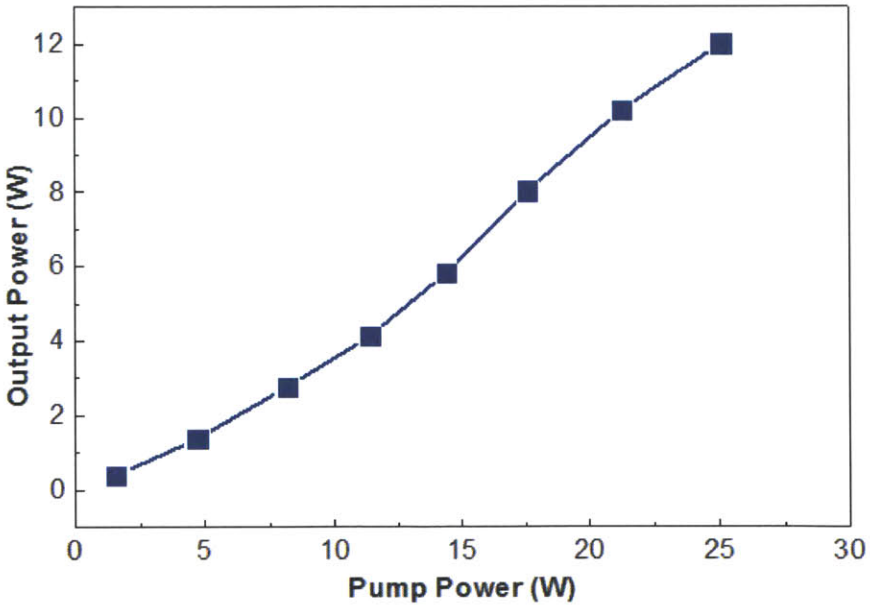

Fig. 5-4. The output power of the power amplifier after the compressor vs. the pump power.

5.3. Noise Performance

The performance of (1) the relative intensity noise (RIN) and (2) the timing jitter of the 3-GHz laser system is critical in further finding f_{CEO} and therefore making a self-referenced frequency comb [80,81,83]. In the next two subsections, we show the RIN noise and timing jitter of the 3 GHz laser system.

5.3.1 Relative Intensity Noise

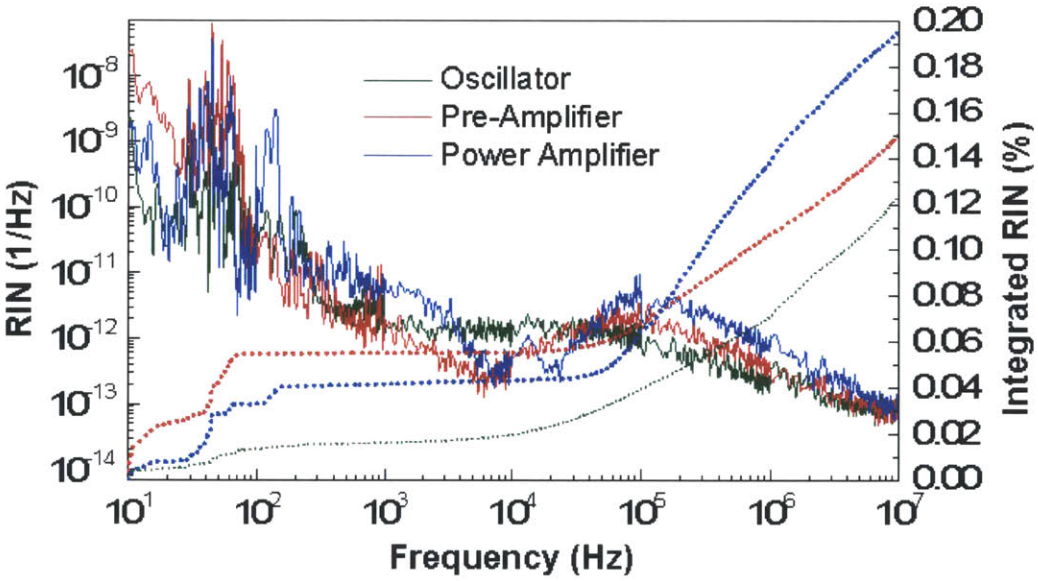

Fig. 5-5. Measured RIN and the integrated RIN at the output of the oscillator, pre-amplifier, and power amplifier.

Relative intensity noise (RIN), the noise power normalized to the average power level, is an indicator of the power instability of a laser [84]. In the 280-MHz laser system only single-mode diodes are used, whereas in the 3-GHz laser system four multimode pump diodes (JDSU L4-9897603-100F) are employed in the high power double-clad Yb-fiber amplifier. Multimode pump diodes are much noisier than single mode diodes in terms of intensity noise. The laser output is detected by the photodetector (Thorlabs DET20C) and fed into the vector signal analyzer (HP 89410A) in order to measure the intensity noise. We compare the measured

integrated relative intensity noise from 10 Hz to 10 MHz of the 280 MHz system and the 3-GHz system. The integrated RIN of the 280 MHz system in Fig. 4-6 is <0.1% while that of the 3-GHz system is ~0.6 %. It is noteworthy that even the 3-GHz oscillator itself has an integrated RIN of ~0.1%. Because of the necessity of using multimode diodes in the high power 3-GHz laser system, reducing the intensity noise of this laser system becomes extremely challenging. Nonetheless, after carefully optimization of the whole system by tuning the operating temperature and currents of all diodes including oscillator pump diodes, the integrated RIN of the 3-GHz laser system is eventually reduced to <0.2% as shown in Fig. 5-5.

5.3.2 Timing Jitter and f_{rep} Locking

Timing jitter describes the phenomenon that the output pulses from a modelocked laser exhibit some deviation of the temporal pulse positions from those of a periodic pulse train. The sources of timing jitter in a modelocked laser have been previously studied and summarized in Haus and Mecozzi's seminal paper [85].

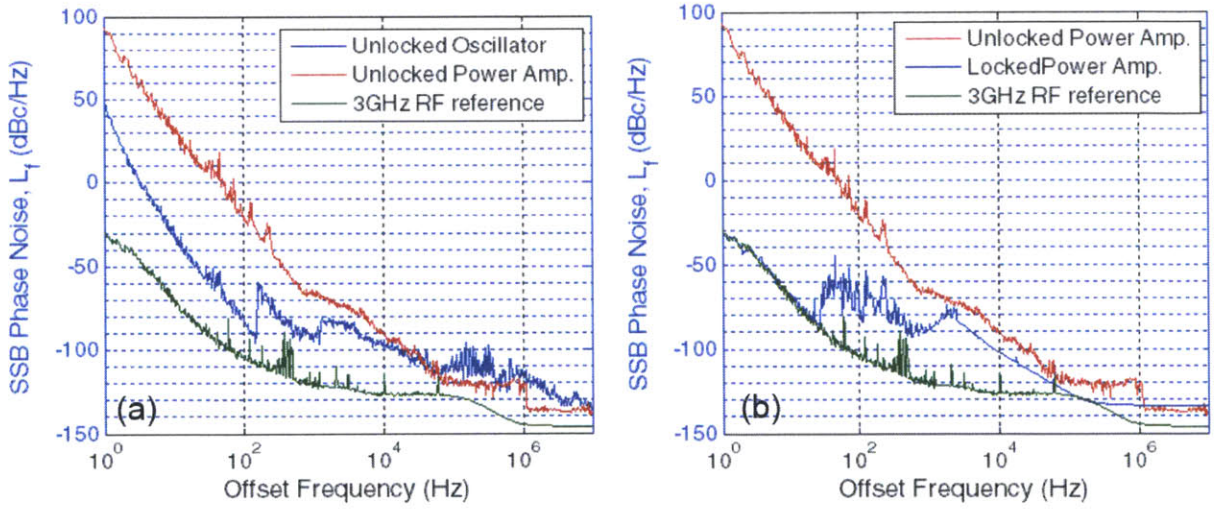

Fig. 5-6. (a) Single side band phase noise of the unlocked oscillator (blue) and the unlocked power amplifier (red). (b) Single side band phase noise of the locked oscillator (blue) and the locked power amplifier (red).

Figure 5-6 shows the measurement of the single side band (SSB) phase noise of the first harmonic (3 GHz) of the laser. The laser output power is focused on a photodetector (EOT ET-3500), the output of which is filtered by a bandpass filter, and amplified before being measured with the signal source analyzer (Agilent E5052). When the oscillator's repetition rate is unlocked, the phase noise measurements of oscillator's output pulses and power-amplifier's output pulses are shown in Fig. 5-6(a). We can see that the phase noise (<10 kHz) of the power amplifier is much larger than that of the oscillator. This is mainly because the intensity noise of the multimode diodes in the power amplifier results in the amplification of the phase noise of the amplified output pulses.

For a high rep-rate oscillator, the round-trip length of an n-GHz oscillator is n times shorter than a 1-GHz laser. If there is a slight change in the cavity length of an n-GHz oscillator, it would lead to n^2-time frequency drift in the repetition rate compared with the drift in a 1 GHz oscillator; that is, the timing jitter of an n-GHz oscillator would have n^2 amount of timing jitter compared with that of a 1 GHz oscillator. Therefore, reducing the timing jitter requires to stabilize the repetition rate of the 3 GHz Yb-fiber oscillator.

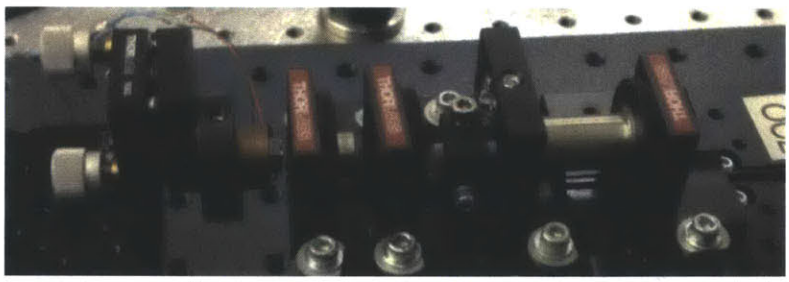

Fig. 5-7. The photo of the saturable absorber mounted on a PZT for f_{rep} locking.

As shown in Fig. 5-7, we add a fast single stack PZT attached to the back of the SAM so that *f*rep can be stabilized. The f_{rep} locking scheme is shown in Fig. 5-8. For f_{rep} stabilization, the output

pulses detected by the fast photodetector (EOT ET-3500A) is bandpass-filtered, amplified, and mixed with a local RF synthesizer (Agilent E8257D) using a double balanced mixer. The mixed signal is lowpass–filtered and then connected to the servo controller (New Focus LB1005) to generate the error signal to control the PZT for a complete feedback loop.

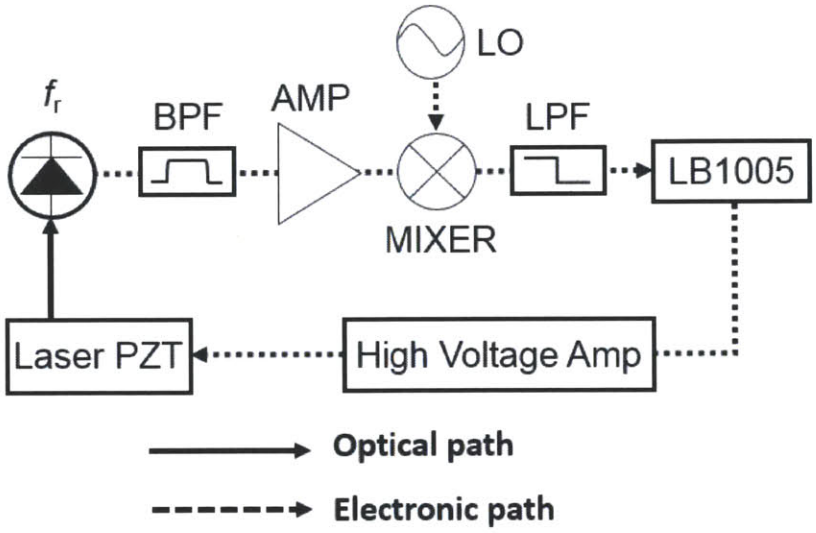

Fig. 5-8. The f_{rep} locking scheme of the 3 GHz oscillator.

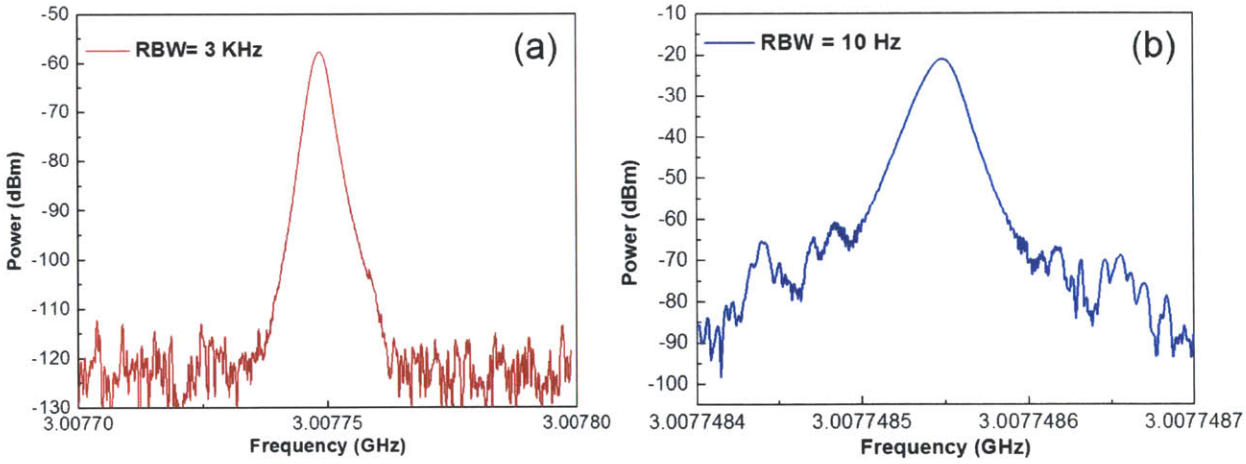

Fig. 5-9. (a) Unlocked f_{rep} with 3 kHz RBW and 100 KHz span. (b) Locked f_{rep} with 10 Hz RBW and 300 Hz span.

The phase noise measurements of amplified pulses with the oscillator's repetition rate locked and unlocked are shown in Fig. 5-6(b). The low frequency part (<20 Hz) of the phase noise is

>100 dB reduced to that of the local RF synthesizer. The locking bandwidth is ~1 kHz. However, the servo box offers too much gain in the low-frequency part such that the phase noise between 20 Hz and 1 kHz is not reduced to that of the RF synthesizer. To improve this, we would need to start with a better enclosure of the oscillator and the 3 GHz high power laser system to reduce the low frequency noise. Figure 5-9 shows the RF spectra for locked f_{rep} and unlocked f_{rep}. By the Lorentzian fitting, the linewidth of the unlocked f_{rep} is ~11 kHz while that of the locked f_{rep} is ~75 Hz.

5.4. Summary

We demonstrate a >12-W (> 4-nJ) 3-GHz Yb-fiber laser system with compressed pulse duration of ~100 fs. This system can be readily applied to the generation of other useful ultrafast sources as described in the following chapters. Moreover, the short compressed pulse duration <100 fs satisfies the rule of thumb for that needed to produce SC with good coherence. The construction of the 3-GHz frequency comb should be promising.

Chapter 6

Application I: 3 GHz Yb-fiber Laser Based Few-Cycle Source at the Ti:sapphire Wavelength

6.1. Motivation

Kerr-lens mode-locked Ti:sapphire lasers have become the workhorses of the field of ultrafast optics. Due to the remarkable gain bandwidth ranging from 650 to 1100 nm, Ti:sapphire lasers with precise cavity-dispersion management emit optical pulses as short as 5 fs—the record short optical pulses ever directly generated from mode-locked lasers [15]. Besides countless time-domain applications utilizing the extremely short pulses, the wavelength range covered by Ti:sapphire lasers is of particular importance for many applications. For example, ultrafast Ti:sapphire lasers are the dominant light source in the field of nonlinear optical microscopy largely because optical pulses with wavelength around 800 nm are able to excite a wide range of important fluorophores via two-photon absorption [1].

Despite their extreme success, the lack of efficient and direct diode pumping has hampered the wide use of Ti:sapphire lasers outside research laboratories, which has spurred much research effort in developing alternative laser sources. One attractive candidate is the diode-pumped mode-locked laser based on Cr^{3+}-doped colquiriite crystals such as Cr^{3+}:LiSAF [86], Cr^{3+}:LiSGaF [87],

and Cr^{3+}:LiCAF [88]. These solid-state lasers provide broadly tunable ultrashort pulses around 800 nm with duration as short as ~10 fs [89,90].

In this chapter, we demonstrate a compact ultrafast source centered at 850 nm with >200-nm bandwidth (full width at half maximum) based on a 3-GHz Yb-fiber master-oscillator-power-amplifier system. The output pulses (with up to 13 W average power) from the laser system are coupled into short (<50 mm) pieces of photonic crystal fibers to excite broadband fiber-optic Cherenkov radiation; the resulting broad phase-matching bandwidth due to short fiber length produces up-converted spectrum spanning the wavelength range of 750-950 nm with an average power of 94 mW, 184 mW, and 380 mW for fiber lengths of 28 mm, 37 mm, and 48 mm, respectively. The spectrum generated from the 37 mm fiber is then de-chirped by 8 double-chirped mirrors, leading to compressed pulses of ~14 fs in duration. Such an ultrafast source is a promising substitute for multi-GHz mode-locked Ti:sapphire lasers for applications in optical frequency metrology and multi-photon coherent microscopy.

6.2. Frequency Up-Conversion using Fiber-Optic Cherenkov Radiation

The presented alternative source is derived from an ultrafast Yb-fiber laser. The state-of-the-art Yb-fiber oscillators are able to produce ultrashort pulses centered at 1.03 μm with duration less than 10 optical cycles after external compression [91,92]. To generate few-cycle pulses at the Ti:sapphire laser wavelength range, we perform frequency up-conversion using fiber-optic Cherenkov radiation (FOCR) inside a short piece of photonic crystal fiber (PCF). As ultrashort pulses propagate in a PCF with anomalous dispersion (or GDD < 0), they emit dispersive waves due to the high-order fiber dispersion—a phenomenon known as FOCR [92–95]. Depending on the sign of the third-order dispersion (TOD), the dispersive wave may locate in the wavelength region shorter (for positive TOD) or longer (for negative TOD) than the input-pulse's center

wavelength [96,97]. FOCR has become a wavelength conversion technique [98–100], for example, to extend a Ti:sapphire laser's near-infrared output into the visible wavelength range with applications for biophotonics, carrier-envelope phase control of ultrashort pulses, and calibration of astrophysical spectrographs using high-precision frequency combs (known as astro-combs), to name a few [101–103]. Most of the reported results produce narrowband (10-20 nm), isolated FOCR spectra [99,100,104].

Despite originating from the $\chi^{(3)}$ nonlinear susceptibility of an optical fiber, FOCR shares a universal feature with other well-known $\chi^{(2)}$nonlinear effects (e.g., second-harmonic generation): they all require phase-matching to achieve efficient power conversion. In a previous study, our group has introduced the concept of *coherence length* L_c to quantify the FOCR bandwidth and its dependence on the PCF length [105,106]. Our experimental results using an octave-spanning Ti:sapphire laser as the driving source reveal that an optimum fiber length exists to maximize the FOCR bandwidth [106].

FOCR can be accurately modeled by the generalized nonlinear Schrödinger equation (GNLSE) that takes into account dispersion, self-phase modulation, self-steepening, and stimulated Raman scattering [60]:

$$\frac{\partial A}{\partial z}+\left(\sum_{n=2}^{\infty}\beta_n\frac{i^{n-1}}{n!}\frac{\partial^n}{\partial T^n}\right)A=i\gamma\left(1+\frac{i}{\omega_0}\frac{\partial}{\partial T}\right)\left(A(z,T)\int_0^{\infty}R(t')\left|A(z,T-t')\right|^2dt'\right),$$

where $A(z,t)$ represents the input pulse's amplitude envelope. $\beta_n=\dfrac{\partial^n\beta(\omega)}{\partial\omega^n}$ is evaluated at the central frequency ω_0 of the input pulse. γ is the nonlinear parameter of the fiber and $\beta(\omega)$ the fiber's dispersion curve. $R(t)$ describes both the instantaneous electronic and delayed molecular responses (i.e. SRS) of fused silica, and is defined as $R(t)=(1-f_R)\delta(t)+f_R[(f_a+f_c)h_a(t)+f_bh_b(t)]$.

Typical values of f_R, f_a, f_b, and f_c are 0.245, 0.75, 0.21, and 0.04, respectively [107]. Isotropic Raman response $h_a(t)$ and anisotropic Raman response $h_b(t)$ are defined as $h_a(t)=\Theta(t)(\tau_1^2+\tau_2^2)/(\tau_1\tau_2^2)exp(-t/\tau_2)sin(t/\tau_1)$ and $h_b(t)=\Theta(t)(2\tau_b-t)/\tau_b^2 bexp(-t/\tau_b)$, where τ_1, τ_2, and τ_b have values of 12 fs, 32 fs, and 96 fs, respectively. $\Theta(t)$ is the Heaviside step function.

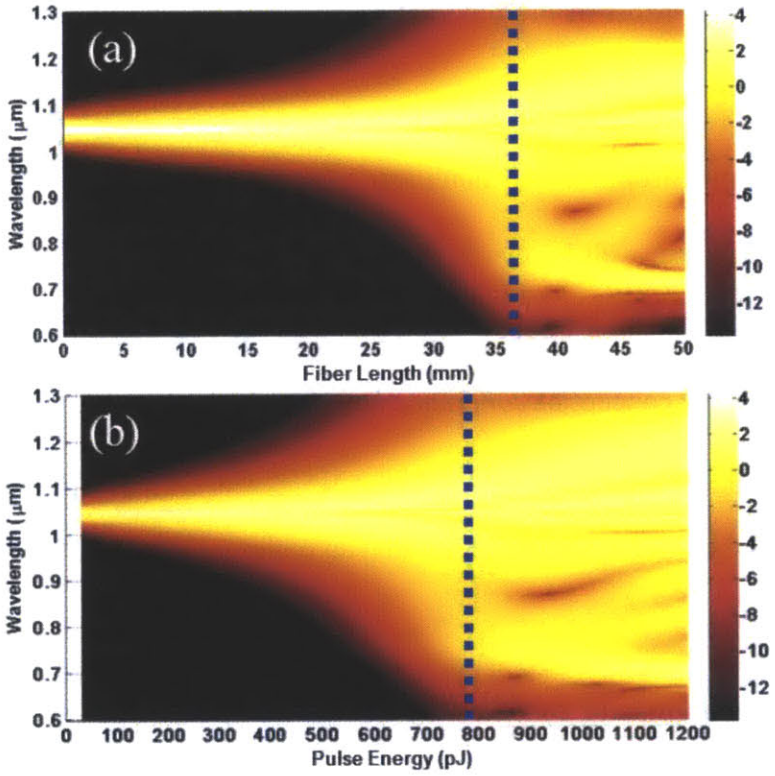

Fig. 6-1. Simulation of FOCR by solving the GNLSE. (a) FOCR evolution versus fiber length assuming 780 pJ input pulse energy. The blue dashed line marks the 37-mm fiber length where a broadband FOCR continuum forms. (b) FOCR evolution versus pulse energy for a PCF of 3.7 cm in length. The blue dashed line marks the 780-pJ pulse energy where a broadband FOCR continuum forms. The spectral intensity in both figures is presented on a logarithm scale.

To be consistent with the following experimental results, we simulated an optical pulse centered at 1.045 μm propagating inside PCF NL-3.2-945 available from NKT Photonics. The fiber exhibits zero-dispersion at 0.945 μm. Figure 6-1(a) shows the spectral evolution along the fiber length for an input Gaussian pulse with 110 fs full-width-half-maximum (FWHM) and 780 pJ energy. Beyond 2.5 cm, the optical spectrum starts to rapidly extend to the shorter

wavelength region; at the 3.7-cm fiber length (indicated by the dashed line), a broadband continuum forms at the shorter wavelength side reaching 700 nm in wavelength. Further propagation leads to an isolated and slowly blue-shifting FOCR, and its bandwidth becomes narrower due to a decreased phase-matching bandwidth for longer fiber length. Figure 6-1(b) shows another simulation with the fiber length fixed at 3.7 cm and the input pulse energy varied. The spectrum evolution in Fig. 6-1(b) follows a similar pattern as is in Fig. 6-1(a), and shows that a broadband FOCR develops for input pulse energy around 780 pJ designated by the dashed line.

Simulation results also show that for 110-fs input pulses, the FOCR accounts for ~10% of the input pulse energy, resulting in a FOCR pulse of ~100 pJ. For a typical 100-MHz repetition rate, the corresponding FOCR source produces an average power of ~10 mW, one order of magnitude less than can be typically achieved from a Ti:sapphire laser at the same repletion-rate. Therefore, to achieve comparable average power we can use our 3-GHz Yb-fiber laser system to generate the FOCR ultrafast source.

6.3. Proof-of-Principle Experiment with a 29 MHz Yb-Fiber Laser

We first perform a proof-of-principle experiment based on a 29-MHz ultrafast Yb-doped fiber oscillator [108]. Yb-doped fiber oscillators can be implemented in many variants. Depending on the amount of net intra-cavity dispersion, they may operate at different mode-locking regimes (i.e. soliton, stretched-pulse, similariton, and dissipative soliton) with the intra-cavity pulse duration ranging from sub-ps to ~10 ps [109,110]. Appendix B gives more detail about the modelocked Yb-fiber at different mode-locking regimes by simulation. These oscillators normally emit positively chirped pulses, requiring external compression to reach their transform-limited duration. Due to the relatively narrow Yb-fiber gain bandwidth (~40 nm), most Yb-fiber oscillators

produce pulses with duration >50 fs after external compression. Intentionally increasing intra-cavity nonlinearity can overcome the gain narrowing effect and generate optical pulses with much broader spectral width, which accommodates even shorter compressed pulses. However, such a strong nonlinear intra-cavity spectral broadening usually generates structured output spectra with highly nonlinear phase, rendering pulse compression extremely difficult to reach the transform-limited duration. Nonetheless, Yb-doped fiber oscillators incorporating substantial spectral broadening and precise external pulse compression have produced ~20-fs pulses albeit with considerable temporal pedestals [91,92]. To validate the generation of high-quality few-cycle pulses at the Ti:sapphire laser wavelength rage, we successfully perform frequency upconversion of an Yb-doped fiber oscillator using fiber-optic Cherenkov radiation (FOCR); the resulting ultrafast source produces ~11-fs pulses centered at 850 nm with 170-nm spectral width at 29 MHz repetition rate.

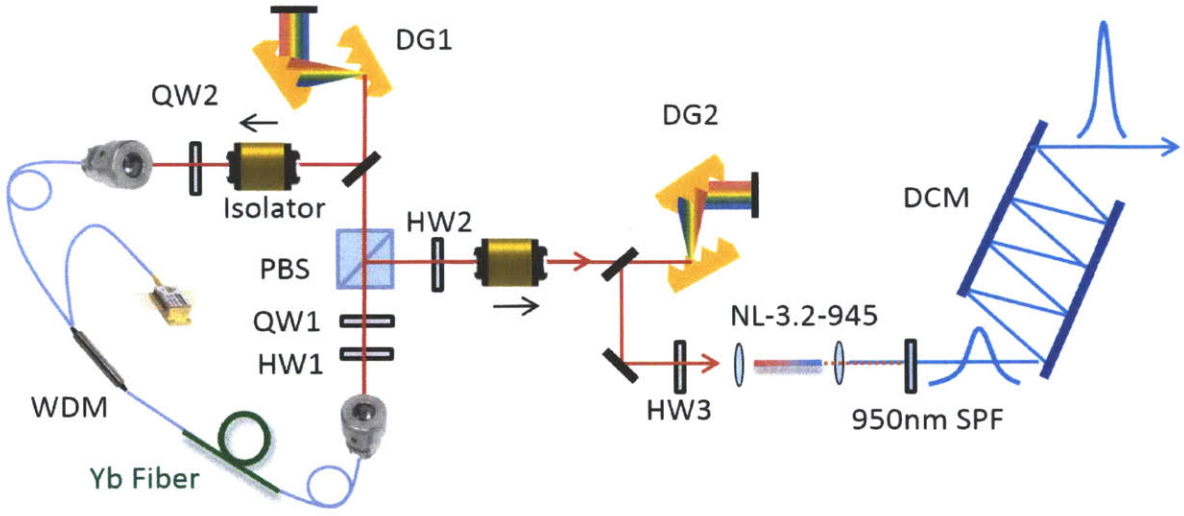

Fig. 6-2. Schematic setup of the generation of 11 fs pulses. QW: quarter-wave plate; HW: half-wave plate; PBS: polarization beam splitter; DG: diffraction grating pair; SPF: 950-nm short-pass filter; and DCM: double-chirped mirror.

Figure 6-2 shows the schematic setup of the laser source, consisting of four parts: 1) an Yb-doped fiber oscillator mode-locked by nonlinear polarization evolution, 2) a diffraction-

grating pair to compress the output pulses, 3) a short piece of photonic crystal fiber (PCF) for FOCR generation, and 4) several double-chirped mirrors (DCMs) to compress the resulting pulses at 850 nm. The Yb-doped fiber oscillator (29-MHz repetition-rate and 226-mW average power) operates in the stretched-pulse mode-locking regime with the output spectrum centered at 1030 nm. The output pulses pass through an optical isolator (Thorlabs IO-3D-1030-VLP) with 90% transmission efficiency and are then compressed by a diffraction-grating (600 line/mm) pair, GD2. The average power of the compressed pulse is 140 mW for a grating-pair efficiency of 70%. As Fig. 6-3 shows, the measured autocorrelation (AC) duration of the compressed output pulse (black line) is 94 fs; the inset shows the corresponding optical spectrum centered at 1030nm with 43-nm bandwidth. As a comparison, the autocorrelation trace of the transform-limited pulse calculated from the optical spectrum is plotted as the red dotted line in Fig. 6-3 as well, showing a duration of 76 fs.

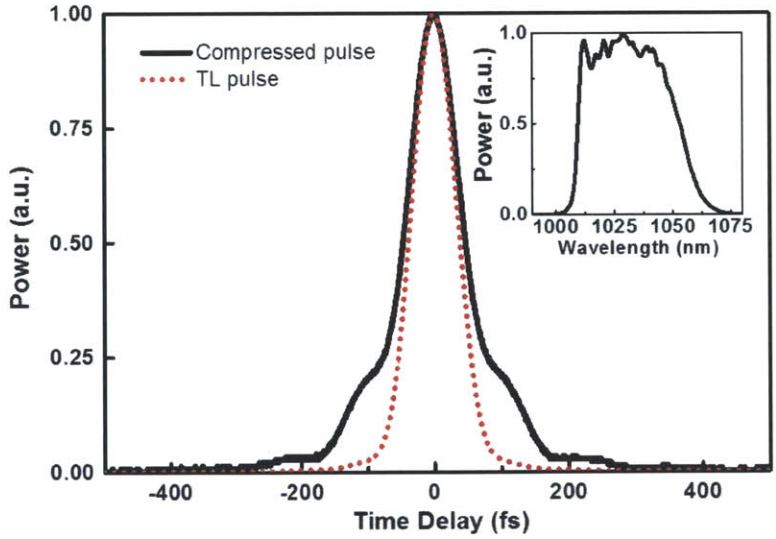

Fig. 6-3. The measured AC trace of the Yb-fiber oscillator output pulse (black line) and the calculated AC trace of the transform-limited pulse (red dotted line) corresponding to the optical spectrum shown as inset.

Compressed pulses of 84 mW (pulse energy of 2.9 nJ) were coupled into a piece of PCF, which has a core of 3.2 μm in diameter with its zero-dispersion wavelength (ZDW) at 945 nm.

A half-wave plate (HW3) was placed before the PCF to mitigate the detrimental effect caused by the fiber's residual birefringence. As the coupled ultrashort pulses propagate in the PCF, they emit dispersive waves at shorter wavelength due to high-order fiber dispersion.

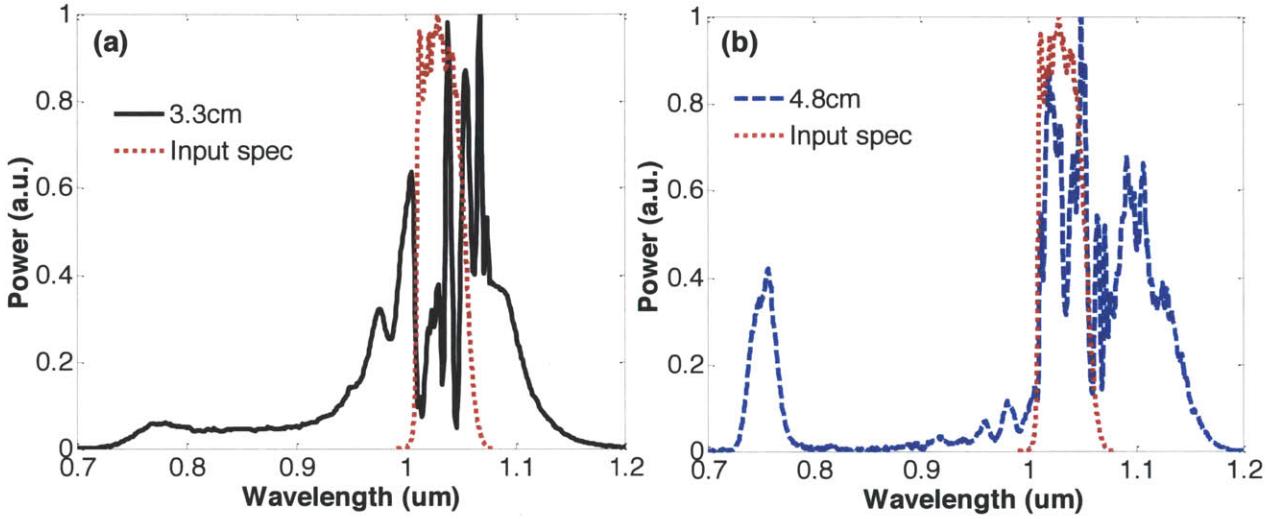

Fig. 6-4. The output spectrum of (a) the 3.7cm-long PCF (black solid curve) and (b) the 4.8cm-long PCF (blue dashed curve).

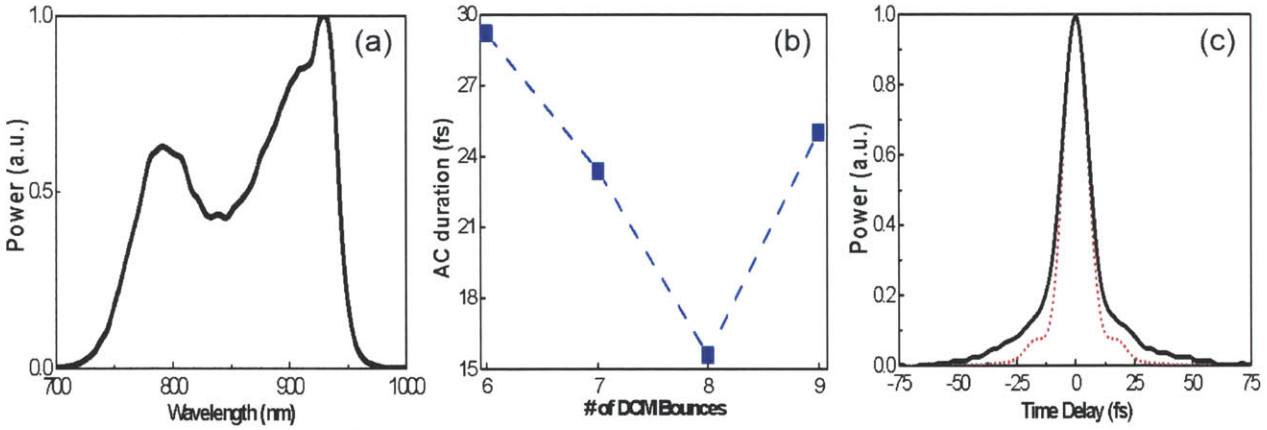

Fig. 6-5. (a) Filtered optical spectrum. (b) AC duration vs. number of DCM bounces (blue dashed line). (c) The measured AC trace of the compressed FOCR (black line) pulse and the calculated AC trace (red dotted line) of the transform-limited pulse corresponding to the (a) filtered optical spectrum.

Figure 6-4 presents the output spectra for two PCFs at different length. Due to a broader FOCR phase-matching bandwidth, the spectrum in Fig. 6-4(a) produced from 3.7-cm PCF develops a smooth broadband continuum extending down to ~750 nm well into the Ti:sapphire

wavelength range. As we increase the PCF length to 4.8 cm, the phase-matching bandwidth decreases substantially; phase-matching can be only fulfilled in a narrow wavelength range around 750 nm, producing an isolated and narrowband FOCR spectrum (Fig. 6-4(b)).

Since the FOCR is initiated by nonlinearity interacting with higher-order dispersion, the compressibility of the FOCR continuum remains in question. To answer this question, we use a 950-nm short-pass filter to slice out the FOCR continuum from the output spectrum shown in Fig. 6-4(a). The filtered continuum, shown in Fig. 6-5(a), has >170-nm full width at half maximum (FWHM) with an average power 7.5 mW, corresponding to 9% conversion efficiency. Such a broad spectrum supports 8.5-fs transform-limited pulses. We then compensated for the spectral phase using double-chirped mirrors (DCM). Each mirror comprises 80 alternating layers of TiO_2 and SiO_2. Each bounce provides a group-delay dispersion of -56 fs^2. The corresponding pulses were measured by an autocorrelator. Figure 6-5(b) shows the autocorrelation duration versus the number of DCM bounces. The compressed pulses reach the shortest duration after 8 bounces. Figure 6-5(c) shows the measured shortest autocorrelation trace (black line); it has a duration (FWHM) of 15 fs. Also shown in this figure (red dotted curve) is the calculated autocorrelation trace (red dotted line) of the transform-limited pulse corresponding to the filtered FOCR spectrum; the autocorrelation duration is 12 fs. We estimated that the compressed pulses using 8 DCM bounces have a duration of ~11 fs assuming a deconvolution factor of 1.4.

In summary, in the proof-of-principle experiment we demonstrate that a combination of an 30 MHz Yb-doped fiber oscillator and FOCR provides new capabilities to ultrafast laser technology: 1) generation of pulses ~11 fs with smooth spectrum and 2) broadband wavelength coverage overlapped with Ti:sapphire lasers. To scale up the average power, in the next section we derive our FOCR ultrafast source from a 3-GHz Yb-fiber laser system, and demonstrate

a 3-GHz source at the Ti:sapphire laser wavelength with up to 380-mW average power and >200 nm bandwidth (FWHM).

6.4. Experiment with the 3-GHz Yb-Fiber Laser System

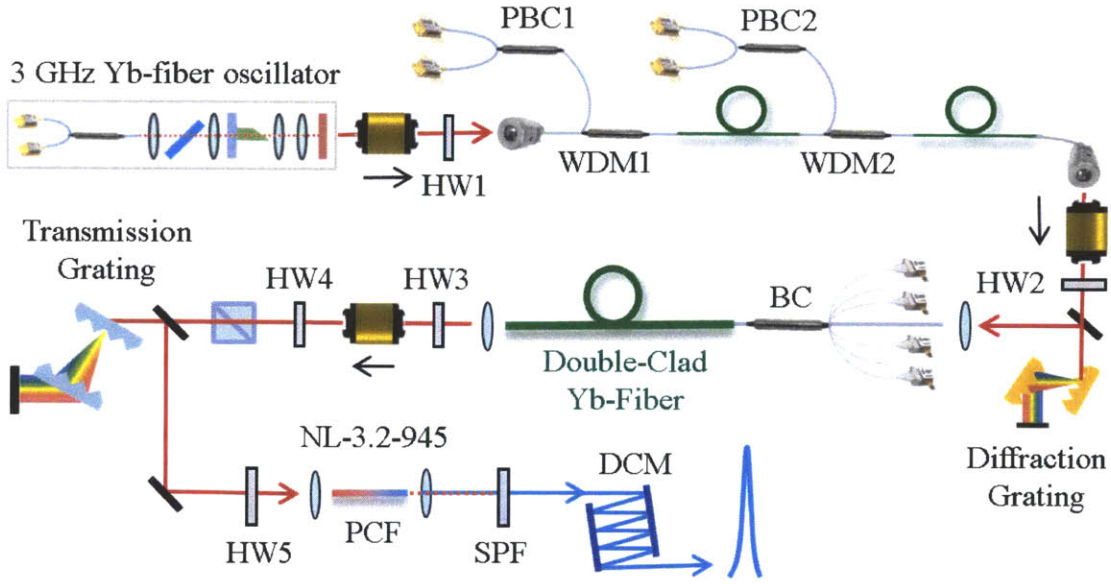

Fig. 6-6. Schematic setup of the 3-GHz ultrafast FOCR source. HW: half-wave plate; PBC: polarization beam combiner; BC: (6+1) x 1 beam combiner; SPF: short-wavelength-pass optical filter that only transmits wavelength components below 950 nm; and DCM: double-chirped mirror.

To further scale up the FOCR power, we replace the 29 MHz Yb-doped fiber oscillator with our 3 GHz Yb-fiber laser system. Figure 6-6 shows the schematic setup of the 3-GHz FOCR laser source, mainly consisting of: 1) a 3-GHz fundamentally mode-locked Yb-fiber oscillator [21], 2) a two-stage polarization-maintaining (PM) fiber amplifier to pre-amplify the oscillator pulses, 3) a diffraction-grating pair for pre-chirp management prior to further power amplification [22], 4) a double-clad Yb-fiber power amplifier, 5) a transmission-grating pair to compress the amplified pulses, 6) a short piece of PCF for wavelength conversion via FOCR, and 7) several double-chirped mirrors (DCMs) to compress the resulting pulses at 850 nm.

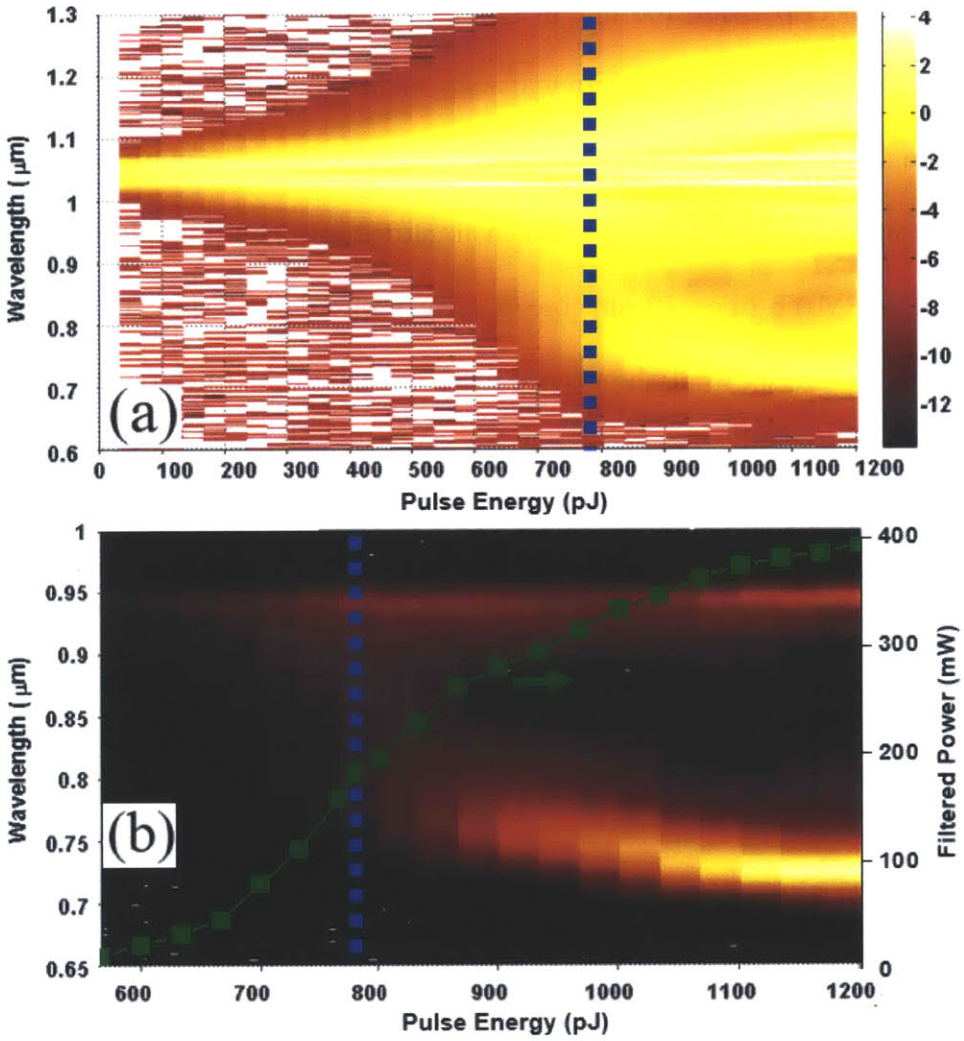

Fig. 6-7. (a) Measured output spectra versus coupled pulse energy into 3.7-cm PCF NL-3.2-945. Spectral intensity is shown on a logarithm scale. (b) Measured output spectra after a short-wavelength-pass optical filter that blocks spectral components above 950 nm. Spectral intensity is shown on a linear scale. The green curve in (b) shows the measured average power after the short-wavelength-pass optical filter. Blue dashed lines in both figures mark the 780 pJ pulse energy corresponding to the broadband FOCR.

Each key element of the 3 GHz Yb-fiber laser system has been discussed in the previous chapters. The 3-GHz Yb-fiber oscillator, centered at 1027 nm with 3.5 nm bandwidth (blue line in Fig. 5-2), produces 32 mW average power. The design and implementation of such a 3 GHz Yb-fiber oscillator has been described in Chapter 2 [21]. The output pulses are amplified to 1.05 W by a two-stage pre-amplifier constructed from single-mode PM fibers; the resulting optical

spectrum is broadened to 7 nm (red line in Fig. 5-2). Before the pre-amplified pulses enter the power amplifier, we employ the pre-chirp management method demonstrated in Chapter 3 [22] to achieve high-quality compressed pulses after the power amplifier. The pulses are pre-chirped by a diffraction-grating (600 line/mm) pair, and then amplified by a power amplifier constructed from 2.4-m double-clad PM Yb-fiber (10-μm core diameter) spliced to a PM (6+1) x 1 beam combiner. The amplified pulses are spectrally broadened to 30-nm bandwidth (green line in Fig. 5-2) during the amplification and are then compressed by a transmission-grating (1000 line/mm) pair. By properly pre-chirping the pre-amplified pulses, we achieve compressed pulses with 13-W average power and the measured autocorrelation trace is 140 fs in duration shown as the solid curve in the inset of Fig. 5-2. As a comparison, the autocorrelation trace of the transform-limited pulse calculated from the optical spectrum is plotted as the dotted curve, showing an autocorrelation duration of 95 fs.

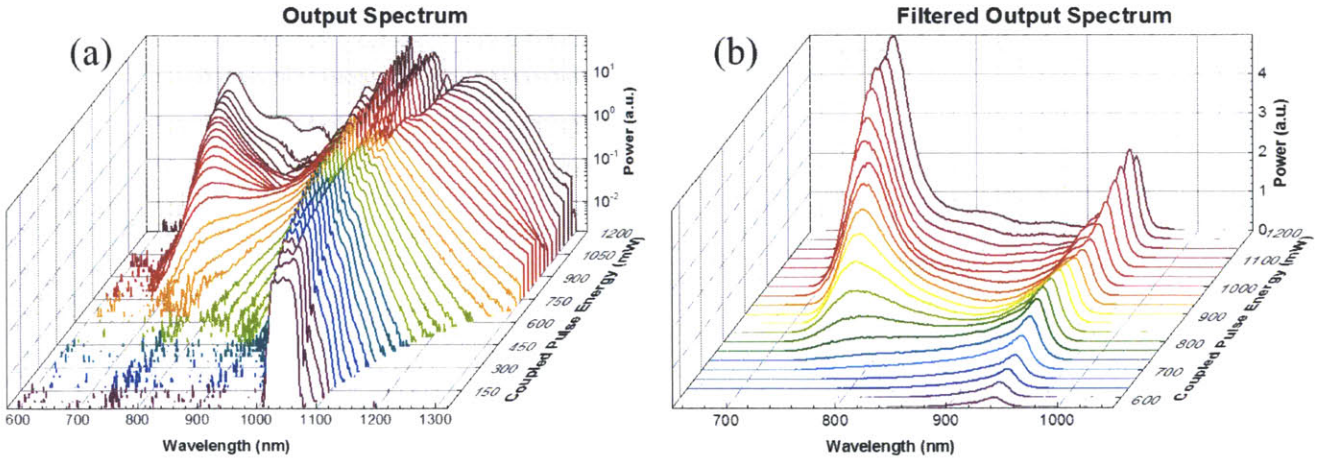

Fig. 6-8. (a) Measured output spectra versus coupled pulse energy into 3.7-cm PCF NL-3.2-945. Spectral power is shown on a logarithm scale. (b) Measured output spectra after a short-wavelength-pass optical filter that blocks spectral components above 950 nm. Spectral power is shown on a linear scale.

To compare with the simulation results in Fig. 6-1(a), we couple the compressed pulses into 37-mm PCF NL-3.2-945. A half-wave plate (HW5 in Fig. 6-6) placed before the PCF mitigates

the detrimental effect caused by the fiber's residual birefringence. Figure 6-7(a) records the measured spectra from the PCF output as a function of coupled pulse energy. In order to visualize the spectral evolution more clearly, the waterfall plots of Fig. 6-7 are also shown in Fig. 6-8 for reference. A comparison between Fig. 6-7(a) and Fig. 6-1(a) indicates excellent agreement between simulation results and experimental measurements. As the simulation predicts, a broadband FOCR appears at the pulse energy of 780 pJ (marked by the dashed lines in Fig. 6-7), corresponding to 2.34-W coupled average power. To clearly observe the evolution of FOCR spectra, we use a short-wavelength-pass optical filter to filter out the spectral components below 950 nm, and plot them in Fig. 6-7(b), shown on a linear scale. It clearly shows that a spectral gap starts to form around 850 nm as pulse energy increases beyond 780 pJ, and an isolated FOCR spectrum appears with its center wavelength blue shifted with the increased pulse energy. The green curve marked with squares in Fig. 6-7(b) denotes the average power of the filtered spectrum, which increases monotonically for higher pulse energy. At 780-pJ pulse energy, 184-mW average power (i.e., 61-pJ pulse energy) is achieved.

It is noteworthy that the optimum pulse energy corresponding to the broadband, non-isolated FOCR depends on the PCF length: shorter PCF requires more input pulse energy. In addition to the 37-mm PCF, we have investigated another two fiber lengths and found that the required input pulse energy to achieve a broadband FOCR is about 440 pJ for 48-mm PCF and 1430 pJ for 28-mm PCF. Figure 6-9(a) plots the three broadband FOCR spectra after the short-pass optical filter. Normalized to their peak at 940 nm, the three spectra are of similar spectral shape centered at around 850 nm with >200-nm bandwidth (FWHM). The average powers of the filtered spectra are 94 mW, 184 mW, and 380 mW, respectively.

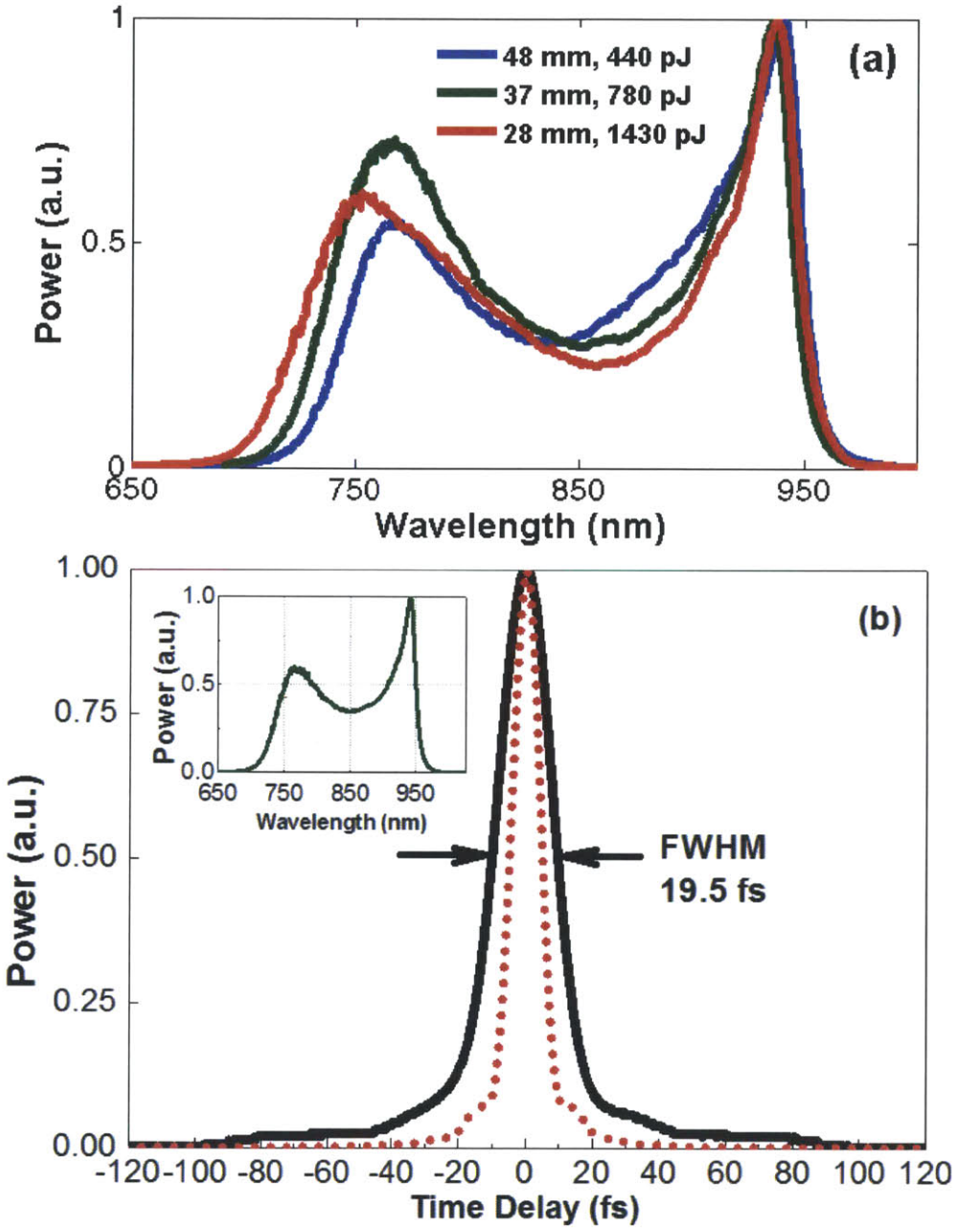

Fig. 6-9. (a) Filtered spectra of broadband FOCR at three different fiber length: 28 mm (red line), 37 mm (green line), and 48 mm (blue line). These three spectra are generated at different input pulse energies: 1430 pJ (28-mm PCF), 780 pJ (37-mm PCF), and 440 pJ (48-mm PCF). The spectra are all normalized to their spectral peak at 940 nm. (b) Blue solid line: measured autocorrelation trace of the compressed FOCR pulse using DCMs to compensate for the phase from the FOCR spectrum (i.e., green curve in (a)) generated from the 37-mm PCF with 780-pJ input pulse energy. Red dashed line: calculated autocorrelation trace of the transform-limited pulse given by the FOCR spectrum in the inset.

Again, since the FOCR is initiated by nonlinearity interacting with the higher-order dispersion, compressibility of such a broadband (>200 nm) FOCR spectrum remains in question. Since nearly the entire filtered spectrum falls into the PCF's normal dispersion region, we use home-designed double-chirped mirrors (DCM) with negative group-delay dispersion to compensate for the spectral phase of the spectra in Fig. 6-9(a). The mirror comprises 96 alternating layers of TiO_2 and SiO_2; each bounce provides a group-delay dispersion of -70 fs^2. The black solid curve in Fig. 6-9(b) shows the measured shortest autocorrelation trace for the filtered FOCR spectrum achieved from 37-mm PCF and 780-pJ pulse energy. The autocorrelation trace after 8 DCMs has a duration (FWHM) of 19.5 fs. Also shown in the same figure is the calculated autocorrelation trace (red dotted line) of the transform-limited pulse given by the corresponding FOCR spectrum (i.e., black curve in Fig. 6-9(a)). We estimate that the compressed pulses are ~14 fs in duration assuming a deconvolution factor of 1.4. We attribute the deviation from the 8-fs transform-limited duration to the uncompensated higher-order dispersion. Note that applying FOCR to Er-doped fiber lasers for broadband wavelength conversion followed by subsequent pulse compression has led to generation of 8-fs pulses centered at 1.17 μm [111].

6.5. Summary

We demonstrate that a combination of a high power 3-GHz Yb-fiber laser system and FOCR provides new capabilities to ultrafast laser technology: 1) generation of ~14 fs pulses with smooth spectrum and 2) broadband wavelength coverage overlapped with Ti:sapphire lasers. Despite relatively low pulse energy of ~100 pJ, such a multi-GHz few-cycle source at Ti:sapphire laser wavelength is of particular importance for applications in optical frequency metrology (e.g., astrophysical spectrograph calibration [28] and multi-photon coherent microscopy [1]). Since the compressed FOCR pulse is derived from the Yb-doped fiber oscillator, and thus

synchronized with the 1.03-μm oscillator output pulse, it is well suited for seeding an optical parametric amplifier with the pump derived from the same fiber oscillator as well. More specifically, we can split the fiber oscillator output into two copies—one for 850-nm pulse generation as the seed and the other after frequency doubling to serve as the pump. The excellent power scalability of Yb-fiber laser technology makes such an ultrafast laser system truly appealing for applications in high-field and attosecond science.

Chapter 7

Application II: 3 GHz, Watt-Level Femtosecond Raman Soliton Source

7.1. Motivation

Femtosecond laser pulses with multi-GHz repetition-rate are desired in many applications, including optical arbitrary waveform generation, laser frequency combs for astrophysical spectrograph calibration, high-speed photonic analog-to-digital conversion, nonlinear bio-optical imaging, to name a few. To date, all the demonstrated multi-GHz femtosecond lasers operate at three wavelengths: 0.8 μm (e.g., Ti:sapphire laser [112,113]), 1.03 μm (e.g., lasers with gain materials of Yb-fiber [21], Yb-KYW [73], Yb-KGW [37], Yb:glass [75] etc.), and 1.55 μm (e.g., Er/Yb co-doped fiber laser [38]). Some important applications, however, require such high repetition-rate femtosecond pulses in a wavelength regime that cannot be directly covered by available ultrafast lasers. For example, most live biological specimens exhibit a minimum light attenuation in the range of 1.2-1.35 μm [114]. Using femtosecond pulses of this wavelength range for nonlinear bio-optical imaging (e.g., two-photon fluorescence excitation microscopy, second-harmonic generation microscopy etc.) allows deeper penetration through turbid specimens. To avoid photo-induced damage caused by pulse energy rather than average power, increasing pulse repetition-rate to multi-GHz while keeping the pulse energy relatively low will improve the

signal-to-noise ratio, reduce the data acquisition time, and increase the image frame rate [2]. Another application is photonic analog-to-digital conversion (ADC) to overcome an aperture jitter of conventional ADCs by using low timing jitter of mode-locked femtosecond lasers [13]. Multi-GHz mode-locked lasers can support high sampling rate and the wavelength range of 1.2-1.3 μm is compatible with mature SiGe technology, allowing a photonic ADC in a monolithic electronic-photonic integration platform.

In this chapter, we present a 3-GHz femtosecond Raman soliton source tunable between 1.15-1.35 μm, producing ultrashort pulses with up to 0.9 W average power at 1.35 μm. Such a Raman soliton source exhibits both the highest repetition rate and highest average power to the best of our knowledge.

7.2. 3 GHz Raman Soliton Femtosecond Source Generation

7.2.1 Experimental Setup

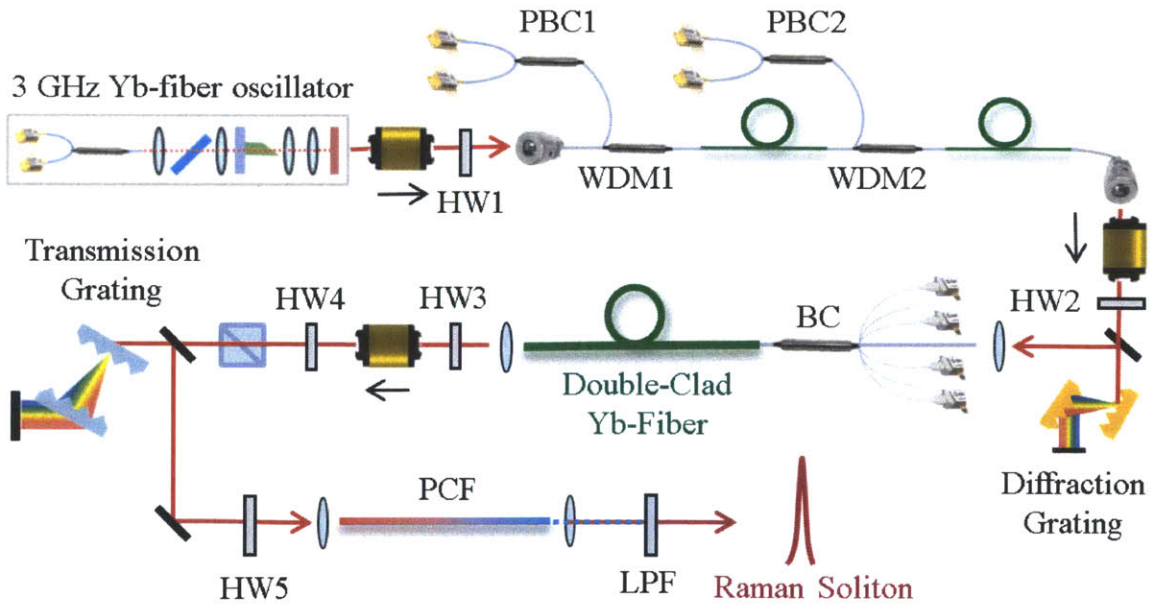

Fig. 7-1 Schematic experimental setup of the 3 GHz Raman soliton source. HW: half-wave plate; PBC: polarization beam combiner; BC: (6+1)x1 beam combiner; LPF: long -pass optical filter; and DCM: double-chirped mirror.

Figure 7-1 shows the experimental setup consisting of a 3-GHz Yb-fiber oscillator, a three-stage Yb-fiber amplifier chain, two diffraction-grating pairs to manage the pulse chirp for high-quality pulse amplification and compression, and a piece of photonic crystal fiber (PCF) for Raman soliton generation. A detailed description of this high-power Yb-fiber master-oscillator-power-amplifier system can be found in Chapter 5.

7.2.2 Simulation of Raman soliton in Three Different PCFs

Table 7-1. Parameters of PCFs used in simulations.
(MFD: mode field diameter, ZDW: zero-dispersion wavelength, γ: nonlinear parameter, β_2: group-velocity dispersion, and β_3: third-order dispersion.)

PCF (type)	MFD (μm)	ZDW (μm)	γ (W^{-1}/km)	β_2 ps^2/km	β_3 (ps^3/km)
NL-3.2-945	2.8	0.945	23	-14.0	0.057
NL-3.7-975	3.1	0.975	18	-7.40	0.059
NL-5.0-1040	4.0	1.040	11	-0.42	0.063

Raman soliton self-frequency shift arises from the interplay between intra-pulse stimulated Raman scattering and soliton formation in an optical fiber with negative group velocity dispersion (GVD) [60]. As a result, the Raman soliton's center frequency red shifts continuously during the propagation while maintaining its transform-limited hyperbolic secant profile. The resulting Raman soliton source delivers wavelength tunable femtosecond pulses at the desired wavelength that cannot be directly obtained from mode-locked ultrafast lasers [115–119]. The amount of self-frequency shift depends on many parameters, such as fiber nonlinearity and GVD, input pulse duration and energy, and fiber length. Semi-analytical methods have been developed to qualitatively describe the complicated interaction among these parameters [120–122]. However, an accurate modeling of Raman soliton evolution necessitates numerically solving the generalized nonlinear Schrödinger equation (GNLSE) that takes into account nonlinear effects including

self-phase modulation, self-steepening, and Raman scattering [60]. To be consistent with the following experimental results, we solved the GNLSE to simulate an optical pulse centered at 1.042 μm propagating inside three different photonic crystal fibers (PCFs)—NL-3.2-945, NL-3.7-975, and NL-5.0-1040—all commercially available from NKT Photonics. Table 7-1 lists the parameters for these three PCFs.

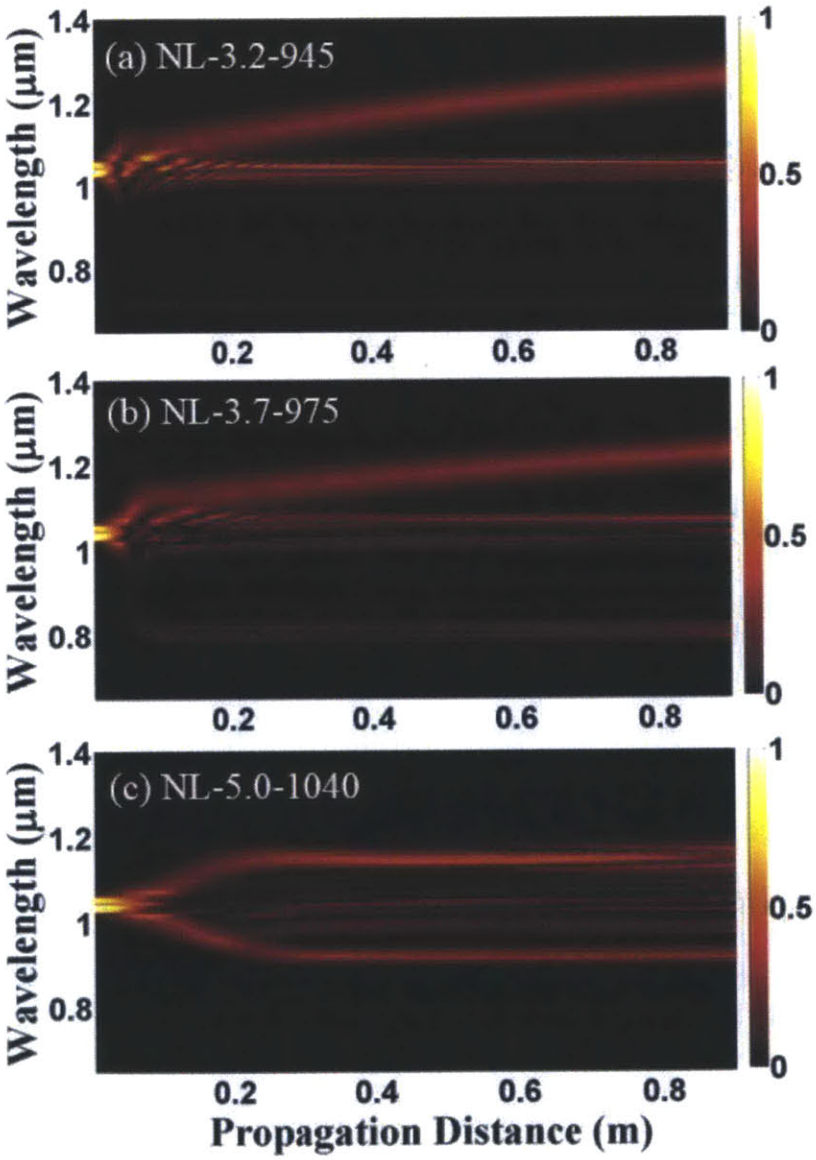

Fig. 7-2. Simulation of spectral evolution using GNLSE for three PCFs: (a) NL-3.2-945, (b) NL-3.7-975, and (c) NL-5.0-1040. The input pulse is of Gaussian shape with 110-fs FWHM duration and 333-pJ pulse energy, which corresponds to 1-W average power for a pulse train at 3 GHz repetition rate.

Figure 7-2 shows the spectral evolution along the fiber length for an input Gaussian pulse with 110 fs full-width-half-maximum (FWHM) and 333 pJ energy. Clearly PCF NL-3.2-945 (Fig. 7-2(a)) and NL-3.7-975 (Fig. 7-2(b)) enable Raman soliton formation that shifts towards longer wavelength with increased propagation distance. For the same propagation distance, the Raman soliton in PCF NL-3.2-945 exhibits longer center wavelength than its counterpart in NL-3.7-975. After propagating 90 cm in PCF NL-3.2-945 (NL-3.7-975), the Raman soliton pulse centers at 1.3 μm (1.2 μm). It is noteworthy that both fibers generate phase-matched dispersive waves at the shorter wavelength, with center wavelength at 0.7-μm for PCF NL-3.2-945 and 0.8-μm for PCF NL-3.7-975. For PCF NL-5.0-1040, its zero-dispersion wavelength (1.040 μm) is so close to the input pulse's center wavelength (1.042 μm) that half of the spectrum locates in the normal dispersion regime (i.e., positive GVD) and the other half in the anomalous dispersion regime (negative GVD). Together with the weaker nonlinearity (11 W^{-1}/km), PCF NL-5.0-1040 shows minimal Raman-induced frequency shift.

7.2.3 Experimental Results

Guided by above simulation, we launched 1-W of compressed pulses generated from our 3-GHz Yb-fiber master-oscillator-power-amplifier system into 90 cm of these three PCFs, and recorded the output spectra in Fig 7-3. As predicted by the simulation, PCF NL-3.2-945 and NL-3.7-975 produce Raman soliton pulses centering at 1.3 μm and 1.2 μm, respectively. We chose PCF NL-3.2-945 for a more detailed study since it generates a Raman soliton pulse with the largest wavelength red-shift. Figure 7-3 records the output spectra from 87-cm PCF NL-3.2-945 for different input average powers. As the power increases, the Raman soliton peak wavelength (λ_{peak}) is further red-shifted and a second Raman soliton starts to emerge. With 1.31-W input power, the 1st Raman soliton peaks at 1.35 μm with 30-nm (FWHM) spectral width. We filtered out this

Raman soliton spectrum and measured the autocorrelation trace (inset of Fig. 7-4), which is 210 fs (FWHM) in duration; it corresponds to a hyperbolic secant pulse of 136-fs with a de-convolution factor 1.54.

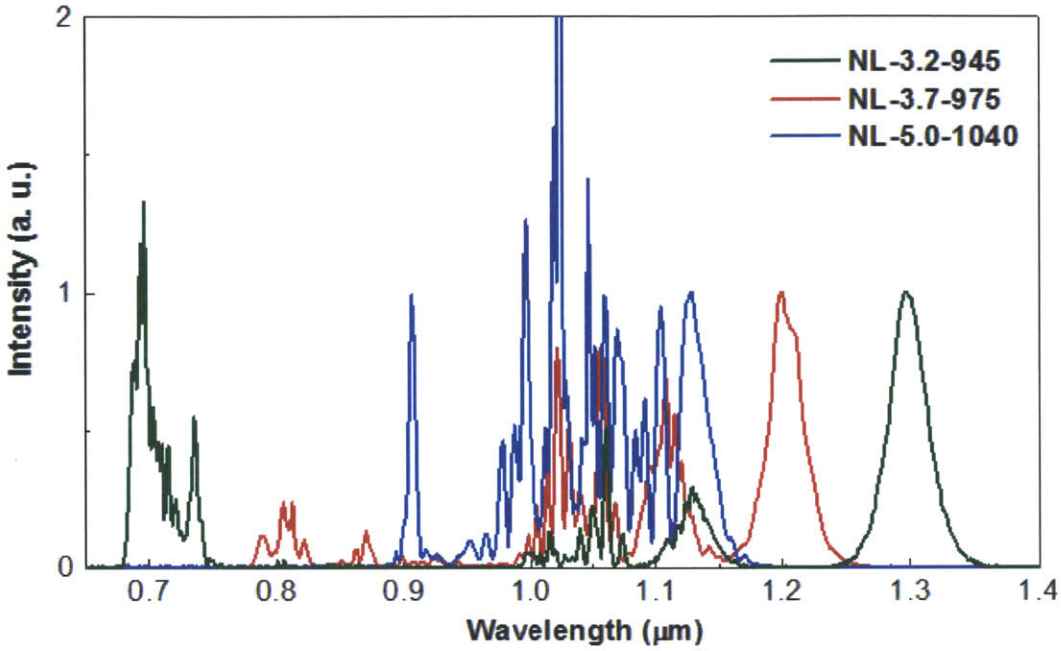

Fig. 7-3. Output spectra from three different PCFs: NL-3.2-945 (green), NL-3.7-975 (Red), and NL-5.0-1040 (blue). All fibers are 90 cm long and the average power coupled into the fibers is 1-W. The spectra are normalized to the Raman soliton peak.

We also measured the peak wavelength (λ_{peak}) and average power of the 1st Raman soliton generated from PCF NL-3.2-945 at three lengths: 87 cm, 54 cm, and 30 cm (Fig. 7-5). As Fig. 7-5(a) shows, when shorter PCFs are used to generate Raman solitons at the same wavelength higher input power is required. For example, the power requirement to produce a Raman soliton pulse at 1.35 μm is 1.31 W, 1.91 W, and 4.90 W for PCF length of 87 cm, 54 cm, and 30 cm, respectively. Figure 7-5(b) plots the average power of the 1st Raman soliton as a function of its peak wavelength for the three PCF lengths. As expected, the average power increases monotonically with respect to the peak wavelength. At the same peak wavelength, using shorter

PCF leads to stronger Raman soliton pulse; especially, the Raman soliton pulse peaking at 1.35 μm from 30-cm PCF NL-3.2-945 has an average power of 900 mW.

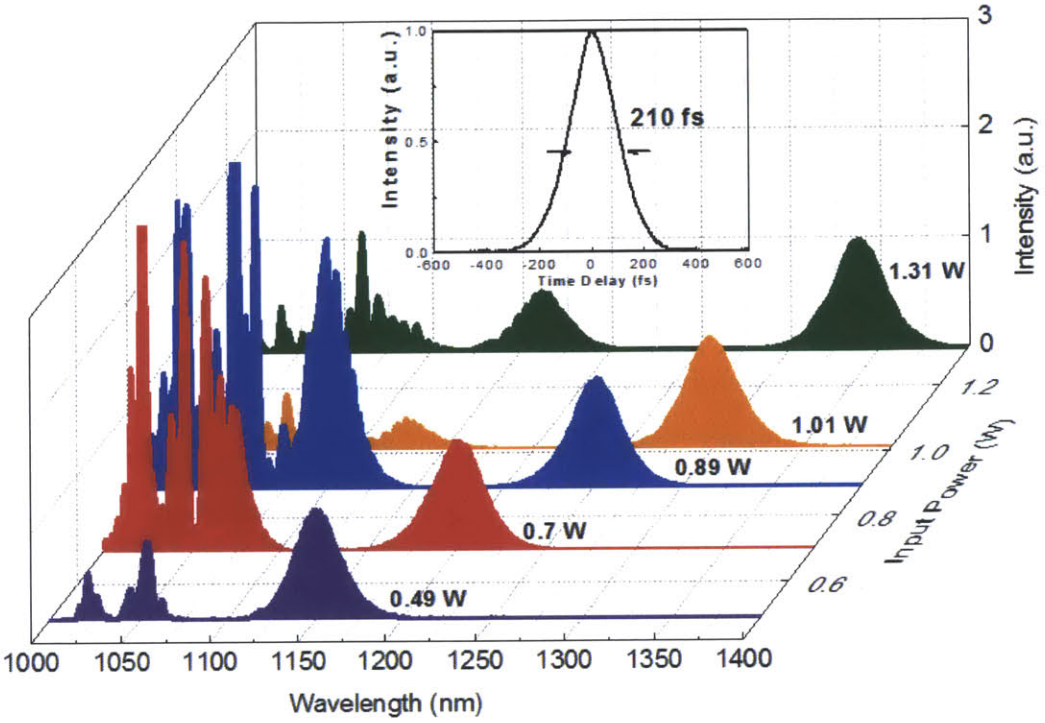

Fig. 7-4. Raman soliton generation as a function of input power for 87-cm PCF NL-3.2-945. The average power coupled into the PCF is also shown for each spectrum. Inset: autocorrelation trace of the Raman soliton pulse at 1.35 μm. The spectra are normalized to the peak of the first Raman soliton spectrum.

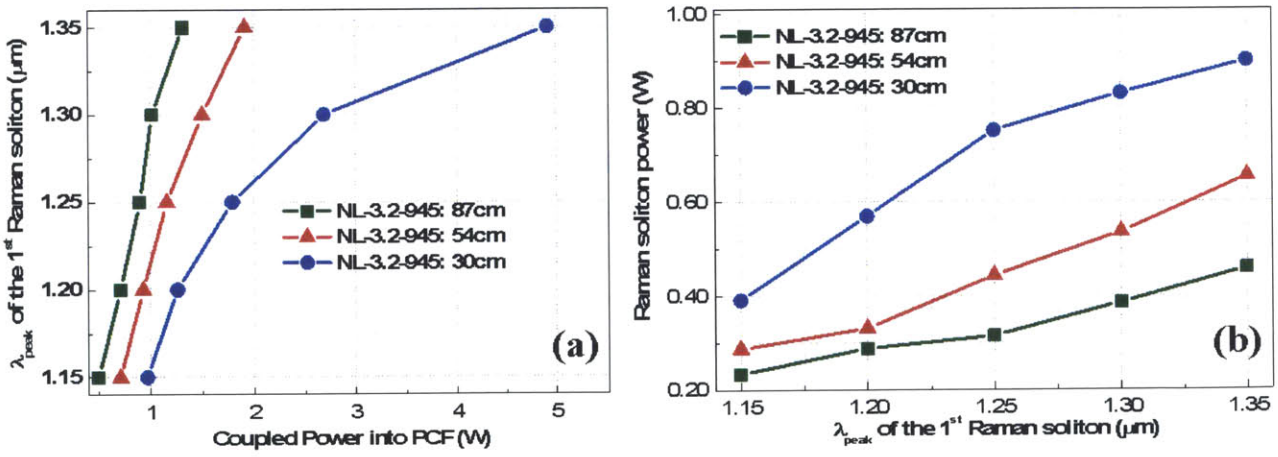

Fig. 7-5. (a) Peak wavelength of the first Raman soliton as a function of input power for PCF NL-3.2-945 at three different lengths. (b) Average power of the first Raman soliton as a function of the first Raman soliton peak wavelength for PCF NL-3.2-945 at three different lengths.

7.2.4 Relative Intensity Noise of Different Order Raman Solitons

The intensity noise of our Raman soliton source is evaluated by measuring the relative intensity noise (RIN). We measured the RIN of the pulse train directly from the 3 GHz Yb-fiber oscillator, after the power amplifier, and after Raman shifting to 1.35 μm in a 54-cm PCF. As Fig. 7-6 shows, the Raman shifting in the PCF increases the intensity noise. The dramatic increase of low-frequency noise (<10-kHz) is attributed to PCF input-end vibration and thermally caused instability due to the high average power coupled into the PCF. Nonetheless, the total integrated RIN is as low as 0.33% from 100 Hz to 10 MHz.

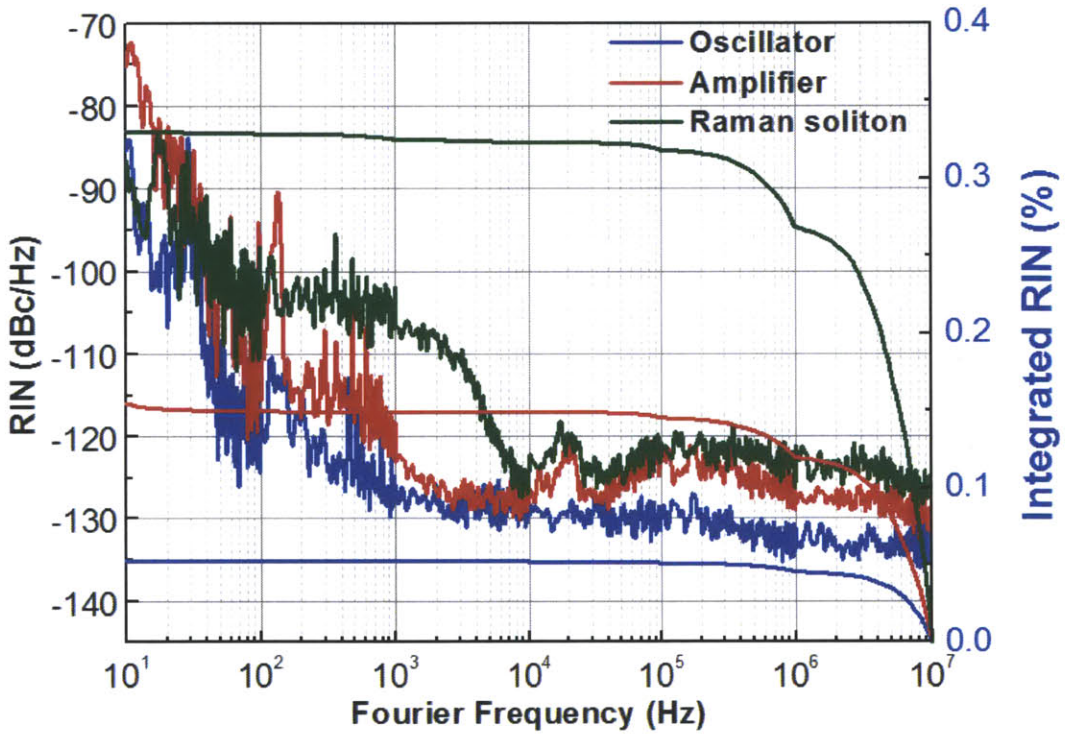

Fig. 7-6. RIN and integrated RIN for the 3 GHz Yb-fiber oscillator, power amplifier, and the Raman soliton, respectively. The Raman soliton pulse peaks at 1.35 μm generated by the 54-cm PCF NL-3.2-945.

7.3. Summary

We demonstrate a 3-GHz repetition-rate (wavelength tunable between 1.15-1.35 μm) source using Raman Soliton generation in a PCF with, to the best of our knowledge, the highest average

power of 0.9 W at 1.35 μm. The delay nature of the Raman scattering effect transfers the input pulse energy to a longer wavelength with >35% efficiency within the wavelength tuning range of the PCF. Further wavelength shifts or power scaling are possible using different PCFs, such as topographic PCFs or large mode area PCFs [123,124]. This high power 3 GHz wavelength tunable laser source will find interesting applications in high-speed photonic analog-to-digital conversion, nonlinear bio-optical imaging, and mid-IR source generation, to name a few.

Chapter 8

3 GHz Passive Frequency Comb via Difference Frequency Generation

8.1. Motivation

The ultimate goal of this thesis work is to build a 3-GHz fiber laser frequency comb that will enable the implementation of next-generation astro-combs based on multi-GHz Yb-fiber laser technology. Since we have validated the feasibility of building a frequency comb based on a narrow bandwidth oscillator using the pre-chirp management method in Chapter 4, we first perform an experiment similar to the one shown in Fig. 4-5 to detect and stabilize the f_{CEO} beat note. The compressed pulses from the 3-GHz laser system are coupled into the same 60-cm long PCF with ZDW at 945 nm. The generated SC spectrum as shown in Fig. 8-1 spanning from 660 nm to 1400 nm is launched into a 1f-2f interferometer which includes the same PPLN for second harmonic generation (SHG) of the 1360 nm wavelength range. The red dotted vertical lines indicate the two wavelengths, 680nm and 1360nm, for the 1f-2f interferometer. However, after compensating the group delay mismatch between the fundamental frequency and the SHG frequency by a tunable delay path, the detected signal has a substantially enhanced white-noise background such that the heterodyned f_{CEO} beat-note becomes undetectable, which indicates a SC of low coherence. This problem does not appear when building the 280 MHz frequency comb.

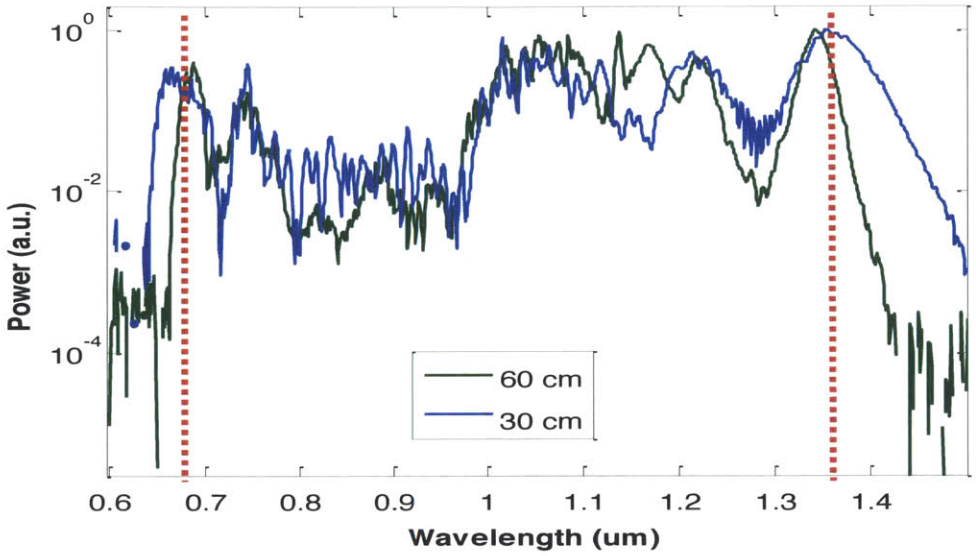

Fig. 8-1. The supercontinuum spectra from the 60-cm and the 30-cm PCFs NL-3.2-945. The red dotted vertical lines indicate the wavelengths for 1f-2f interferometer.

To achieve higher SC coherence, we need a shorter PCF, a shorter pulse, or lower intensity noise of the pulse in order to reduce the overall noise amplification by modulation instability and therefore increase the SC coherence [80,83,125–131]. A straightforward way to solve this is to replace the PCF with a shorter PCF because a longer the PCF leads to SC with worse coherence [83,125,126]. We then reduce the length of the PCF from 60 cm to 30 cm in the experiment. Figure 8-1 also shows the generated SC from the 30-cm PCF. Furthermore, the repetition rate of the 3 GHz Yb-fiber oscillator is locked to a RF reference (as introduced in Chapter 5) in order to greatly reduce the low-frequency timing jitter. Although this is not required in the 280 MHz f_{ceo} locking, we believe the improved timing jitter shown in Fig. 5-6 will significantly enhance the SC coherence because the timing jitter of the input pulse will be amplified and also be converted to the RIN and phase noise of the SC at the PCF output. Nonetheless, the heterodyned f_{CEO} beat-note remains undetectable. Therefore, we need to come up

with a different method in detecting f_{CEO} in order to improve the coherence and eventually build a 3-GHz frequency comb.

In this chapter, a passively phase-locked laser source based on the 3-GHz Yb-fiber laser system is introduced. The carrier envelope offset frequency is set to zero via difference frequency generation between the dispersive wave at 613 nm generated from PCF NL-3.0-850 and the compressed pulse centered at 1045 nm. A frequency comb with such a high repetition-rate has not been demonstrated in the Er-doped fiber laser wavelength.

8.2. Investigation of Supercontinuum Coherence

As mentioned in Section 5.3.1, in the 3-GHz laser system the high power double-clad Yb-fiber amplifier is pumped by four multimode pump diodes, which have much higher RIN than single mode diodes. We compare the measured integrated RIN from 10 Hz to 10 MHz of the 280 MHz system (which employs only single-mode pump diodes) and the 3 GHz system. The integrated RIN of the 280 MHz system is ~0.1% while that of the optimized 3 GHz system is <0.2 %; the 3-GHz oscillator itself has a RIN of ~0.1%. Because of the necessity of using multimode diodes in the high power 3-GHz laser system, further reducing the intensity noise of this laser system becomes extremely challenging. Therefore, we resort to a different way to generate the f_{CEO} beat note. In the previous section, the finding of the f_{CEO} beat note is done by beating the SHG of 1360 nm Raman soliton with the 680 nm dispersive wave. Raman soliton is actually noisy due to the spontaneous Raman scattering and the modulation instability [132,133]. Also, when the PCF is long, the Raman soliton will trap the dispersive wave and the noisy Raman soliton will thereby affect the dispersive wave; the dispersive wave will become noisy as well.

To investigate how the intensity noise affects the resulting SC coherence, we calculate the coherence of a noisy pulse at a PCF output. The noise of a pulse could be from the quantum shot

noise and the technical noise in the experiment environment. Normally in the literature, only quantum shot noise is taken into account to calculate the SC coherence. The quantum shot noise is usually modelled semi-classically by adding one photon with random phase to each frequency bin; the intensity noise (laser technical noise) is modelled by adding a random intensity within a specified percentage of the overall intensity in each time bin. In our simulation, we only consider the technical intensity noise because the quantum shot noise is orders of magnitude less; it is the technical noise that results in the deteriorated SC coherence such that the f_{CEO} beat signal becomes undetectable or buried in the noise. In the simulation, 30 single-shot calculations are performed. The resulting coherence is defined as the modulus of the complex degree of first-order coherence calculated over a finite bandwidth at each wavelength in the SC: $\left|g_{12}^{(1)}(\lambda,t_1-t_2)\right| = \left|\frac{< E_1^*(\lambda,t_1)E_2(\lambda,t_2) >}{\sqrt{<|E_1(\lambda,t_1)|^2><|E_2(\lambda,t_2)|^2>}}\right|$. The angle brackets indicate an ensemble average over independently generated SC pairs, $E_1(t_1, \lambda_1)$ and $E_2(t_2, \lambda_2)$. We apply the ensemble average to the simulation results that yields 435 SC pairs obtained from input pulses with different values of integrated relative intensity noise. Because we are interested mainly in the wavelength dependence of the coherence, we calculate $\left|g_{12}^{(1)}\right|$ at t_1-t_2=0, which, in practice, corresponds to measuring the fringe visibility at the center of the fringe pattern in a Young two-source experiment [80,83,125–131].

Figure 8-2(a) shows the simulated coherence of a 0.7-nJ pulse propagating in a 60-cm long PCF with ZDW at 945 nm with four different levels of added intensity noise, 0.1%, 0.2%, 0.3%, and 0.6%. The average spectrum with 0.3% intensity noise is shown in green. At 680 nm and 1360 nm (indicated by the two vertical red dotted lines), the 0.1% intensity noise, as in the 280 MHz system, leads to excellent coherence while 0.6% intensity noise, as in the 3 GHz system,

renders serious coherence degradation (close to zero). This simulation helps understand why we cannot detect f_{CEO} in the 3-GHz system with the conventional method.

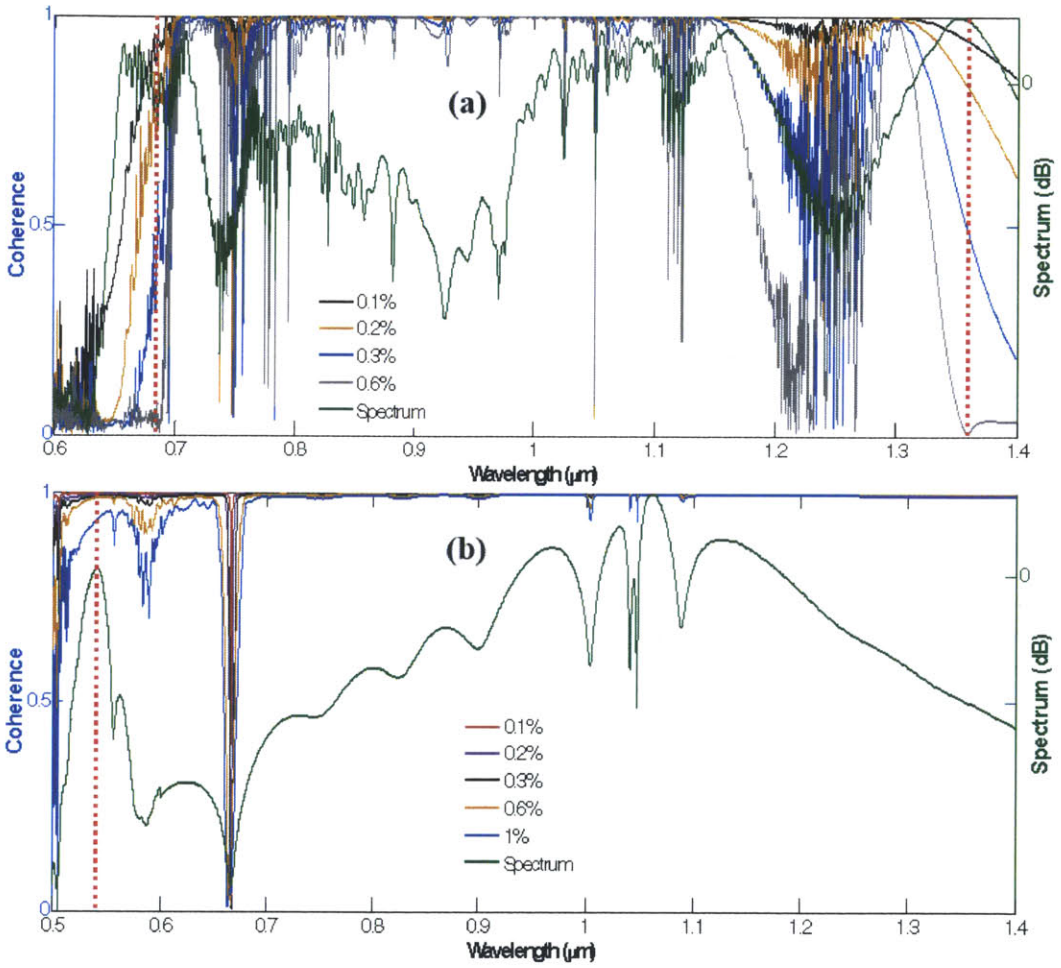

Fig. 8-2. (a) The calculated coherence and average spectrum of a 0.7 nJ pulse propagating in a 60-cm long PCF with ZDW 945 nm. (b) The calculated coherence of a 0.7 nJ pulse propagating in a 1.8-cm long PCF with ZDW 845 nm.

To overcome the issue of the deteriorated coherence arising from the intensity noise, our idea is to use a piece of PCF (< 5 cm) that can generate FOCR at ~520 nm and beat this FOCR with the SHG of the compressed pulse centered at 1045 nm to find the f_{CEO} beat note. The advantage of this scheme is that (1) the PCF is short so that the Raman soliton has not yet existed and hence there is no Raman soliton trapping the FOCR occurs. The coherence of FOCR will be significantly improved. (2) The SHG of the compressed pulse itself has excellent coherence. Beating this SHG

rather than the SHG of a Raman soliton with FOCR will definitely render a much better f_{CEO} beat note. (3) The power level of the SHG of the compressed pulses is much larger than that of the SHG of Raman soliton. Figure 8-2(b) shows the coherence at the output of a 1.8-cm long PCF that generates FOCR at ~520 nm. The resulting coherence is much better than the SC coherence in Fig. 8-2(a) even when the intensity noise is as high as 1%. Therefore, we should be able to either beat the 520 nm FOCR with the SHG of the compressed pulse centered at 1045 nm to generate and stabilize f_{CEO}. In this experiment, we used a 4-cm long PCF NL-2.8-850-02 to generate FOCR at ~522 nm.

Figure 8-3 shows the normalized spectra of the FOCR, the compressed pules, and the SHG of the compressed pulses. The spectrum of the SHG overlaps with that of the FOCR. However, we failed to detect f_{CEO} beat note with all these efforts.

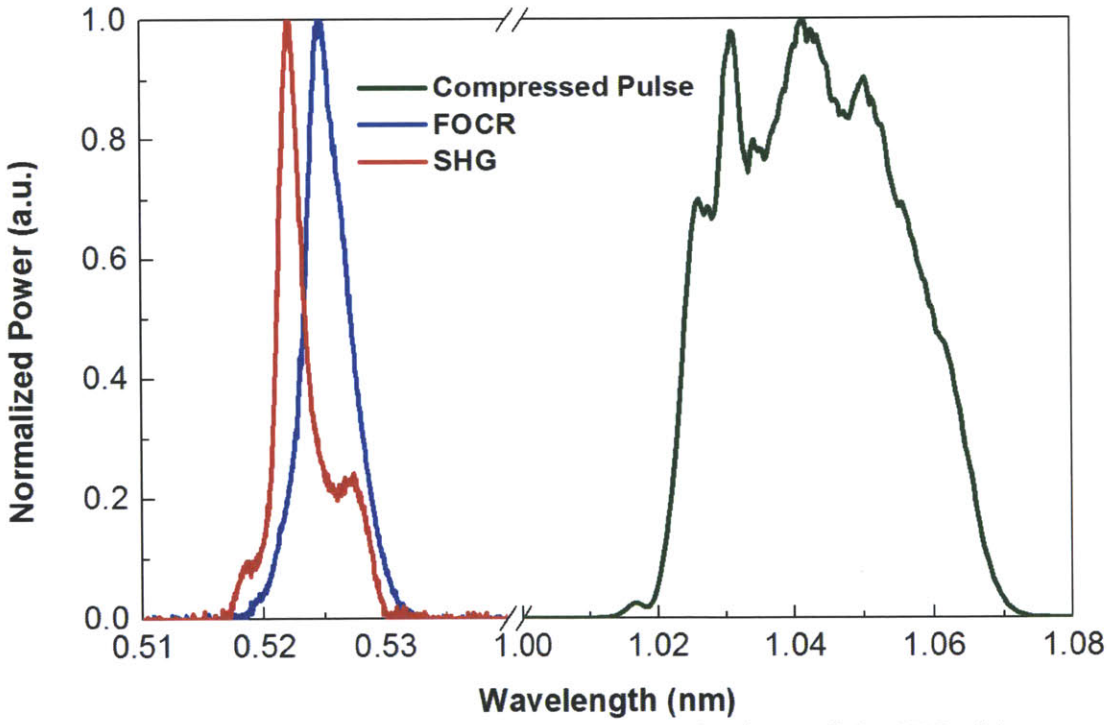

Fig. 8-3. The spectra of the FOCR, the compressed pules, and the SHG of the compressed pulses.

8.3. Passive Frequency Comb based on Difference Frequency Generation

The experiments and simulation in the previous section have excluded the possibility that it is the intensity noise that makes f_{CEO} beat note undetectable. The main reason could be that the optical linewidth of the 3 GHz laser is too broad or the timing jitter is too large such that the signal-to-noise ratio of the f_{CEO} beat note is too low and the beat note is buried below the background noise of the RF spectrum.

Therefore, we can employ a totally different way of building a CEO-stabilized frequency comb via difference frequency generation (DFG) to avoid the f_{CEO} locking part because the resulting DFG source has zero CEO frequency. We performed the DFG in periodically-poled lithium niobate (PPLN) using the FOCR as the pump and part of the compressed pulse as the signal to generate a DFG wavelength at around 1550 nm. Then a passive frequency comb can be built by only stabilizing f_{rep}.

8.3.1 Passive Frequency Comb ($f_{CEO} = 0$)

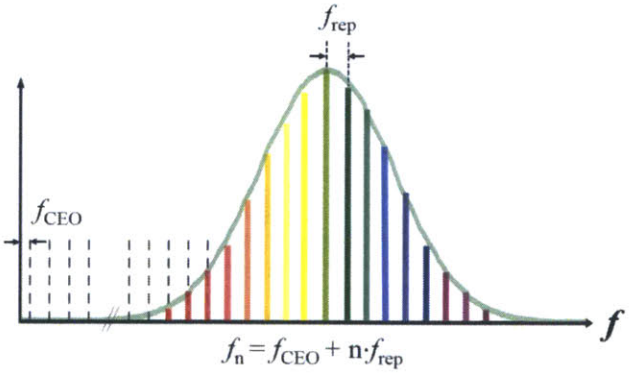

Fig. 8-4. The n^{th} optical frequencies, f_n, of the comb lines from a modelocked laser where $f_n = f_{CEO} + n \cdot f_{rep}$.

The n^{th} optical frequency of the comb lines from a modelocked laser shown in Fig. 8-4 can be written as $f_n = f_{CEO} + n \cdot f_{rep}$, where f_{CEO} is the carrier-envelope-offset frequency and f_{rep} is the repetition rate. f_{CEO} is related to f_{rep} by $f_{CEO} = (\Delta\Phi_{CE}/2\pi) \cdot f_{rep}$ where $\Delta\Phi_{CE}$ is the carrier-envelope

phase shift and is attributed to the pulse propagation in a dispersive medium, causing the pulse envelope and carrier wave to travel at different velocities in the laser cavity. Without active stabilization, f_{CEO} and f_{rep} would drift due to a host of environmental disturbances, leading to changes in the laser's cavity length, refractive index, and nonlinear dynamics. By stabilizing two parameters (i.e. f_{CEO} and f_{rep}), we can implement a frequency comb.

In our experiment, since f_{CEO} is still undetectable, we can build the 3 GHz frequency comb by avoiding the need for locking f_{CEO}. That is, we can perform difference frequency generation by mixing two frequencies, f_{n1} and f_{n2}. The DFG frequency is:

$$f_{DFG} = f_{n1} - f_{n2} = (f_{CEO} + n_2 \cdot f_{rep}) - (f_{CEO} + n_1 \cdot f_{rep}) = (n_2 - n_1) \cdot f_{rep}.$$

In this case, the DFG source has zero CEO frequency and a passive frequency comb can be built by only stabilizing the repetition rate, f_{rep}.

8.3.2 Experimental Setup and Results

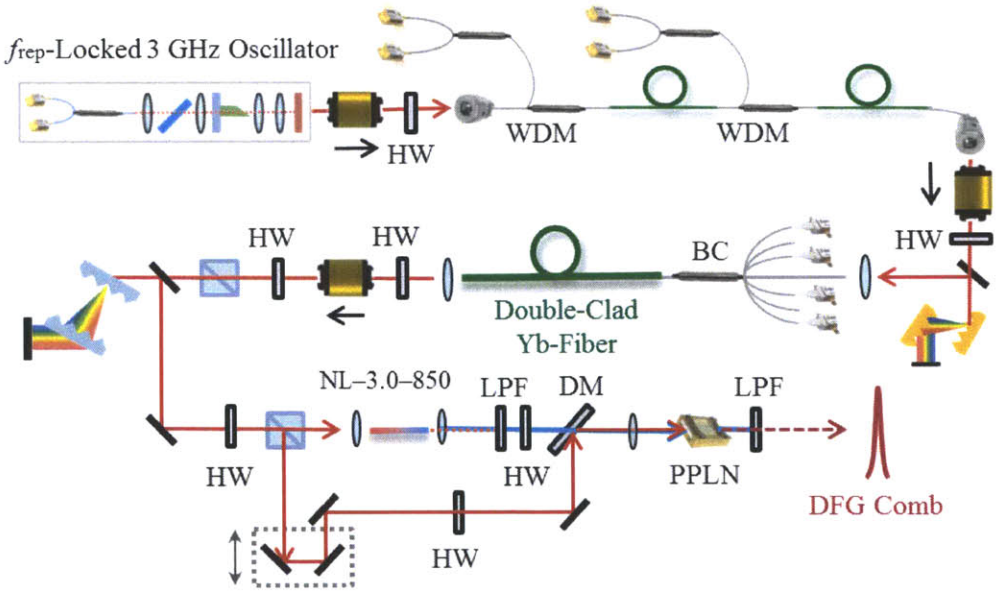

Fig. 8-5. Schematic experimental setup of the 3 GHz DFG source. HW: half-wave plate; PBC: polarization beam combiner; BC: (6+1)x1 beam combiner;

LPF: long-wavelength-pass optical filter; DM: dichroic mirror; and
PPLN: periodically-poled lithium niobate.

To build a DFG comb, we aim to generate a DFG wavelength at 1.5 μm which is in the Er-doped fiber laser wavelength so that the generated DFG can be further amplified to a higher power level for future applications. Besides, the only single-mode narrow linewidth external cavity diode laser (ECDL, Photonetics Tunics-PR/PRI) available in our lab has a wavelength of 1.5 μm. We can investigate the DFG linewidth by beating the DFG source against the ECDL. The experimental setup is shown in Fig. 8-5. As demonstrated in section 5.3.2, the repetition rate, f_{rep}, is always stabilized to a RF synthesizer (Agilent E8257D) during the experiment. One part of the compressed pulse from the 3 GHz laser system is coupled into a PCF.

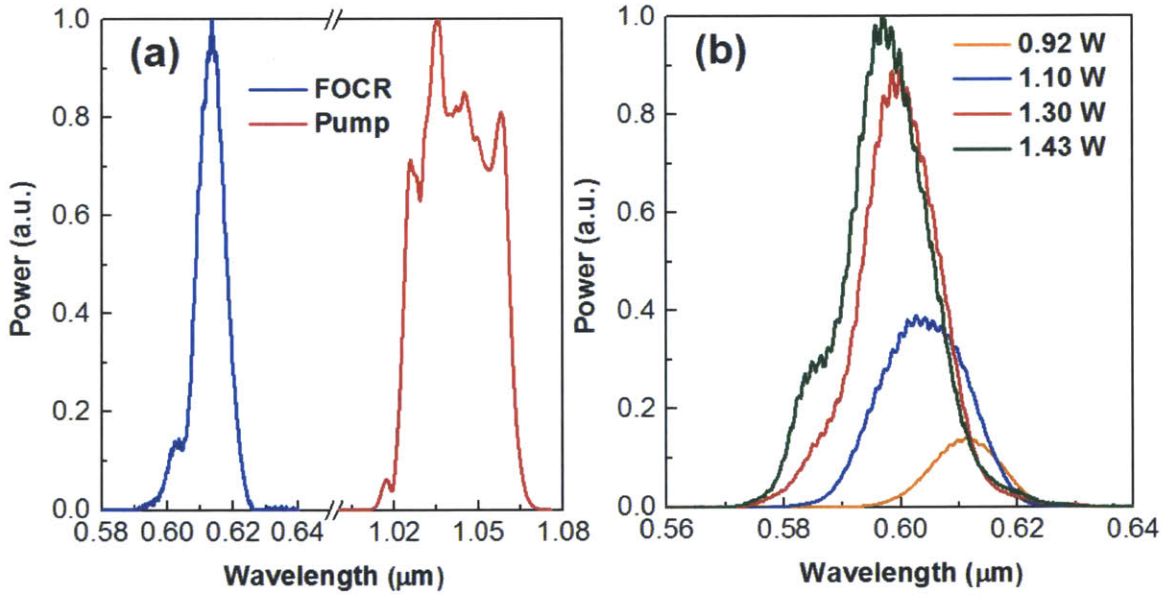

Fig. 8-6. (a) The spectra of the pump (compressed pulses) and the FOCR generated by a 4-cm PCF NL-3.0-850. (b) The FOCR spectra with different PCF input power.

We choose the PCF NL-3.0-850 to generate the FOCR at around 620 nm. The PCF is only 4-cm long such that the generated FOCR can hold good coherence. The remaining part works as the pump and is later combined with the FOCR at the PCF output by a dichroic mirror. The combined beam is then coupled into a 2-mm-long MgO doped PPNL crystal

(Covesion MSFG612-0.5) to generate the DFG source. The spectra of the pump and the FOCR are shown in Fig. 8-6(a). The FOCR spectrum varies with the coupled power into PCF as shown in Fig. 8-6(b). When 0.92 W power is coupled into the PCF, 3-4 mW FOCR is generated at 617 nm. Although the higher coupler power increases the efficiency of dispersive wave, the wavelength is more blue-shifted such that it is out of phase-matching condition of the PPLN. By tuning the relative time delay between two pulses, we can achieve different DFG spectra as shown in Fig. 8-7. Typical DFG power near 1.5 μm was ~10 μW after two long-pass filters (Edmund optics #48-565 and Semrock BLP01-1319R-25). The PPLN polling period was 10.85 μm at the crystal temperature 110°C. Note that this is just a preliminary result. Higher DFG power can be reached by using a longer PPLN crystal.

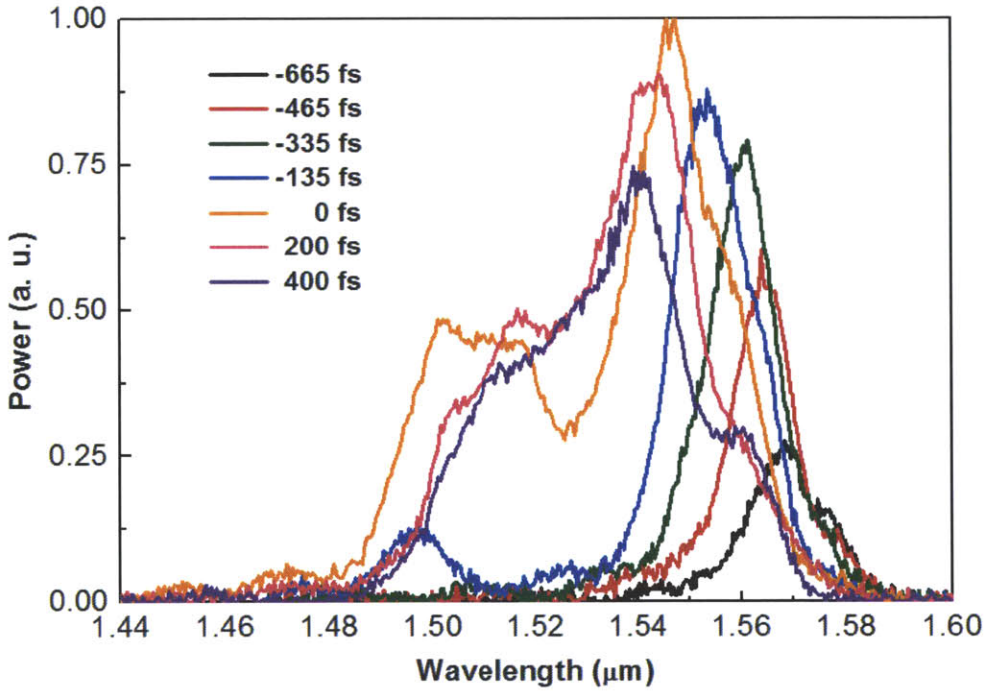

Fig. 8-7. The spectra of the DFG comb with different relative time delays between the pump and the FOCR.

8.3.3 Optical Linewidth of the 3 GHz passive comb

To check the optical linewidth of this stabilized DFG comb, we performed the heterodyne beat note measurement between one of the DFG comb lines and the ECDL at 1.5 um whose typical FWHM linewidth is ~100 kHz. The DFG comb is coupled into one port of a 50/50 fiber beam combiner with the coupling efficiency of 20% and the fiber-coupled output of ECDL is coupled into the other input port. The combined output is then detected by a photodetector (New Focus Model 1601-AC). The measured RF spectrum, with ~-68 dBm peak power, of the beat note is shown in Fig. 8-8. The signal-to-noise ratio is ~15 dB because of the low DFG power at 1.5μm. The beat note fitted to a Lorentzian shape shows a linewidth of ~1.5 MHz.

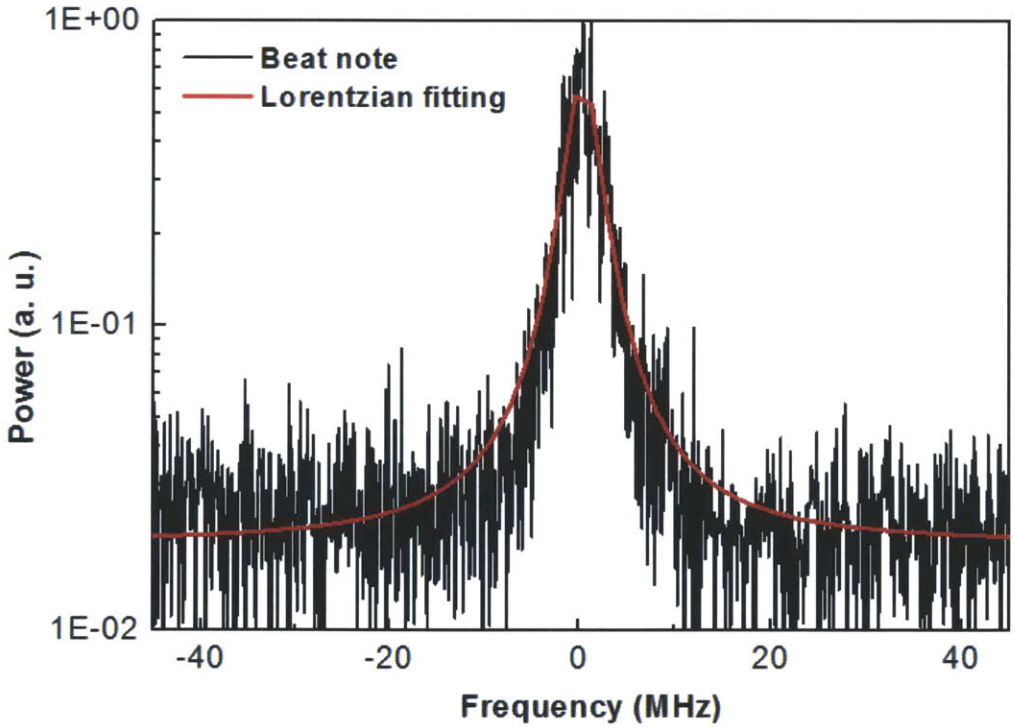

Fig. 8-8. The measured heterodyne beat note between one of the DFG comb line and the ECDL at 1.5 um. The beat note fitted to a Lorentzian shape shows a linewidth of ~1.5MHz.

8.4. Summary

To summarize, the 3 GHz passive comb is implemented by difference frequency generation. To the best of our knowledge, this is the frequency comb with highest rep-rate within the telecommunication wavelength range. Ongoing work includes increasing the power of the DFG comb and narrowing the comb linewidth. The DFG wavelength is within the Er:fiber wavelength and can be further amplified to a higher power level for future applications.

Chapter 9

Conclusion and Future Work: Towards a 3-GHz Yb-Fiber Astro-Comb

9.1. Conclusion

In this dissertation, we demonstrate 3 GHz femtosecond laser sources are demonstrated. These sources are useful for applications in optical coherence tomography, optical frequency metrology, multi-photon biological imaging, photonic analog-to-digital conversion, etc. First, a 3-GHz fundamentally mode-locked Yb-fiber laser is demonstrated with the highest rep-rate among all femtosecond Yb-fiber lasers to date. We then numerically and experimentally study the optimization of femtosecond YDFAs in order to achieve both high-quality and high-power compressed pulses for the 3 GHz high power fiber laser system. Using the 3 GHz high power femtosecond Yb-fiber laser system, a few-cycle ultrafast laser source at the Ti:sapphire laser wavelength is demonstrated as a promising substitute for multi-GHz mode-locked Ti:sapphire lasers. In addition, a watt-level femtosecond Raman soliton source, wavelength-tunable from 1.15 μm to 1.35 μm, is implemented. Such a Raman soliton source exhibits both the highest repetition rate and highest average power to the best of our knowledge. At last, we also show the preliminary work on a 3 GHz passive frequency comb via difference frequency generation at

1.5 μm, which is currently the highest rep-rate frequency comb in the telecommunication wavelength range.

9.2. Current Issues

We have introduced several experiments on improving f_{CEO} and finding f_{CEO} beat note in the 3 GHz laser system. Because f_{CEO} is still undetectable, we resorted to building a passive frequency comb via difference frequency generation. A typical fiber laser frequency comb has a linewidth of ~100 KHz or even narrower. As shown in Fig. 8-8. The measured heterodyne beat note between one of the DFG comb line and the ECDL at 1.5 um. The beat note fitted to a Lorentzian shape shows a linewidth of ~1.5MHz. On the other hand, we can estimate the optical linewidth from the comb-line equation. Consider the comb line of the DFG comb at 1.5 um, $f_{DFG} = f_{n1} - f_{n2} = (n_2 - n_1) \cdot f_{rep}$ where $f_{rep} = 3$ GHz, the mode number of the comb line $(n_2 - n_1)$ is $2/3 \times 10^5$. The linewidth of the locked f_{rep} in Fig. 5-9(b) has a linewidth of ~75 Hz ($\Delta f_{rep} = 75$ Hz). Therefore, we can get the estimated value of the DFG linewidth by $\Delta f_{DFG} = (n_2 - n_1) \cdot \Delta f_{rep} = 2/3 * 10^5 \times 75 = 5$ MHz. It turns out the measured linewidth 1.5 MHz is close to the estimated value.

We also tried to measure the optical linewidth with the 3 GHz oscillator. However, at that moment the only two single-wavelength laser diodes we could borrow at MIT were at 1064 nm and 1500 nm. Since the output spectrum from the oscillator does not contain 1064 nm, we instead measured the optical linewidth of the 3 GHz high power laser system at 1064 nm and the linewidth is ~20 MHz. In this case, we can have a rough estimation of Δf_{CEO} being larger than 10 MHz. This might explain why f_{CEO} is undetectable. It is too broad such that the signal-to-noise ratio of f_{CEO} is very poor. Consequently, to improve the DFG linewidth to one order narrower ~100 kHz, one solution is that we can work on improving the f_{rep} linewidth Δf_{rep}. If we can reduce the f_{rep} linewidth

one order of magnitude smaller, we should be able to achieve a passive comb with optical linewidth ~100 kHz. The task now becomes how to reduce the f_{rep} linewidth of the 3 GHz oscillator.

Among the three 3 GHz Yb-fiber oscillators we built, we found the free-running f_{rep} linewidth of the DESY one (Fig. 2-9) has a f_{rep} linewidth of ~1 kHz which is one order smaller than those of the other two oscillators (~ 11 kHz). The only difference in these oscillators is that in the DESY oscillator we employed a new model of a standalone diode driver controller (Thorlabs CLD1015). Figure 9-1 shows the RIN measurement of the same pump diode using different diode controllers in our labs. The Thorlabs controller produces the lowest intensity noise among all the other diode controllers.

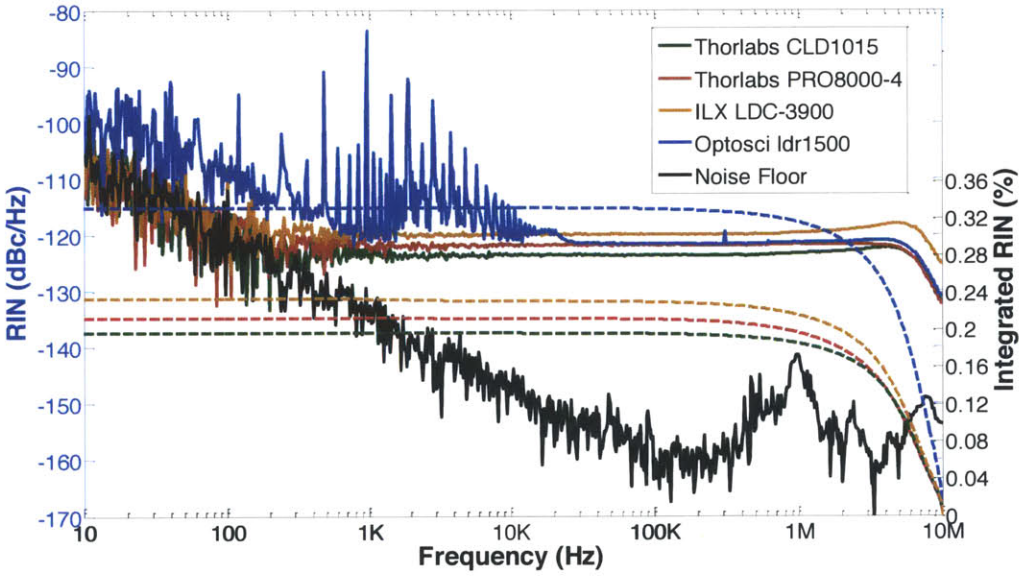

Fig. 9-1. RIN measurements of the same pump diode driven by different diode driver controller. The dashed curves are the integrated RIN.

9.3. Future Work

9.3.1 Optical Linewidth Improvement

The next plan on improving the optical linewidth is to lock the f_{rep} of the 3 GHz oscillator with the Thorlabs diode controller and measure the optical linewidth directly from the 3-GHz

oscillator. We can also replace the pump diode with a single-wavelength pump diode. This experiment can be done at DESY because there is an ultra-stable cavity-stabilized laser at 1030 nm.

9.3.2 A Simpler Way to Build the 3 GHz Frequency Comb

Eventually a simpler way to implement a 3 GHz frequency comb is to lock the f_{rep} first and then lock one of the comb lines from the oscillator to an ultra-stable cavity-stabilized laser at 1030 nm.

9.3.3 Blue and Green Astro-Comb

Once we have a frequency comb, we need to perform nonlinear wavelength conversion from 1 μm to the green or blue spectrum. This requires the generation of fiber-optic Cherenkov radiation as demonstrated in Chapter 6. Furthermore, we might not be able to generate the green or blue spectrum to be as broad as we want. This requires the aid of numerical calculation on pulse propagation in a PCF taper to estimate the tapering ration, the length and the type of the PCF.

9.3.4 All-fiber 10-GHz Yb-fiber Oscillator

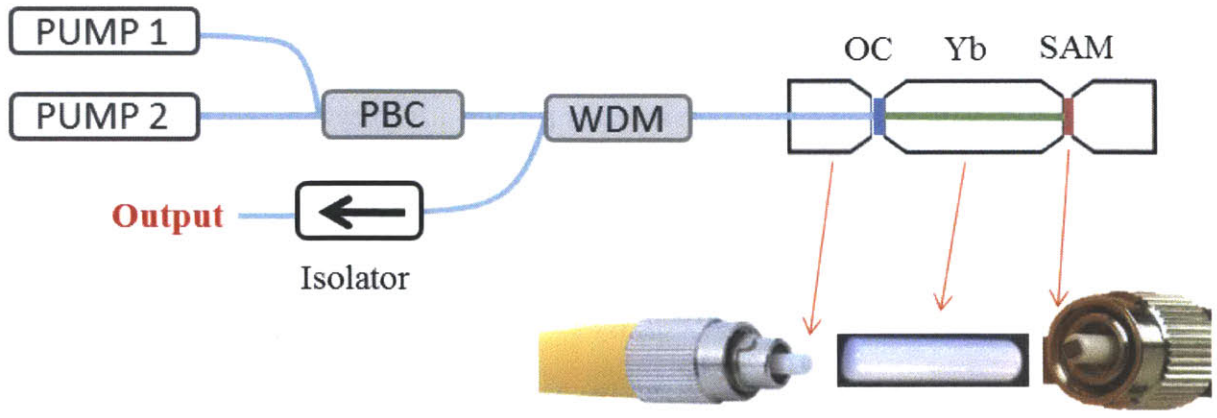

Fig. 9-2. The proposed schematic setup of an all-fiber 10-GHz Yb-fiber oscillator.

Finally, to achieve an even higher repetition rate up to 10 GHz, an all-fiber 10-GHz Yb-fiber oscillator is proposed in Fig. 9-2. The output coupler coating is directly coated on one end of the 1-cm long Yb-fiber and that end can be directly connected to a fiber end of a WDM by a mating sleeve. With such a design, a very robust and relatively low-loss connection is obtained compared to free space coupling of the pump into the gain fiber. Besides, the SBR can be mounted on a fiber connector so that it can be connected to the other end of the Yb-fiber by another mating sleeve.

Appendix A

Chirally-Coupled-Core Modelocked Yb-Fiber Oscillator

A.1. Introduction

Power/energy scaling of ultrafast Yb-fiber oscillators has experienced rapid progress largely driven by many real-world applications that desire high peak and average power femtosecond pulses. For moderate pulse energies, high power/energy Yb-fiber oscillators may replace current complicated master-oscillator-power-amplifier (MOPA) systems. The bottleneck in constructing high power/energy Yb-fiber oscillators arises from the accumulated nonlinear phase due to tight confinement of ultrashort pulses circulating inside the fiber. Stable mode-locking limits the nonlinear phase below a certain threshold to avoid the onset of detrimental effects, e.g., multiple pulsing. Two orthogonal approaches are being pursuit to overcome this limitation: 1) temporally elongate the pulse inside the fiber and 2) spatially relax the confinement exerted by the fiber to the optical beam. The first approach is implemented via managing laser cavity dispersion. Depending on the amount of net cavity dispersion, the intra-cavity pulse exhibits a duration ranging from sub-ps to ~10 ps, corresponding to different mode-locking regimes (i.e. soliton, stretched-pulse, similariton, and dissipative soliton) [134]. For example, dissipative soliton lasers possess large positive net cavity dispersion. Its intra-cavity pulse is strongly chirped and stretched which in turn substantially reduces the acquired nonlinear phase and thus facilitates formation of high energy

pulses. Recently, a 30-nJ dissipative soliton laser based on double-clad single-mode Yb-doped fiber has been demonstrated [135]. The second scaling approach relies on the use of large-mode-area (LMA) Yb-fibers that have been widely incorporated into high power/energy fiber amplifiers. To retain a diffraction-limited beam quality—one of the most important merits for fiber lasers, special care must be taken to ensure that the LMA Yb-fiber operates at fundamental mode (i.e. LP01 mode) although it also accommodates higher-order modes. Using a photonic crystal LMA Yb-fiber (4000 μm^2 mode-area) as the gain medium and a fiber-based mode filter to improve intra-cavity beam quality, pulses with sub-μJ energy and sub-ps (711 fs after compression) duration have been generated [136]. For generation of ultrafast (~100 fs after compression) pulses, pulse energies >100 nJ are demonstrated using the same type of fiber with smaller mode-area [137,138]. Despite remarkable success in implementing high power/energy laser system, photonic crystal LMA fibers suffer from high splicing loss and cannot be tightly coiled for compact packaging, which offset key advantages (e.g. robustness and monolithic integration) offered by conventional single-mode fiber technology.

Yb-fiber oscillators normally emit positively chirped pulses. Dechirping these pulses to their transform-limited duration necessitates external compression. Most systems exploit a pair of dielectric diffraction-gratings working at a double-pass configuration to accomplish the compression. Dielectric gratings outperform their standard metal-coated counterparts in terms of power/energy handling capability. Nonetheless, diffraction-grating based compressors demand critical alignment and lack robustness. Even a slight misalignment may introduce noticeable spatial chirp and pulse front tilt, thus degrading the excellent beam quality warranted by the fiber oscillator itself. Furthermore, diffraction-grating based compressors introduce a loss of at least 20%.

To address these drawbacks arising from photonic-crystal LMA Yb-fiber and diffraction-grating based compressors, we adopt two rapidly advancing technologies: chirally-coupled-core (3C) LMA fiber that only transmits pure fundamental-mode and high-dispersion mirror (HDM) that permits loss-free, spatial-distortion-free pulse compression. In this appendix, we first demonstrate an Yb-fiber laser system that delivers 25-nJ, 80-fs pulses at 39 MHz repetition rate with diffraction-limited (M^2=1.05) beam quality [26] and then demonstrate high-power (>10 W), 300-fs mode-locked oscillators at 83-MHz repetition rate using air-clad Chirally-Coupled-Core Yb-fiber with 37-μm central-core diameter, corresponding to a 30-μm mode-field-diameter.

A.2. Key elements: 3C LMA fiber and HDMs

In contrast to traditional LMA fibers that require special care to ensure fundamental mode propagation, 3C LMA fibers intrinsically support only the LP01 mode, making them indistinguishable from conventional single-mode fibers [139–142]. As shown in Fig. A-1, a typical 3C fiber consists of a large straight central core and at least one smaller side core that is chirally wound around the main core [140]. Higher-order modes of the central core are efficiently coupled to the side core where they are strongly attenuated by a high propagation loss. Thus 3C LMA fibers are effectively single-mode and do not rely on any external mode management or require coiling in any specific geometry. The fibers allow simple low-loss (~0.05-0.1 dB) splicing for both passive-to-passive and gain-fiber-to-passive without causing modal distortion. 3C LMA Yb-fibers have been incorporated into CW fiber lasers achieving up to 250-W of output power [141] and a MOPA system (as the amplifier) generating 150-W, 10-ns pulses at 250-kHz repetition rate [142]. However, a mode-locked oscillator employing this new class of fiber has not been demonstrated.

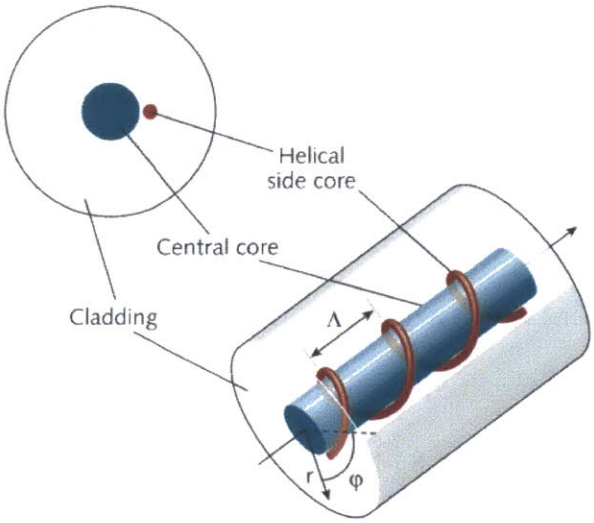

Fig. A-1. Chirally coupled core fiber uses a central guiding core with at least one satellite core wrapped helically around it. Upper left figure shows fiber end face [140].

Chirped multilayer coatings, such as HDMs, represent another breakthrough in laser technology and have experienced tremendous developments for more than one decade [143]. They are widely used in solid-state (especially Ti:sapphire) lasers to provide broadband dispersion control of few-cycle pulses. Recently, there is considerable research interest in developing HDMs and incorporating them into ultrafast solid-state lasers [144–146]. A HDM provides negative group-delay dispersion (GDD) in the range between -1000 fs^2 and -2000 fs^2, about three orders of magnitude less than what can be achieved from a diffraction-grating pair. At first glance, HDMs are by no means a substitute for diffraction-gratings to compress chirped pulses in a fiber laser system. This is definitely true for a fiber MOPA system employing chirped-pulse amplification, in which the pulse is typically pre-stretched to > 100 ps. The chirped pulse directly emitted from an Yb-fiber oscillator, however, is typically at the ps level in duration; in this scenario, a compressor constructed from HDMs is entirely possible. As a proof of concept, we successfully dechirp a sub-ps pulse (generated by a 3C Yb-fiber oscillator) to 80-fs duration using 6 bounces from home-designed HDMs (-2000 fs^2 GDD for each bounce).

A.3. Experimental Setup and Results

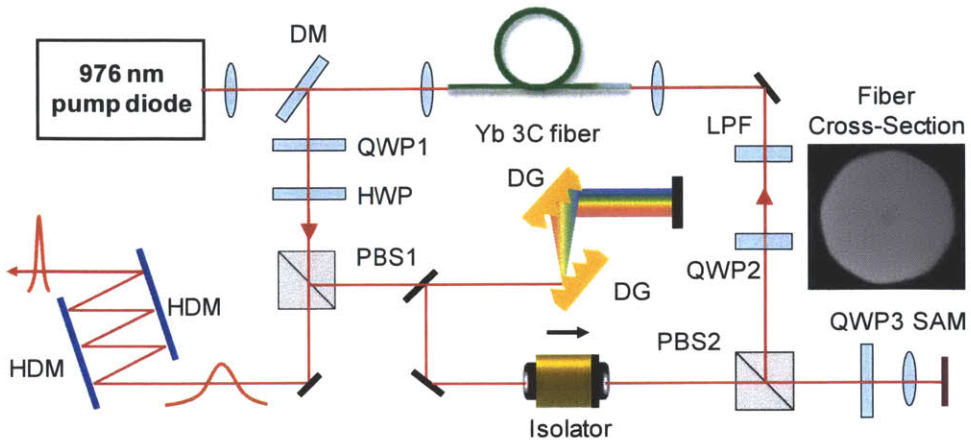

Fig. A-2. Schematic setup of the laser system. DM: dichroic mirror; QWP: quarter-wave plate; HWP: half-wave plate; LPF: long-pass filter; PBS: polarization beam splitter; SAM: saturable absorber mirror; HDM: high-dispersion mirror. The fiber's cross-section shows the central core and the side core.

Figure A-2 illustrates the schematic setup. The 976-nm pump with 45-W maximum power is delivered by a 400-μm core-diameter fiber with 0.22 NA. A dichroic mirror transmits the pump and reflects the lasing pulse that circulates counter-clockwise inside the ring-cavity. Arbor Photonics provided 3C fiber (4.2 m) with an Yb-doped central core of 33.5-μm diameter (21-μm mode-diameter, 0.059-NA) and a 250-μm 0.46-NA hexagonal-shaped inner cladding (inset of Fig. 1). The coupling efficiency of pump light into the 3C fiber length is 75%. The growth of total forward and backward ASE (i.e. amplified spontaneous emission) has a threshold of 4 W absorbed pump power. Mode-locking is initiated by a commercially available saturable absorber mirror (SAM) that has 35% modulation depth and 500-fs relaxation time. A combination of wave plates (i.e. QWP1, HWP, and QWP2 in Fig. A-2) and polarizer (i.e. PBS1 in Fig. A-2) provides an additional mode-locking mechanism via nonlinear polarization evolution (NPE) that significantly reshapes the intra-cavity pulse. Rotation of these three wave plates leads to different mode-locking states. A pair of 600-line/mm diffraction-gratings at a double-pass configuration

provides negative group-delay dispersion to control the net cavity dispersion. A long-wavelength pass filter with a cutoff wavelength at 980 nm blocks the unabsorbed pump to prevent it from causing damage on the SAM. An optical isolator ensures unidirectional circulation of the intra-cavity pulse. Single-pulse operation is monitored using a long-range autocorrelation and optical/RF spectral measurements.

By changing the net intra-cavity dispersion, the laser may run in the similariton or dissipative soliton regime, leading to output spectra with sharp falling edges and spiky features that impose a large pedestal onto the externally compressed pulse. To avoid compromising pulse quality, the net cavity dispersion in the current setup is slightly negative and the laser operates in the stretched-pulse mode-locking regime. The direct output pulse ejected from PBS1 exhibits positive chirp with sub-ps duration. In our system, we use home-designed HDMs as the compressor. As shown in Fig. A-3, the HDM includes 55 alternating layers of Nb_2O_5 and SiO_2; each bounce provides a dispersion of -2000 fs^2 with a reflectivity >99.99%. The optimal structure in terms of layer number and thickness is determined by minimizing the integrated phase distortion ratio (PDR) with uniform weighting, which minimizes the fraction of optical pulse energy pulled into phase distortions in each bounce [147]. While this is not necessarily equivalent to minimizing the resulting pulse width, per se, optimizing the PDR has been empirically shown to yield shorter pulses than optimizing GDD or GD [14]. Figure A-4 shows the auto-correlation (AC) trace duration of the compressed pulse versus number of bounces from HDMs. The inset (a) plots the designed and measured group delay as a function of wavelength and the inset (b) indicates the corresponding spectrum of the pulse. The AC trace duration continuously deceases from initial 510 fs to 210 fs after 6 bounces and then starts to increase with more bounces. The measured transmission of the compressor with 6 bounces is >99%. It is noteworthy that each bounce shortens

the AC duration by about 60 fs prior to the 6th bounce, which agrees with the fact that the optical spectrum has 10-nm bandwidth (inset (a) Fig. A-4), corresponding to a 120fs FWHM transform limited pulse having a 170-fs AC duration. The deviation of our best compression (210-fs AC duration, inset (b) in Fig. A-4) from the transform-limited duration is mostly due to the discrete nature of the dispersion compensation using HDMs with -2000 fs^2 dispersion per bounce.

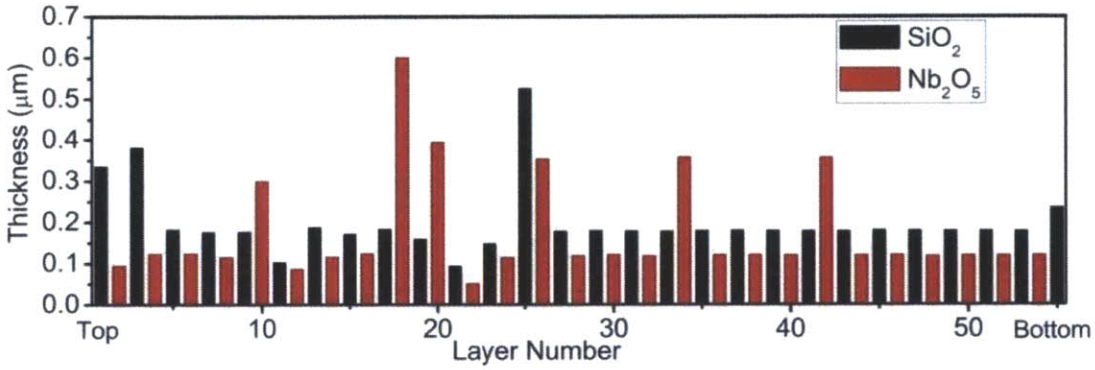

Fig. A-3. Structure of the home-designed high-dispersion mirror.

In an Yb-fiber laser system that employs a diffraction-grating compressor, optimization of compression is achieved by varying grating separation which results in a tunable dispersion to match the input chirped pulse. As a contrast, the total dispersion from a HDM compressor cannot be continuously adjusted. We can, however, vary the emitted pulse's chirp to match the HDM compressor by tweaking laser parameters, such as pump power, separation of diffraction-grating pair, mode-locking state owing to NPE etc. Changing the settings of NPE followed by fine tuning of the pump power can significantly improve the compression and bring the compressed pulse close to its transform-limited duration. Figure A-5 presents an optimized compression of the laser pulse resulting from a different mode-locking state with increased intra-cavity power. The spectrum (inset (a) in Fig. A-5) has twice the bandwidth of the former mode-locking state. The laser emits 970-mW average power corresponding to 25-nJ pulse energy. After 6 HDM bounces,

the measured AC trace (red, solid line) has a duration of 110 fs, only 10-fs longer than its calculated counterpart (blue dashed line) using the transform-limited pulse. The full-width-half-maximum duration of the experimentally compressed pulse is estimated to be 80 fs, slightly longer than its transform-limited duration. The RF spectrum, shown in the same figure as inset (b), exhibits a >60 dB signal to background ratio; and the integrated relative intensity noise is less than 1%.

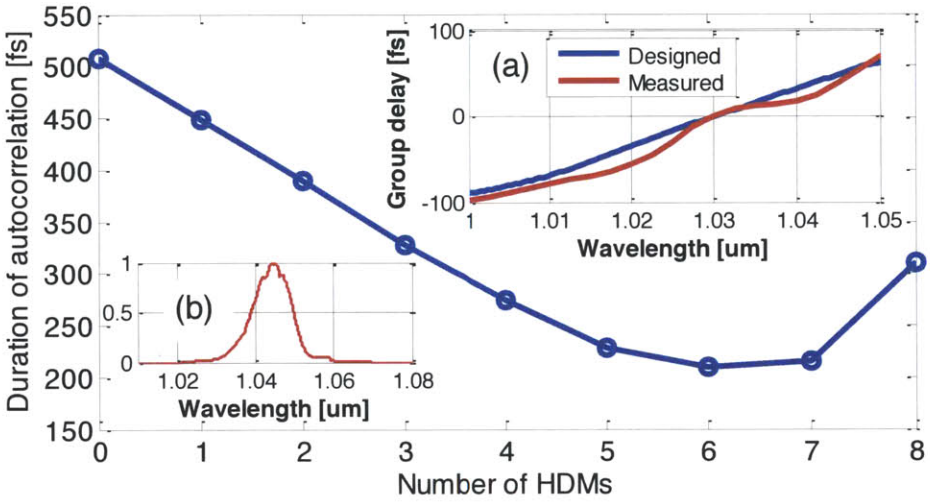

Fig. A-4. Duration of AC trace versus number of HDM bounces. Inset: (a) designed (blue, solid line) and measured (red, dashed line) group delay as a function of wavelength and (b) the optical spectrum of the pulse.

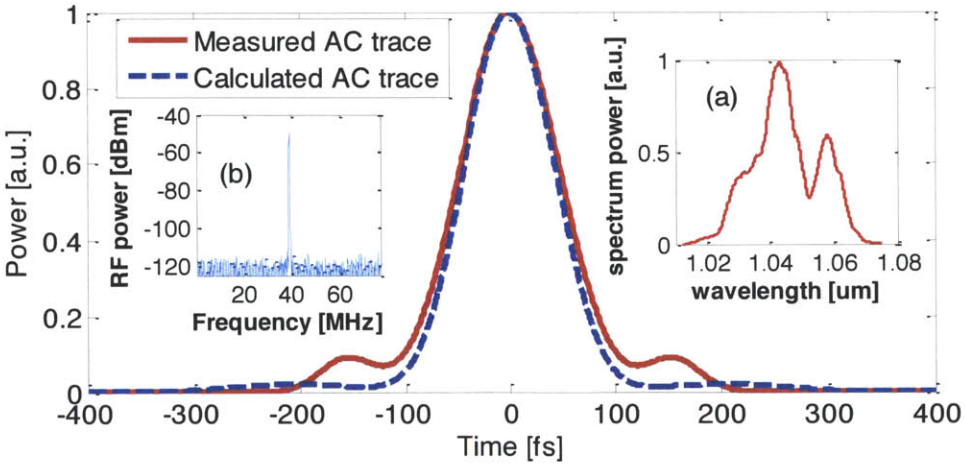

Fig. A-5. Compression of a broadband pulse. Two curves represent the measured AC trace (red, solid line) and calculated AC trace (blue, dashed line) corresponding to the transform-limited pulse, and. Inset: (a) optical spectrum and (b) RF spectrum measured at resolution bandwidth of 300 kHz.

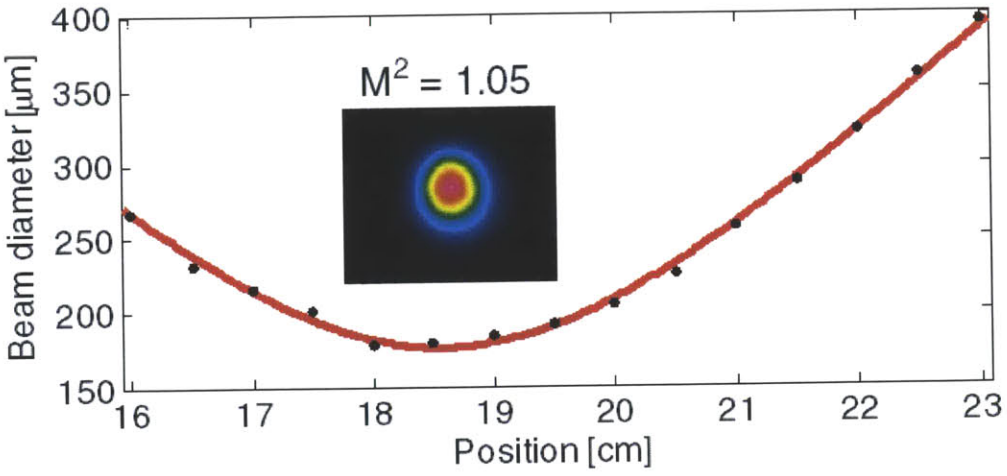

Fig. A-6. Beam profile and M^2 measurement of the compressed pulses. M^2=1.05 indicates that the HDM based compressor preserves the diffraction-limited beam quality of the 3C Yb-fiber oscillator

In the laser community, M^2 has become a standard measure to quantify the optical beam quality. Measuring M^2 is widely performed for CW or nano-second pulsed fiber lasers; it rarely appears in the work of high power/energy *ultrafast* LMA-fiber lasers. To the best of our knowledge, M^2 measurements of compressed pulses from LMA fiber lasers have not been reported. To verify that the HDM compressor does preserve incident beam quality from the 3C Yb-fiber oscillator, we have measured M^2 of the optical beam before and after the compressor under a variety of laser operation states: non-lasing (i.e. pump power below threshold or cavity blocked), CW lasing, and mode-locking at different states. All the measured values fall into a range of 1.03-1.07. Figure A-6 plots the beam profile and M^2 measurement for the compressed pulse shown in Fig. A-5. M^2=1.05 evidently confirms that the loss-free compressor based on HDMs maintains the diffraction-limited beam quality that originates from the 3C Yb-fiber. Note that single-mode operation of the 3C fiber has been tested separately by feeding in a broadband optical source and recording the transmitted optical spectrum (similar to S^2 measurement [148]); no noticeable

modulation is observed, which indicates that the fiber is truly single-mode (i.e. LP_{01}). Therefore the M^2 measurement undoubtedly confirms that the HDM compressor is distortion free and we do achieve diffraction-limited beam quality.

A.4. Discussion

As discussed, the key to energy scaling of fiber lasers is reducing the fiber-optic nonlinear effects by 1) increasing spatial mode-area inside fiber and 2) increasing intra-cavity pulse duration. As for our laser configuration, these two methods translate to demanding a 3C Yb-fiber with larger mode-area and 2) more dispersion from a HDM compressor to dechirp a longer emitted pulse. Work with significantly larger core 3C fibers is ongoing. In the current setup, we use 6 HDM bounces for optimal compression. Compressing longer emitted pulses requires more bounces. Eventually it is the fabrication error on layer thickness that limits the maximum permitted number of bounces before reaching an unacceptable compression quality. By taking into account fabrication errors, 10 bounces on our HDMs introduce negligible phase error for an optical pulse with 40-nm bandwidth. Further optimization should allow a robust mirror design less susceptible to fabrication errors [147].

In conclusion, we demonstrate a high-energy femtosecond laser system that incorporates two rapidly advancing technologies: chirally-coupled-core large-mode-area Yb-fiber to ensure fundamental-mode operation and high-dispersion mirrors to enable loss-free pulse compression while preserving the diffraction-limited beam quality. Mode-locking is initiated by a saturable absorber mirror and further pulse shortening is achieved by nonlinear polarization evolution. Centered at 1045 nm with 39-MHz repetition rate, the laser emits 25-nJ, positively chirped pulses with 970-mW average power. 6 bounces from double-chirped-mirrors compress these pulses down

to 80 fs, close to their transform-limited duration. The loss-free compression gives rise to a diffraction-limited optical beam (M^2=1.05).

A.5. Further Power Scaling with Air-clad CCC Fiber

Progress in developing high power/energy femtosecond Yb-fiber oscillators has rapidly advanced in recent years, primarily due to the use of large-mode-area (LMA) Yb-fibers to reduce the intracavity nonlinear phase. Using LMA (mode-field diameter of 75 μm) photonic crystal Yb-fiber, 0.8-μJ ultrashort pulses at 60 W have been achieved [149]. However, such photonic crystal Yb-fibers are sensitive to bending, and cannot be tightly coiled, which contrasts sharply with the key advantages (e.g. robustness, monolithicity, compactness, etc.) offered by conventional single-mode fiber technology.

Recently, chirally-coupled core (CCC) fibers have emerged as a new technological platform for the next generation fiber lasers. CCC fibers consist of two cores placed in optical proximity. The core in the center is straight along the fiber axis for the signal transmission. The second core (i.e., side core), is chirally wound around the center core. Much smaller in diameter, the side core exerts substantial propagation loss on the higher-order modes inside the center core so that only the fundamental mode propagates in the center core with minimal loss. Providing robust single-mode core-size scaling without the need of external mode-filtering or mode-matching methods, CCC fibers can be spliced together and coiled for compact packaging. Therefore they are well suited for fabricating standardized CCC-fiber pigtailed components with single-mode throughput [139,150].

Using the first-generation CCC Yb-fibers with 21-μm mode-field-diameter (MFD), two groups have demonstrated femtosecond mode-locked oscillators operating in the stretched-pulse regime (25-nJ pulse energy) [26] or all-normal dispersion regime (40-nJ pulse energy) [151].

Further energy/power scaling necessitates CCC Yb-fibers with much larger MFD. Recently, air-clad CCC Yb-fibers with 30-μm MFD were fabricated, leading to a demonstration of a 511 W fiber MOPA system featuring single-frequency and single-transverse mode [152]. Use of air-clad structure facilitates high pump-absorption (i.e., 8-dB/m), making this CCC Yb-fiber especially suitable for constructing high repetition-rate (e.g., ~100 MHz) and high-power oscillators employing short fiber length. In this section, we demonstrate a femtosecond, all-normal-dispersion oscillator operating at 83-MHz repetition rate with pulse energy > 140 nJ (average power > 10 W).

As Fig. A-7 shows, the oscillator consists of 1.7-m air-clad CCC fiber with an Yb-doped central core of 37-μm diameter (30-μm MFD, 0.07-NA), a 260-μm 0.6-NA inner cladding, and a 443-μm outer cladding. The 976-nm pump with 75-W maximum power is delivered by a 400-μm core-diameter fiber with NA=0.22. The dichroic mirror transmits the pump and reflects the lasing pulse that circulates counter-clockwise inside the ring-cavity. A combination of wave plates (i.e. QWP1, HWP, and QWP2 in Fig. A-7) and a polarization beam splitter (i.e. PBS in Fig. A-7) initiates the mode-locking via nonlinear polarization evolution (NPE) that significantly reshapes the intra-cavity pulse. Rotation of these three wave plates leads to different mode-locking states. Mode-locking is further stabilized by a bandpass filter with 4-nm full-width-half-maximum (FWHM). The optical isolator ensures the intracavity pulse circulating uni-directionally. The output pulse ejected from PBS exhibits a positive chirp with picosecond duration depending on the modelocking states. The output pulse is then compressed by a pair of gratings (600 line/mm line density) configured at double pass with ~50% transmission efficiency.

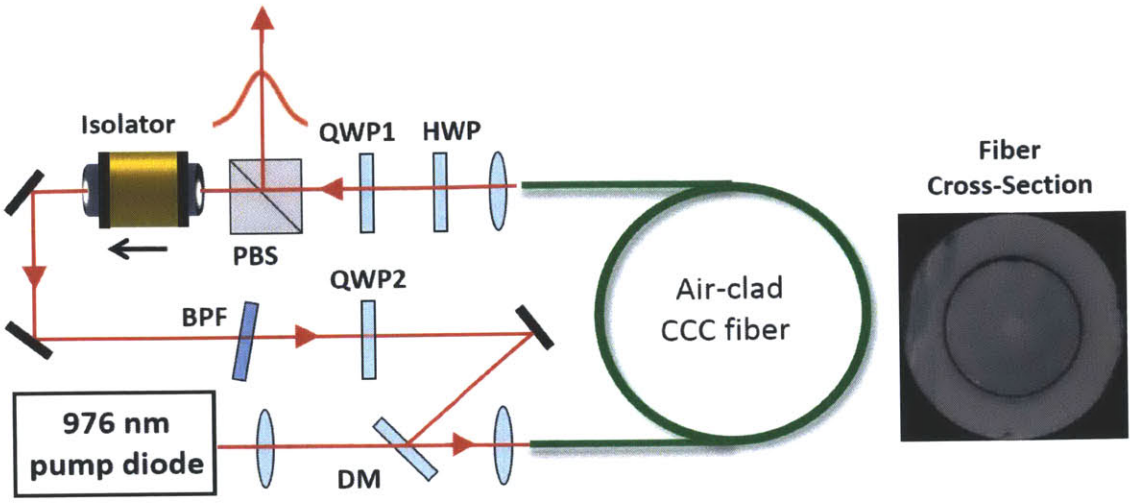

Fig. A-7. Schematic setup of the oscillator (left) and the fiber cross-section (right). DM: dichroic mirror; QWP: quarter-wave plate; HWP: half-wave plate; BPF: bandpass filter; PBS: polarization beam splitter.

Adjusting the wave plates varies the output coupling ratio, and leads to various self-starting modelocking states. The broadest output spectrum shown in Fig. A-8(a) has a 32-nm FWHM bandwidth and 5-W average power before the compressor. The spectral modulation indicates that the pulse experiences strong self-phase modulation when propagating inside the CCC fiber. We use an autocorrelator with 150-ps scanning range together with optical/RF spectral measurements to confirm single-pulse operation. The autocorrelation traces for the output pulse (black curve) and the compressed pulse (red curve) are shown in Fig. A-9(a); also plotted in the same figure is the calculated transform-limited pulse (blue curve) from the spectrum in Fig. A-8(a). The autocorrelation durations of the uncompressed and compressed pulses are 4 ps and 140 fs, respectively. The corresponding RF spectrum (inset in Fig. A-9(b)) and the RF measurement of the repetition-rate are shown in Fig. A-9(b). The signal-to-background ratio is larger than 40dB. By adjusting the wave plates, we increased the output coupling ratio and consequently increased the output power to 12 W. In this modelocking state, the output spectrum, shown in Fig. A-8(b), has only 6-nm FWHM bandwidth as a result of reduced intracavity power. This narrow spectrum

exhibits only slight modulation implying that the pulse experiences reduced self-phase modulation from propagating in the CCC fiber due to the higher output coupling ratio. The autocorrelation durations of the compressed pulses is 420 fs.

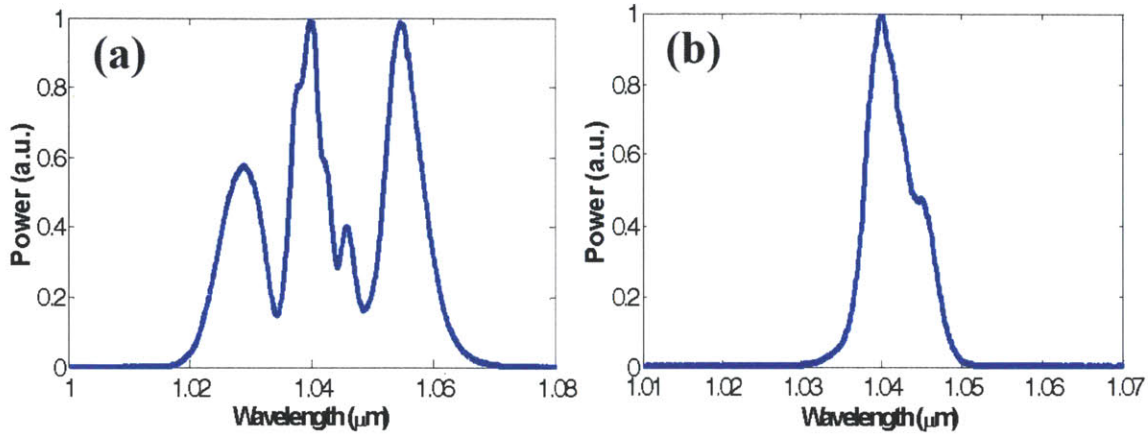

Fig. A-8. Optical spectra measured at NPE output of the oscillator operating at an output power of (a) 5W and (b) 12W.

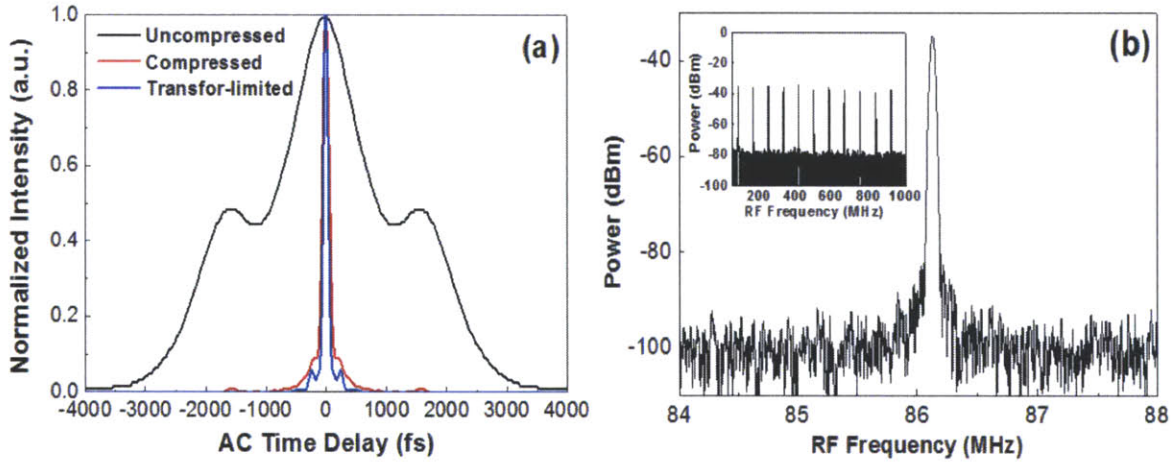

Fig. A-9. (a) Autocorrelation traces of the pulses. (b) Fundamental RF spectrum. Inset: Broadband RF spectrum.

In conclusion, we have demonstrated a high-energy femtosecond oscillator that incorporates an air-clad CCC Yb-fiber to ensure single-mode operation. Stable mode-locking is achieved using NPE together with a bandpass filter. The 300-fs mode-locked oscillator emits output power as high as 12W with 83-MHz repetition rate, corresponding to ~144-nJ pulse energy [27].

Appendix B

Modeling of Femtosecond Yb-Fiber Oscillators

B.1. Introduction

It is well known that compensation of group-velocity dispersion (GVD) in a fiber laser cavity is a prerequisite to generating femtosecond pulses. Most femtosecond fiber lasers have dispersion maps with optical segments of positive and negative GVD. The cavity's net GVD can be positive or negative. With large net negative GVD, soliton-like pulses can form due to the balance between negative GVD and positive nonlinearity (i.e., self-phase modulation). As the net GVD approaches zero, stretched-pulse operation occurs [110], which allows the intracavity pulse energy an order of magnitude higher than can be achieved in a soliton laser. Recently, Chong *et al.* [153] has reported another kind of mode-locked Yb fiber laser whose pulse shaping is dominated by spectral filtering of a highly-chirped intracavity pulse. The cavity contains no negative-GVD components. Different from soliton or stretched-pulse mode-locking, this all-normal-dispersion (ANDi) laser exhibits various pulse shapes and evolutions [154]. The pulse energy from an ANDi laser has been scaled to the 20 nJ level, and higher energies are possible.

To investigate the pulse dynamics in different mode-locking regimes, numerical simulation of the fiber oscillator is of particular importance. The theory behind mode-locked lasers has been well explored. For classical solid state and dye lasers advanced analytical theories exist; the master equation developed by Haus [155] has successfully modeled many types of mode-locked lasers. However, the mast equation linearizes the effect of cavity elements on the pulse, and thus is only adequate if these effects are weak in each round trip. In fiber lasers, however, this is not the case, and hence more advanced models based on numerical calculations have to be developed. The model used in this appendix is based on solving the NLSE numerically [156].

In this appendix, numerical simulation of the mode-locked Yb-fiber oscillator is presented using a rigorous, distributed model. Intracavity elements, such as gain fiber, passive fiber, saturable absorber, and dispersion compensation optics, are treated separately; the pulse propagation inside fibers is modeled by NLSE solved by the split-step Fourier method. Implemented using the fourth-order Runge-Kutta method in the interaction picture, the simulation provides an accuracy of $O(h^4)$ at less numerical expense. An adaptive step size algorithm (known as phase rotation method) is used to reduce the computation time. This model enables us to explore three different mode-locking regimes: 1) the stretched-pulse regime near zero net-dispersion, 2) the self-similar regime, and 3) the all-normal dispersion regime. Unlike previous published work, the non-negligibly large third order dispersion from grating pair is also included.

B.2. Numerical Solution to the NLSE

Analytical solutions to the full Maxwell wave equation for a nonlinear optical system do not exist. Even numerically solving the wave equation becomes extremely difficult due to the large parameter space. The vector form of the wave equation is a four-dimensional (three spatial, one temporal), second-order partial differential equation. Thus, approximations based on propagation

conditions and experimental results are needed in order to solve an approximate scalar form of the wave equation, *i.e.* the NLSE:

$$\frac{\partial \mathrm{A}(\mathrm{z},\tau)}{\partial z} = -i\frac{\beta_2}{2}\frac{\partial^2 \mathrm{A}(\mathrm{z},\tau)}{\partial \tau^2} + \frac{\beta_3}{6}\frac{\partial^3 \mathrm{A}(\mathrm{z},\tau)}{\partial \tau^3} + i\gamma|A|^2 A + gA, \qquad (1)$$

where $A(z,\tau)$ is slow varying electric field envelope, z the propagation distance, τ the time in the moving frame of the pulse, and γ the nonlinear parameter. The dispersion and nonlinear coefficients of single-mode fiber (SMF) used in the simulation are $\beta_2 = 23$ fs^2 /cm, $\beta_3 = 30$ fs^3 /m, and $\gamma = 0.0047$ (Wm)$^{-1}$, respectively. $g_{E\text{pulse}}$ denotes the net gain function for the Yb-doped gain fiber. The pulse energy is given by $E_{\text{pulse}} = \int_{-T_R/2}^{T_R/2} |A(z,\tau)|^2 d\tau$ where T_R is the cavity round-trip time. Gain saturation is modeled according to $g_{E\text{pulse}} = g_o(1 + E_{\text{pulse}}/E_{\text{sat}})$, where g_o corresponds to small-signal gain (2~6 m^{-1} assumed). The gain is introduced in the frequency domain and has a Lorentzian line-shape of 40-nm bandwidth centered at 1030nm. The gain saturation energy E_{sat} is set according to the pump power. In the simulation, E_{sat} varies from 0.3 to 3 nJ. In this modeling, we neglect self-steepening and stimulated Raman scattering in the NLSE.

B.2.1 Fourth-order Runge-Kutta Method in the Interaction Picture

NLSE is often solved using the split-step Fourier method (SSFM) [62], in which dispersive and nonlinear effects are separately integrated, and the results are combined to construct the full solution. The dispersive term is evaluated in the frequency domain through the use of the fast Fourier transform (FFT), while the nonlinear term is treated in the time domain. It is also possible to construct higher order split-step schemes such as the fourth-order scheme of Blow and Wood [157].

In general, global accuracy cannot exceed the accuracy of the method that is used to integrate the nonlinear step. For this purpose, Runge–Kutta or implicit schemes are normally used. A highly efficient and accurate algorithm, called the fourth-order Runge–Kutta in the interaction picture (RK4IP) method [62], has been developed to solve the Gross–Pitaevskii equation. RK4IP method has successfully been implemented to numerically study nonlinear phenomena arising from Bose–Einstein condensates. Closely related to the SSFM, RK4IP method transforms the problem into the interaction picture, which allows using conventional explicit techniques to step the solution forward. A higher efficiency is achieved by combining a fourth-order Runge–Kutta technique for stepping, with an appropriate choice of separation between the normal and interaction pictures. Memory efficient and easy to implement, the method exhibits fourth-order global accuracy. The RK4IP algorithm has a local error of fifth-order $O(h^5)$ and, thus, is a globally fourth-order accurate method $O(h^4)$. In this appendix, we use the RK4IP algorithm rather than SSFM to solve the NLSE to achieve higher accuracy.

B.2.2 Adaptive Method

For the SSFM or RK4IP method, the time-domain resolution is selected according to the maximum bandwidth of the signal during propagation, and the available discretization bins that are limited by the memory of the computer and the acceptable computational time. The time domain resolution therefore depends on the properties of signal and computer, and is fixed during the simulation. The longitudinal step size, however, does not have to be constant. If nonlinearities are low, the step size can be increased because the error in splitting dispersive and nonlinear processes is negligible. If both dispersion and nonlinearity are significant, a smaller step size is required. Since the balance between dispersion and nonlinearity can change during propagation due to decreasing peak power and broadening of the pulse, an algorithm is required to estimate the

current local error and to adapt accordingly. Since there is no mathematical restriction on the step-size h for the SSFM or RK4IP, keeping h very small would produce high accuracy at the cost of more computation time. Furthermore, choosing h smaller than the carrier wavelength λ_0 is physically meaningless, since the carrier frequency term in $A(t,\tau)$ is dropped in the derivation of the NLSE. On the other hand, choosing h to be too large imposes an artificial loss to the simulated system.

To optimize computational speed and achieve higher accuracy compared to the fixed step-size method, an efficient adaptive step-size method (called nonlinear phase-rotation method [158]) is employed. The nonlinear phase-rotation method is a variable step-size method designed for systems in which nonlinearity plays a major role. Within one simulation step, the effect of the nonlinear operator increases the phase shift. An upper limit on the nonlinear phase increment imposes bound on the step size, $h \le \frac{\phi_{NL}^{\max}}{\gamma |u|^2}$. Originally applied to simulate soliton propagation, this criterion for selecting the step size is widely used in optical-fiber transmission simulators.

B.3. Modeling of a Yb-fiber Oscillator Configured in a Ring Cavity

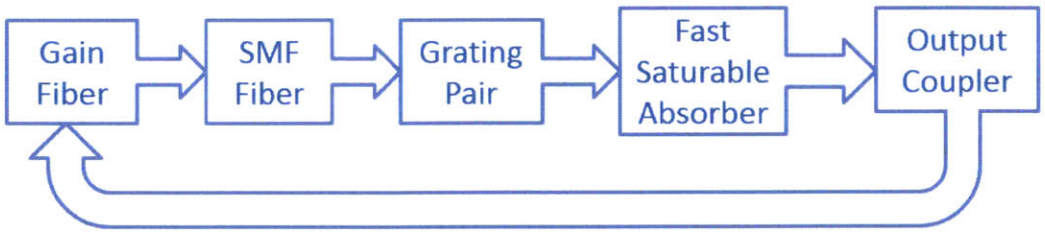

Fig. B-1. Illustration of the fiber laser ring cavity elements used for the simulations.

Our fiber oscillator model is based on iteratively simulating each part of the oscillator separately by solving the NLSE (Eq. 1) [154]. The simulation flow is shown in Fig. B-1. The NLSE describes the temporal and longitudinal dependence of the slowly varying (complex) pulse

envelope $A(z,\tau)$ along each nonlinear dispersive element (e.g. the fiber segments). For the gain fiber, the frequency dependent $g(\omega)$ is evaluated by a multiplication in the frequency domain. Similar to the cavity described in the paper of Ilday et.al. [110], the saturable absorber is approximated with an infinitely fast response time, which is appropriate for any absorber based on the Kerr effect (Kerr lens or nonlinear polarization rotation). The ideal saturable absorber is modeled with monotonically increasing transmission $T=1-l_o/[1+P(\tau)/P_{sat}]$ where $l_o=0.5$ is the unsaturated loss, $P(\tau)$ is the instantaneous pulse power, and P_{sat} is the saturation power. Details of the mode-locked spectrum can be changed by choosing different P_{sat} but overall characteristics do not change substantially. Once the transmission function deviates severely from the ideal one (e.g., the sinusoidal transmission curve of nonlinear polarization evolution) the simulation starts to show dramatically different results. We remove the detailed effects of the saturable absorber, in order to focus on other parameters. To this end, P_{sat} is adjusted within the range (0.05–13 kW) according to the pulse energy, so that the same pulse shape but with different peak powers experience the same point on the saturable absorber transmission curve.

The losses and output coupling are accounted a 50% loss after the saturable absorber mirror (SAM). The remaining power propagates through a dispersion compensation stage before entering the single mode fiber, which closes the loop. Figure B-1 illustrates the cavity configuration with all the simulation parameters similar to those used in Ref. [159].

The net cavity dispersion is calculated by $GDD_{net}=ß_{2Gain}\cdot L_{Gain}+ß_{2SMF}\cdot L_{SMF}+ GDD_{grating}$, where $GDD_{grating}$ is group delay dispersion induced by the grating pair which we employ as the dispersion delay line (DDL). In the simulation, we can adjust GDD_{net} by tuning $GDD_{grating}$; that is, the separation between the grating pair is adjusted. Each grating has a fixed groove period of 600 mm^{-1} and the light beam is incident at 45°. In the simulations, a pulse is iterated over many

round trips until a steady solution is reached. The convergence is evaluated by the relative change

ε in the N^{th} round-trip, $\varepsilon = \dfrac{\sum_i \left|A^N\right|^2 - \sum_i \left|A^{N-1}\right|^2}{\sum_i \left|A^{N-1}\right|^2}$, where A_i is the complex field amplitude. Three

different mode-locking regimes of an 80-MHz Yb-fiber ring lasers are investigated, i.e., the stretched-pulse regime near zero net-dispersion, the self-similar regime, and the all-normal dispersion regime.

B.4. Simulation of an Yb-fiber Oscillator in Three Different Regimes

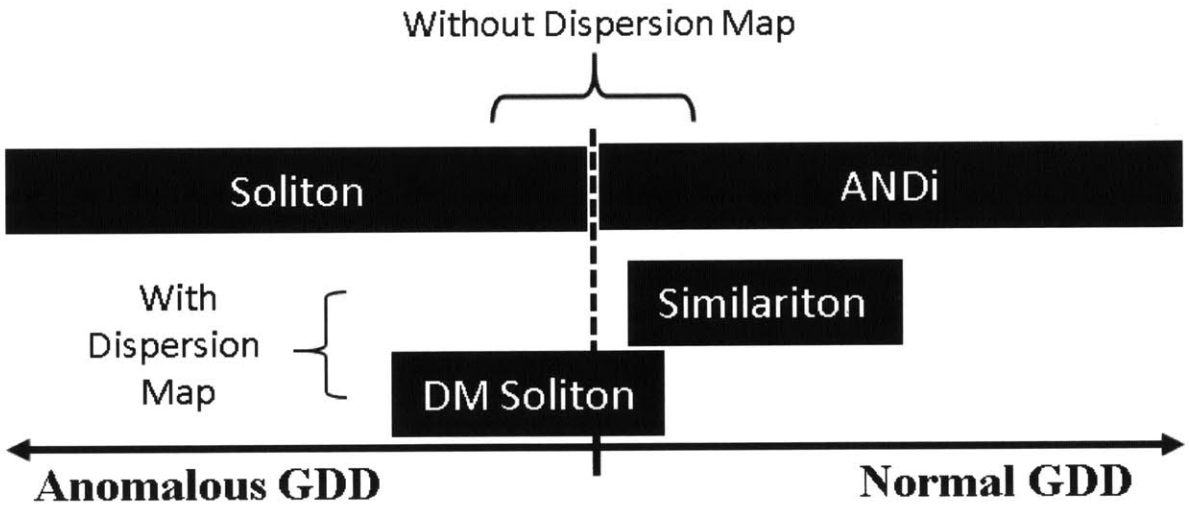

Fig. B-2. Operating mode-locked regimes according to the dispersion map.

To clarify the three regimes that we are going to simulate and investigate, the classification of four main mode-locking regimes is summarized in Fig. B-2 according to the net cavity GVD [109]. Clearly, soliton mode-locking occurs for a cavity that consists of only negative-GVD elements. With a dispersion map, the solutions are generally dispersion-managed (DM) solitons. For large net anomalous GVD, the pulses approximate static solitons, but as the net GVD approaches zero the solutions breathe. These regimes are based on some balance of negative GVD and positive nonlinearity. DM solitons can even exist at small net positive GVD. In soliton-like

pulse shaping, self-amplitude modulations mostly play a secondary role, namely starting and stabilizing the mode locking. As the net cavity GVD changes sign from negative to positive, different pulse-shaping mechanisms take over. With a dispersion map, self-similar operation can appear. Finally, stable pulse shaping can occur in an ANDi laser cavity comprised of only positive-GVD components.

Since single-mode Yb-doped fiber exhibits positive GVD, we will focus on simulating three mode-locking regimes (DM soliton, similariton, and ANDi laser) to explore energy scalability.

B.4.1 Stretched-pulse Regime ($GDD_{net} = -0.025$ ps^2)

The parameters of numerical simulation are listed in Table B-1. The grating pair has a separation of 6 cm, which leads to the net cavity GDD of −0.025 ps^2. The initial Gaussian pulse with 1-ps duration is sent to the laser cavity and iteratively propagates until the pulse converges.

Table B-1. Parameters of simulating DM soliton.

Gain Fiber	SMF	Grating	FSA	OC
L = 0.6 m g = 2/m γ = 0.0047 (Wm)$^{-1}$ E_{sat} = 0.3 nJ	L = 2 m γ = 0.0047 (Wm)$^{-1}$ E_{sat} = 0.3 nJ	$\theta_i = 45^\circ$ Λ = 600 mm^{-1} L_{sep} = 6 cm	L_0 = 50% P_{sat} = 100 W	T_0 = 50%

As we can see in Fig. B-3, the initial 1-ps Gaussian pulse converges to the steady state after many round trips. Figure B-4 shows the number of roundtrips (N) before the pulse converges. It also shows that the steady state solution has a soliton-like shape in both spectral and temporal domain which indicates that the oscillator operates in the DM soliton regime.

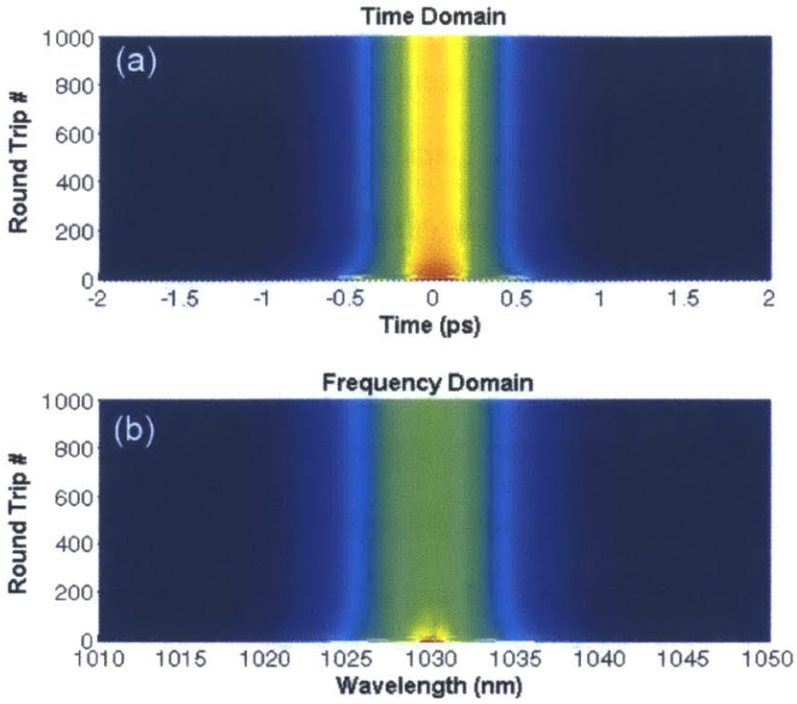

Fig. B-3. The convergence of the DM soliton to the initial condition in (a) the time domain and (b) the spectrum domain.

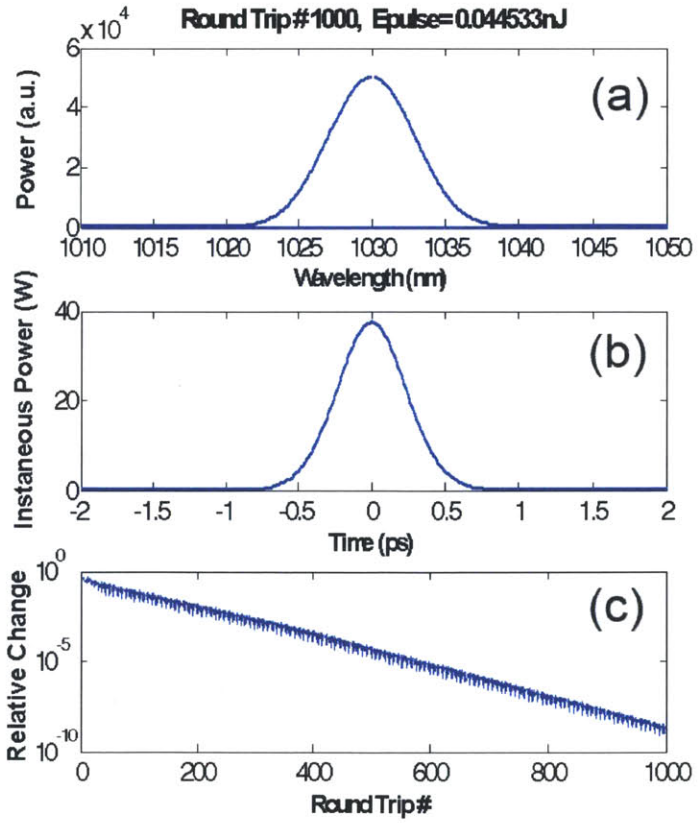

Fig. B-4. (a) The spectral shape and (b) the temporal shape of DM soliton at the output coupler. (c) The convergence with respect to the round-trip number.

For the stretched-pulse mode-locking, the intracavity pulse duration experiences a large change in a round trip, which effectively reduces the pulse peak power, and thus facilitates the generation of higher pulse energies. The intracavity pulse is stretched and compressed twice in each cavity round-trip; it reaches minimum duration in the middle of each segment and acquires both signs of chirp [160]. To prove this phenomenon, we further simulate the pulse dynamics in the cavity. As shown in Fig. B-5, the pulse does breathe twice during each round trip. The pulse before the grating pair is originally of positive chirp. After the compression from the grating pair, it becomes negatively chirped. As the pulse propagates through the fiber, it is compressed and then dispersed again by the fiber's normal dispersion. It is noteworthy that the pulse is asymmetric along the cavity, caused by the third order dispersion (TOD) of 862800 fs^3 mainly from the grating pair. In the literature, the grating-pair's TOD is normally neglected; consequently, the pulse possesses a symmetric temporal and spectral profile.

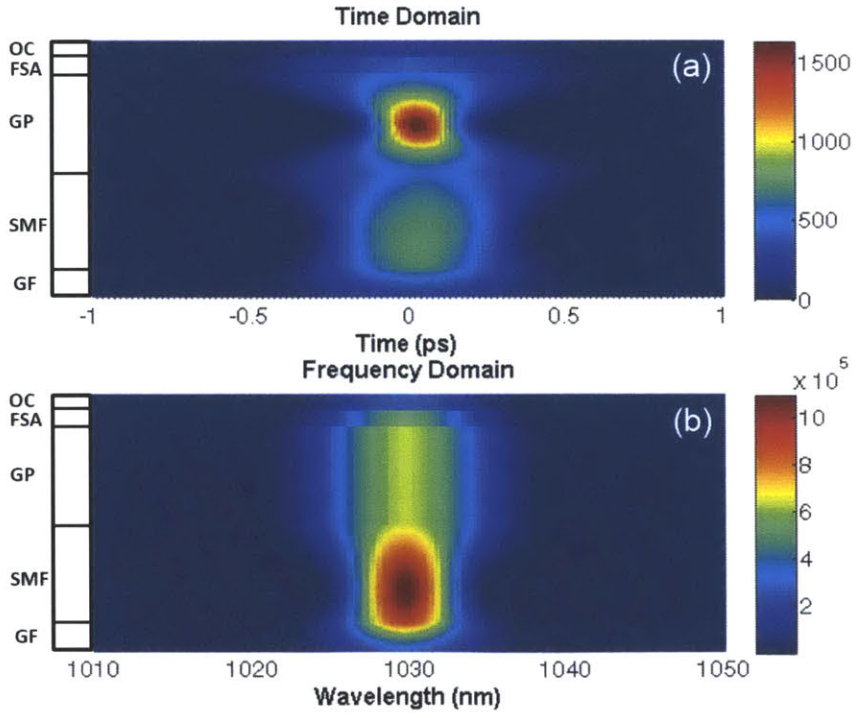

Fig. B-5. The pulse propagation dynamics in the cavity in the stretched pulse regime. GF: gain fiber; SMF: single mode fiber; OC: output coupler; GP: grating pair; FSA: fast saturable absorber.

B.4.2 Self-similar Regime (GDD_{net} = +0.025 ps^2)

To achieve higher pulse energy, we can adjust the net GDD to be positive and set the mode-locking state in the self-similar regime. The simulation parameters are listed in Table B-2. The grating pair has a separation of 2.5-cm, which leads to net cavity GDD of 0.025 ps^2.

Table B-2. Parameters of simulating similariton.

Gain Fiber	SMF	Grating	FSA	OC
L = 0.6 m g = 2/m $\gamma = 0.0023\ (Wm)^{-1}$ E_{sat} = 3 nJ	L = 2 m $\gamma = 0.0023\ (Wm)^{-1}$ E_{sat} = 3 nJ	$\theta_i = 45^\circ$ $\Lambda = 600\ mm^{-1}$ L_{sep} = 2.5 cm	L_0 = 50% P_{sat} = 500 W	T_0 = 50%

Figure B-6 shows the number of roundtrips (N) before the convergence and the steady state solution has a parabolic shape in the frequency domain, which indicates that the oscillator operates in the self-similar regime.

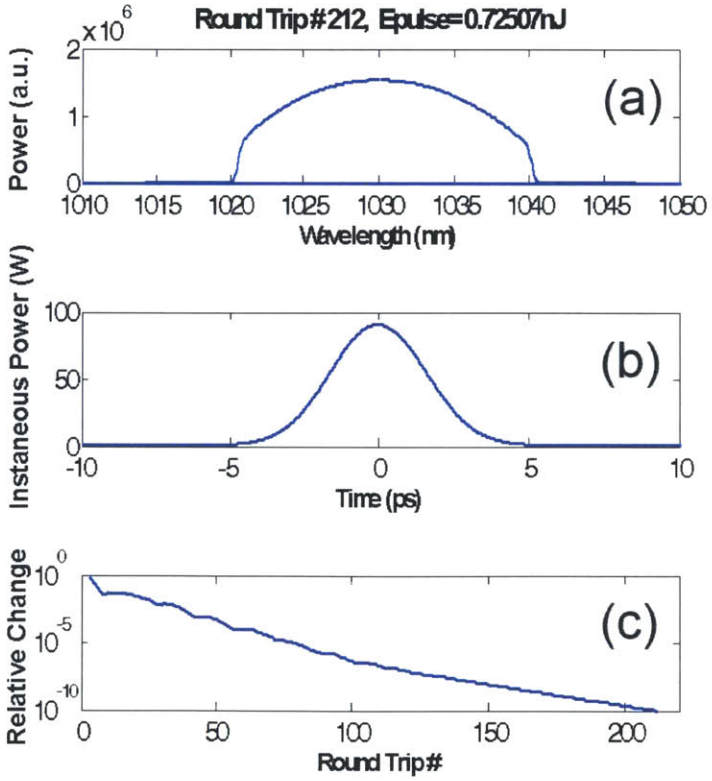

Fig. B-6. (a) The spectral shape and (b) the temporal shape of the similariton at the output coupler. (c) The convergence with respect to the round-trip number.

The main feature of the self-similar evolution for the intracavity pulse is that the pulse duration evolves monotonously in the active fiber and its spectrum approaches a parabolic shape. The finite gain bandwidth of the Yb-fiber ultimately limits the self-similar evolution, preventing further energy scaling [68,69,161]. To explore this phenomenon, we also simulate the pulse dynamics in the cavity in Fig. B-7. The pulse only stretches in the fiber. The pulse before the grating pair has a positive chirp. After the compression of the grating pair, it is still positively chirped. Besides, the pulse evolves almost symmetrically despite the existence of net TOD of 132,500 fs^3.

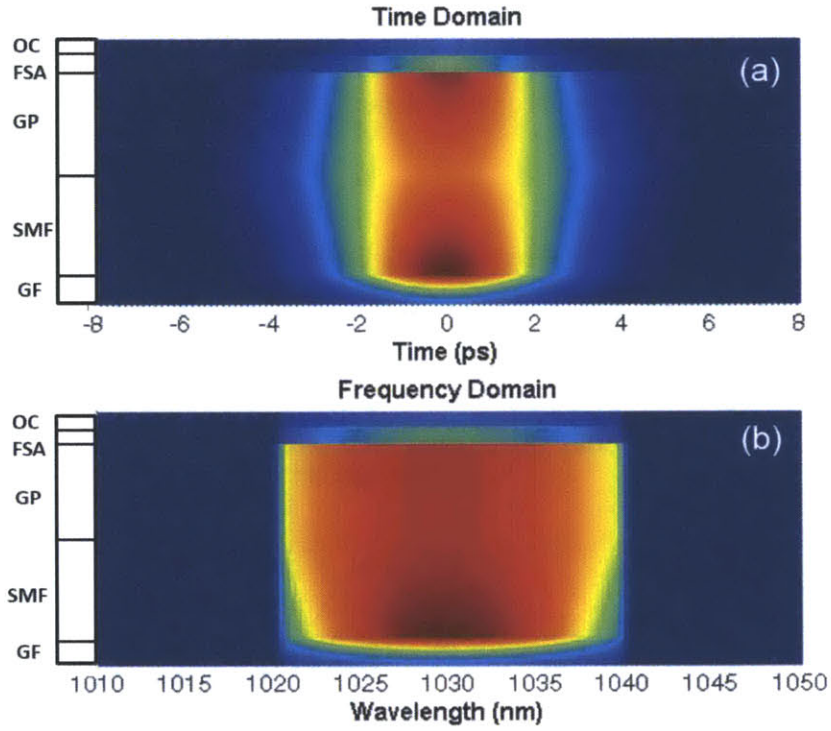

Fig. B-7. The pulse propagation dynamics in the cavity in the time and frequency domain. GF: gain fiber; SMF: single mode fiber; OC: output coupler; GP: grating pair; FSA: fast saturable absorber.

B.4.3 All-normal Dispersion Regime (GDD_{net} = +0.06 ps^2)

To further achieve higher intracavity pulse energy, the negative GVD segment should be removed and replaced by a spectral filter, resulting in an all–normal-dispersion (ANDi) oscillator.

Pulse shaping inside ANDi fiber oscillators relies on intracavity spectral filtering of the highly chirped intracavity pulse, which cuts off the temporal wings of the pulse. The new illustration of the ring cavity is shown in Fig. B-8, with simulation parameters listed in Table B-3. Here, the grating pair is replaced by a Gaussian spectral filter with 10-nm bandwidth centered at 1030 nm. The intracavity cavity dispersion in this case is +0.06 ps^2. The initial 1-ps Gaussian pulse is sent to the laser cavity and iteratively propagates until the pulse converges.

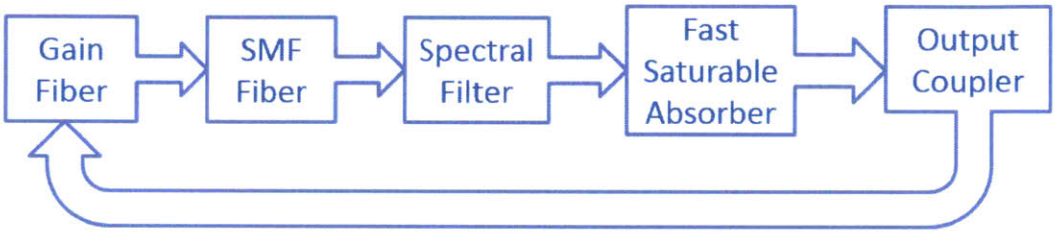

Fig. B-8. Simulation flow of an ANDi oscillator.

Table B-3. Parameters of simulating an ANDi oscillator.

Gain Fiber	SMF	Spectral Filter	FSA	OC
L = 0.6 m g = 6.9/m $\gamma = 0.0047\ (Wm)^{-1}$ $E_{sat} = 3$ nJ	L = 2 m $\gamma = 0.0047\ (Wm)^{-1}$ $E_{sat} = 3$ nJ	FWHM = 10 nm centered at 1030 nm	$L_0 = 50\%$ $P_{sat} = 50$ W	$T_0 = 10\%$

Figure B-9 shows the number of roundtrips (N) before the convergence. In the spectral domain, we can see side lobes on the wings develop. The main characteristic operation of ANDi lasers is the spectral filtering of the chirped intracavity pulse, and the development of spectral spikes as the pulse propagates inside the fiber [162]. To investigate this phenomenon, we also simulate the pulse dynamics in the ANDi laser. As shown in Fig. B-10, pulse stretches monotonically in the fiber and becomes shortened by the spectral filter, which also narrows the pulse spectrum. This indicates that the pulse before the spectral filter is highly chirped. The spectral filter does have a strong pulse shaping mechanism. Therefore, the main pulse-shaping mechanism

of an ANDi fiber laser is sometimes described as chirped-pulse spectral filtering. As the pulse propagates along the fiber (Fig. B-10(b)), spikes grow up on the edge of the spectrum which is a characteristic of ANDi lasers. Despite the net TOD of 78,000 fs^3, the pulse evolves almost symmetrically.

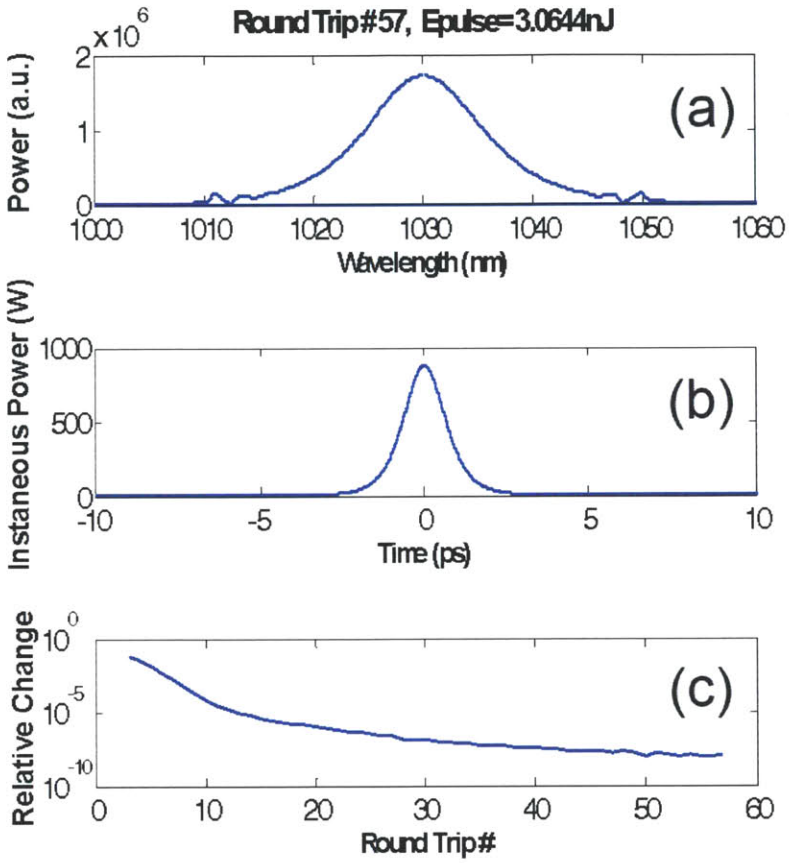

Fig. B-9. (a) The spectral shape and (b) the temporal shape of the ANDi laser at the output coupler. (c) The convergence with respect to the round-trip number.

Furthermore, comparing these three regimes reveals that the pulse energies of DM soliton, similariton, ANDi laser are 0.04 nJ, 0.72 nJ, and 3 nJ, respectively. It shows that ANDi lasers sustain the highest mode-locking pulse energy. However, it should be noted that although ANDi laser can produce relatively high energy pulse, the pulse quality after external GDD compression is poor and would have pedestals around. Usually, people who design

an ANDi laser will put an output coupler at the end of the single mode fiber to obtain high pulse energy. In this configuration, Fig. B-11(a) shows that the output is a 7-ps chirped pulse whose spectrum supports a transform-limited pulse of 60 fs in Fig. B-11(b). Clearly, the transform-limited pulse is of poor quality featuring noticeable pedestal. A pulse with better quality but lower energy can be achieved by taking the output at different positions of the cavity. This is clearly seen in Fig. B-11. If we take the output at OC rather than at SMF, the pulse spectrum is smoother but at the cost of losing pulse energy; the corresponding transform-limited pulse exhibits negligible pedestals.

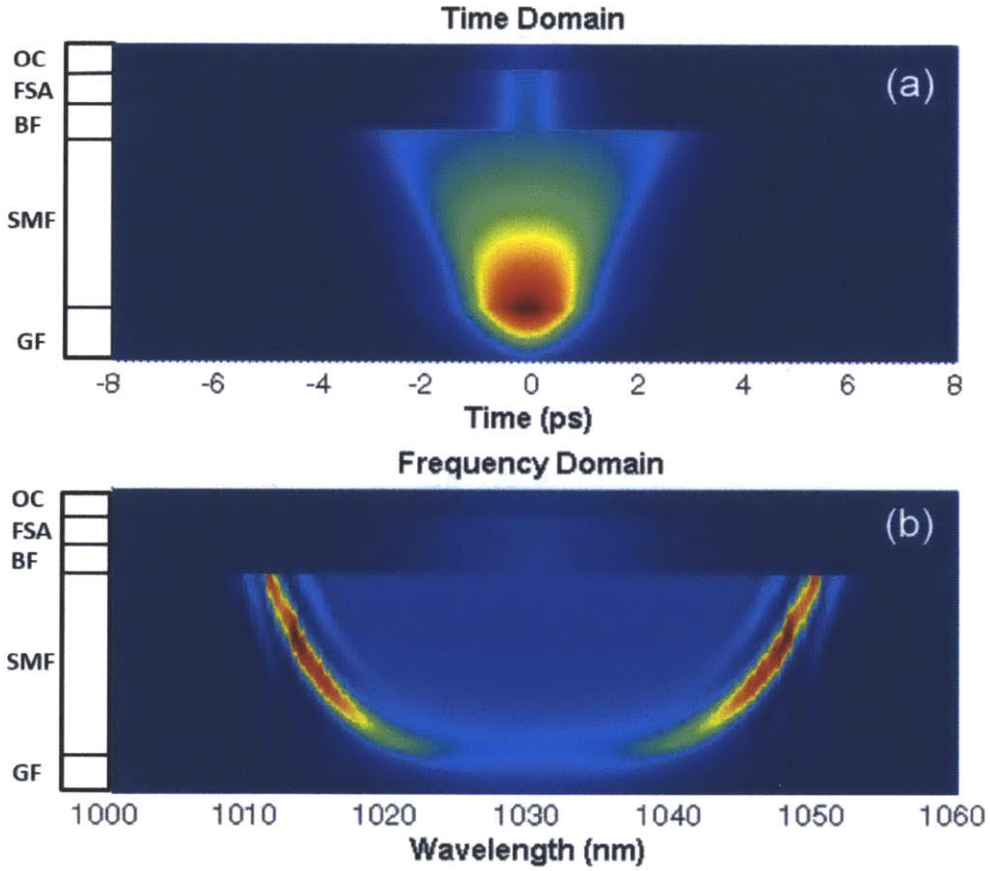

Fig. B-10. The pulse propagation dynamics in the ANDi laser in the time and frequency domain. GF: gain fiber; SMF: single mode fiber; BF: bandpass filter; OC: output coupler; FSA: fast saturable absorber.

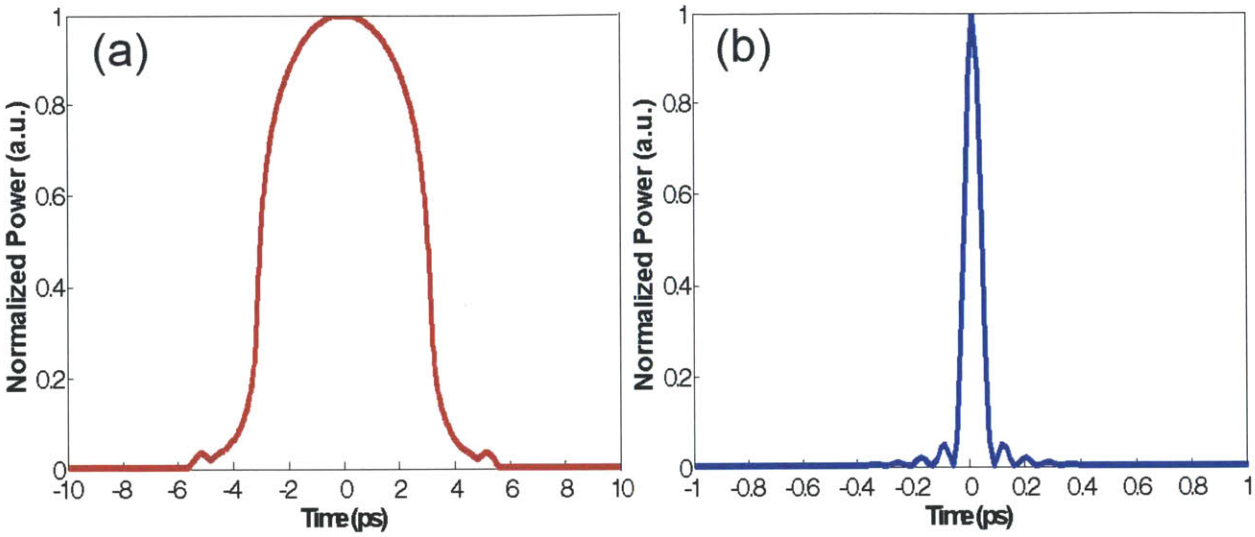

Fig. B-11. (a) The temporal pulse and (b) the transform-limited pulse at the end of the single mode fiber in the ANDi laser.

B.5. Conclusion

In this appendix, numerical simulations of the mode-locked Yb-fiber oscillator are presented using a rigorous, distributed model. We have introduced and numerically explored the characteristics in three different mode-locking regimes. The pulse dynamics inside the cavity is also studied. These numerical simulations reveal the physical mechanism for Yb-fiber oscillators. Future implementation can take into account cross-phase modulation, self-steepening, and stimulated Raman scattering to have a more accurate modeling when the pulse energy is higher.

Bibliography

1. B. R. Masters and P. T. C. So, *Handbook of Biomedical Nonlinear Optical Microscopy* (Oxford University Press, 2008).

2. N. Ji, J. C. Magee, and E. Betzig, "High-speed, low-photodamage nonlinear imaging using passive pulse splitters," Nat. Methods **5**, 197–202 (2008).

3. S.-W. Chu, T.-M. Liu, C.-K. Sun, C.-Y. Lin, and H.-J. Tsai, "Real-time second-harmonic-generation microscopy based on a 2-GHz repetition rate Ti:sapphire laser," Opt. Express **11**, 933 (2003).

4. E. Ippen, A. Benedick, J. Birge, H. Byun, L.-J. Chen, G. Chang, D. Chao, J. Morse, A. Motamedi, M. Sander, G. Petrich, L. Kolodziejski, and F. Kärtner, "Optical Arbitrary Waveform Generation," in *Conference on Lasers and Electro-Optics 2010*, OSA Technical Digest (CD) (Optical Society of America, 2010), p. JThC4.

5. S. Yoo, "Monolithically integrated optical arbitrary waveform generators by line-by-line amplitude and phase modulation," in *IEEE Lasers and Electro-Optics Society, 2008. LEOS 2008. 21st Annual Meeting of the* (2008), pp. 425–426.

6. S. T. Cundiff and A. M. Weiner, "Optical arbitrary waveform generation," Nat. Photonics **4**, 760–766 (2010).

7. S. A. Diddams, "The evolving optical frequency comb," J. Opt. Soc. Am. B **27**, B51–B62 (2010).

8. D. Huang, E. A. Swanson, C. P. Lin, J. S. Schuman, W. G. Stinson, W. Chang, M. R. Hee, T. Flotte, K. Gregory, C. A. Puliafito, and J. G. Fujimoto, "Optical coherence tomography," Science **254**, 1178–1181 (1991).

9. J. M. Schmitt, "Optical coherence tomography (OCT): a review," IEEE J. Sel. Top. Quantum Electron. **5**, 1205–1215 (1999).

10. J. G. Fujimoto, "Optical coherence tomography for ultrahigh resolution in vivo imaging," Nat. Biotechnol. **21**, 1361–1367 (2003).

11. J. A. Bell, M. C. Hamilton, D. A. Leep, T. D. Moran, H. F. Taylor, and Y.-H. Lee, "Extension of electronic A/D converters to multi-gigahertz sampling rates using optical sampling and demultiplexing techniques," **1**, 289– 293 (1989).

12. A. Yariv and R.G.M.P. Koumans, "Time interleaved optical sampling for ultra-high speed A/D conversion," Electron. Lett. **34**, 2012–2013 (1998).

13. A. Khilo, S. J. Spector, M. E. Grein, A. H. Nejadmalayeri, C. W. Holzwarth, M. Y. Sander, M. S. Dahlem, M. Y. Peng, M. W. Geis, N. A. DiLello, J. U. Yoon, A. Motamedi, J. S. Orcutt, J. P. Wang, C. M. Sorace-Agaskar, M. A. Popović, J. Sun, G.-R. Zhou, H. Byun, J. Chen, J. L. Hoyt, H. I. Smith, R. J. Ram, M. Perrott, T. M. Lyszczarz, E. P. Ippen, and F. X. Kärtner, "Photonic ADC: overcoming the bottleneck of electronic jitter," Opt. Express **20**, 4454–4469 (2012).

14. W. Denk, J. H. Strickler, and W. W. Webb, "Two-photon laser scanning fluorescence microscopy," Science **248**, 73–76 (1990).

15. R. Ell, U. Morgner, F. X. Kärtner, J. G. Fujimoto, E. P. Ippen, V. Scheuer, G. Angelow, T. Tschudi, M. J. Lederer, A. Boiko, and B. Luther-Davies, "Generation of 5-fs pulses and octave-spanning spectra directly from a Ti:sapphire laser," Opt. Lett. **26**, 373–375 (2001).

16. U. Morgner, F. X. Kärtner, S. H. Cho, Y. Chen, H. A. Haus, J. G. Fujimoto, E. P. Ippen, V. Scheuer, G. Angelow, and T. Tschudi, "Sub-two-cycle pulses from a Kerr-lens mode-locked Ti:sapphire laser," Opt. Lett. **24**, 411–413 (1999).

17. L.-J. Chen, A. J. Benedick, J. R. Birge, M. Y. Sander, and F. Kärtner, "Octave-spanning, dual-output 2.166 GHz Ti:sapphire laser," Opt. Express **16**, 20699–20705 (2008).

18. A. Seas, V. Petričević, and R. R. Alfano, "Generation of sub-100-fs pulses from a cw mode-locked chromium-doped forsterite laser," Opt. Lett. **17**, 937 (1992).

19. A. Seas, V. Petričević, and R. R. Alfano, "Self-mode-locked chromium-doped forsterite laser generates 50-fspulses," Opt. Lett. **18**, 891–893 (1993).

20. V. Yanovsky, B. I. Minkov, Y. Pang, and F. Wise, "Generation of 25-fs pulses from a self-mode-locked Cr:forsterite laser with optimized group-delay dispersion," Opt. Lett. **18**, 1541–1543 (1993).

21. H.-W. Chen, G. Chang, S. Xu, Z. Yang, and F. X. Kärtner, "3 GHz, fundamentally mode-locked, femtosecond Yb-fiber laser," Opt. Lett. **37**, 3522–3524 (2012).

22. H.-W. Chen, J. Lim, S.-W. Huang, D. N. Schimpf, F. X. Kärtner, and G. Chang, "Optimization of femtosecond Yb-doped fiber amplifiers for high-quality pulse compression," Opt. Express **20**, 28672–28682 (2012).

23. J. Lim, H.-W. Chen, G. Chang, and F. X. Kärtner, "Frequency comb based on a narrowband Yb-fiber oscillator: pre-chirp management for self-referenced carrier envelope offset frequency stabilization," Opt. Express **21**, 4531–4538 (2013).

24. H.-W. Chen, Z. Haider, J. Lim, S. Xu, Z. Yang, F. X. Kärtner, and G. Chang, "3 GHz, Yb-fiber laser-based, few-cycle ultrafast source at the Ti:sapphire laser wavelength," Opt. Lett. **38**, 4927–4930 (2013).

25. J. Lim, H.-W. Chen, S. Xu, Z. Yang, G. Chang, and F. X. Kärtner, "3 GHz, watt-level femtosecond Raman soliton source," Opt. Lett. **39**, 2060–2063 (2014).

26. H.-W. Chen, T. Sosnowski, C.-H. Liu, L.-J. Chen, J. R. Birge, A. Galvanauskas, F. X. Kärtner, and G. Chang, "Chirally-coupled-core Yb-fiber laser delivering 80-fs pulses with diffraction-limited beam quality warranted by a high-dispersion mirror based compressor," Opt. Express **18**, 24699–24705 (2010).

27. H.-W. Chen, G. Chang, C. Zhu, X. Ma, A. Galvanauskas, and F. X. Kärtner, "Air-clad chirally-coupled-core Yb-fiber femtosecond oscillator with >10W average power," EPJ Web Conf. **41**, 10006 (2013).

28. C.-H. Li, A. J. Benedick, P. Fendel, A. G. Glenday, F. X. Kärtner, D. F. Phillips, D. Sasselov, A. Szentgyorgyi, and R. L. Walsworth, "A laser frequency comb that enables radial velocity measurements with a precision of 1 cm s-1," Nature **452**, 610–612 (2008).

29. T. Steinmetz, T. Wilken, C. Araujo-Hauck, R. Holzwarth, T. W. Hänsch, L. Pasquini, A. Manescau, S. D'Odorico, M. T. Murphy, T. Kentischer, W. Schmidt, and T. Udem, "Laser Frequency Combs for Astronomical Observations," Science **321**, 1335–1337 (2008).

30. D. A. Braje, M. S. Kirchner, S. Osterman, T. Fortier, and S. A. Diddams, "Astronomical spectrograph calibration with broad-spectrum frequency combs," Eur. Phys. J. D **48**, 57–66 (2008).

31. G. Chang, C.-H. Li, D. F. Phillips, R. L. Walsworth, and F. X. Kärtner, "Toward a broadband astro-comb: effects of nonlinear spectral broadening in optical fibers," Opt. Express **18**, 12736–12747 (2010).

32. T. Wilken, G. L. Curto, R. A. Probst, T. Steinmetz, A. Manescau, L. Pasquini, J. I. G. Hernández, R. Rebolo, T. W. Hänsch, T. Udem, and R. Holzwarth, "A spectrograph for exoplanet observations calibrated at the centimetre-per-second level," Nature **485**, 611–614 (2012).

33. G. G. Ycas, F. Quinlan, S. A. Diddams, S. Osterman, S. Mahadevan, S. Redman, R. Terrien, L. Ramsey, C. F. Bender, B. Botzer, and S. Sigurdsson, "Demonstration of on-sky calibration of astronomical spectra using a 25 GHz near-IR laser frequency comb," Opt. Express **20**, 6631–6643 (2012).

34. A. Bartels, D. Heinecke, and S. A. Diddams, "10-GHz Self-Referenced Optical Frequency Comb," Science **326**, 681–681 (2009).

35. D. Li, U. Demirbas, J. R. Birge, G. S. Petrich, L. A. Kolodziejski, A. Sennaroglu, F. X. Kärtner, and J. G. Fujimoto, "Diode-pumped passively mode-locked GHz femtosecond Cr:LiSAF laser with kW peak power," Opt. Lett. **35**, 1446–1448 (2010).

36. S. Yamazoe, M. Katou, T. Adachi, and T. Kasamatsu, "Palm-top-size, 1.5 kW peak-power, and femtosecond (160 fs) diode-pumped mode-locked Yb^{+3}:$KY(WO_4)_2$ solid-state laser with a semiconductor saturable absorber mirror," Opt. Lett. **35**, 748–750 (2010).

37. S. Pekarek, A. Klenner, T. Südmeyer, C. Fiebig, K. Paschke, G. Erbert, and U. Keller, "Femtosecond diode-pumped solid-state laser with a repetition rate of 4.8 GHz," Opt. Express **20**, 4248–4253 (2012).

38. J. Chen, J. W. Sickler, H. Byun, E. P. Ippen, S. Jiang, and F. X. Kärtner, "Fundamentally Mode-locked 3 GHz Femtosecond Erbium Fiber Laser," in *Ultrafast Phenomena XVI*, P. Corkum, S. Silvestri, K. A. Nelson, E. Riedle, R. W. Schoenlein, F. P. Schäfer, J. P. Toennies, and W. Zinth, eds., Springer Series in Chemical Physics (Springer Berlin Heidelberg, 2009), Vol. 92, pp. 732–734.

39. I. Hartl, H. A. Mckay, R. Thapa, B. K. Thomas, L. Dong, and M. E. Fermann, "GHz Yb-Femtosecond-Fiber Laser Frequency Comb," in *Conference on Lasers and Electro-Optics/International Quantum Electronics Conference*, OSA Technical Digest (CD) (Optical Society of America, 2009), p. CMN1.

40. D. Chao, M. Sander, G. Chang, J. Morse, J. Cox, G. Petrich, L. Kolodziejski, F. Kärtner, and E. Ippen, "Self-referenced Erbium Fiber Laser Frequency Comb at a GHz Repetition Rate," in *Optical Fiber Communication Conference*, OSA Technical Digest (Optical Society of America, 2012), p. OW1C.2.

41. A. Ruehl, A. Marcinkevicius, M. E. Fermann, and I. Hartl, "80 W, 120 fs Yb-fiber frequency comb," Opt. Lett. **35**, 3015–3017 (2010).

42. D. Pudo, H. Byun, J. Chen, J. Sickler, F. X. Kärtner, and E. P. Ippen, "Scaling of passively mode-locked soliton erbium waveguide lasers based on slow saturable absorbers," Opt. Express **16**, 19221–19231 (2008).

43. I. Hartl, A. Romann, and M. E. Fermann, "Passively mode locked GHz femtosecond Yb-fiber laser using an intra-cavity Martinez compressor," in *Lasers and Electro-Optics (CLEO), 2011 Conference on* (2011), pp. 1 –2.

44. S. H. Xu, Z. M. Yang, T. Liu, W. N. Zhang, Z. M. Feng, Q. Y. Zhang, and Z. H. Jiang, "An efficient compact 300 mW narrow-linewidth single frequency fiber laser at 1.5 μm," Opt. Express **18**, 1249–1254 (2010).

45. J. Thévenin, M. Vallet, and M. Brunel, "Dual-polarization mode-locked Nd:YAG laser," Opt. Lett. **37**, 2859–2861 (2012).

46. B. C. Collings, S. T. Cundiff, N. N. Akhmediev, J. M. Soto-Crespo, K. Bergman, and W. H. Knox, "Polarization-locked temporal vector solitons in a fiber laser: experiment," J. Opt. Soc. Am. B **17**, 354–365 (2000).

47. S. T. Cundiff, B. C. Collings, and K. Bergman, "Polarization locked vector solitons and axis instability in optical fiber," Chaos Interdiscip. J. Nonlinear Sci. **10**, 613–624 (2000).

48. C. Mou, S. Sergeyev, A. Rozhin, and S. Turistyn, "All-fiber polarization locked vector soliton laser using carbon nanotubes," Opt. Lett. **36**, 3831–3833 (2011).

49. S. V. Sergeyev, C. Mou, A. Rozhin, and S. K. Turitsyn, "Vector solitons with locked and precessing states of polarization," Opt. Express **20**, 27434–27440 (2012).

50. Y. F. Song, H. Zhang, D. Y. Tang, and D. Y. Shen, "Polarization rotation vector solitons in a graphene mode-locked fiber laser," Opt. Express **20**, 27283–27289 (2012).

51. D. Y. Tang, H. Zhang, L. M. Zhao, and X. Wu, "Observation of High-Order Polarization-Locked Vector Solitons in a Fiber Laser," Phys. Rev. Lett. **101**, 153904 (2008).

52. D. Strickland and G. Mourou, "Compression of amplified chirped optical pulses," Opt. Commun. **55**, 447–449 (1985).

53. A. Galvanauskas, "Mode-scalable fiber-based chirped pulse amplification systems," IEEE J. Sel. Top. Quantum Electron. **7**, 504 –517 (2001).

54. R. Paschotta, J. Nilsson, A. C. Tropper, and D. C. Hanna, "Ytterbium-doped fiber amplifiers," IEEE J. Quantum Electron. **33**, 1049 –1056 (1997).

55. M. Oberthaler and R. A. Höpfel, "Special narrowing of ultrashort laser pulses by self-phase modulation in optical fibers," Appl. Phys. Lett. **63**, 1017–1019 (1993).

56. J. Limpert, T. Gabler, A. Liem, H. Zellmer, and A. Tünnermann, "SPM-induced spectral compression of picosecond pulses in a single-mode Yb-doped fiber amplifier," Appl. Phys. B Lasers Opt. **74**, 191–195 (2002).

48. C. R. Giles and E. Desurvire, "Propagation of signal and noise in concatenated erbium-doped fiber optical amplifiers," J. Light. Technol. **9**, 147 –154 (1991).

58. C. R. Giles and E. Desurvire, "Modeling erbium-doped fiber amplifiers," J. Light. Technol. **9**, 271–283 (1991).

59. F. He, J. H. Price, K. T. Vu, A. Malinowski, J. K. Sahu, and D. J. Richardson, "Optimisation of cascaded Yb fiber amplifier chains using numerical-modelling," Opt. Express **14**, 12846–12858 (2006).

60. G. Agrawal, *Nonlinear Fiber Optics* (Academic Press, 2001).

61. T. J. Whitley and R. Wyatt, "Alternative Gaussian spot size polynomial for use with doped fiber amplifiers," IEEE Photonics Technol. Lett. **5**, 1325–1327 (1993).

53. J. Hult, "A Fourth-Order Runge–Kutta in the Interaction Picture Method for Simulating Supercontinuum Generation in Optical Fibers," J. Light. Technol. **25**, 3770–3775 (2007).

63. A. Heidt, "Efficient Adaptive Step Size Method for the Simulation of Supercontinuum Generation in Optical Fibers," J. Light. Technol. **27**, 3984–3991 (2009).

64. B. Ortaç, J. Limpert, and A. Tünnermann, "High-energy femtosecond Yb-doped fiber laser operating in the anomalous dispersion regime," Opt. Lett. **32**, 2149–2151 (2007).

65. M. E. Fermann, V. I. Kruglov, B. C. Thomsen, J. M. Dudley, and J. D. Harvey, "Self-Similar Propagation and Amplification of Parabolic Pulses in Optical Fibers," Phys. Rev. Lett. **84**, 6010–6013 (2000).

66. V. I. Kruglov, A. C. Peacock, J. D. Harvey, and J. M. Dudley, "Self-similar propagation of parabolic pulses in normal-dispersion fiber amplifiers," J. Opt. Soc. Am. B **19**, 461–469 (2002).

67. G. Chang, A. Galvanauskas, H. G. Winful, and T. B. Norris, "Dependence of parabolic pulse amplification on stimulated Raman scattering and gain bandwidth," Opt. Lett. **29**, 2647–2649 (2004).

68. D. B. Soh, J. Nilsson, and A. B. Grudinin, "Efficient femtosecond pulse generation using a parabolic amplifier combined with a pulse compressor. I. Stimulated Raman-scattering effects," J. Opt. Soc. Am. B **23**, 1–9 (2006).

69. D. B. Soh, J. Nilsson, and A. B. Grudinin, "Efficient femtosecond pulse generation using a parabolic amplifier combined with a pulse compressor. II. Finite gain-bandwidth effect," J. Opt. Soc. Am. B **23**, 10–19 (2006).

70. S. Pekarek, T. Südmeyer, S. Lecomte, S. Kundermann, J. M. Dudley, and U. Keller, "Self-referenceable frequency comb from a gigahertz diode-pumped solid-state laser," Opt. Express **19**, 16491–16497 (2011).

71. I. Hartl, H. A. McKay, R. Thapa, B. K. Thomas, A. Ruehl, L. Dong, and M. E. Fermann, "GHz Yb-Fiber Laser Frequency Comb for Spectroscopy Applications," in *Advances in Imaging*, OSA Technical Digest (CD) (Optical Society of America, 2009), p. FMB3.

72. T. C. Schratwieser, C. G. Leburn, and D. T. Reid, "Highly efficient 1 GHz repetition-frequency femtosecond Yb^{3+}:$KY(WO_4)_2$ laser," Opt. Lett. **37**, 1133–1135 (2012).

73. M. Endo, A. Ozawa, and Y. Kobayashi, "Kerr-lens mode-locked Yb:KYW laser at 4.6-GHz repetition rate," Opt. Express **20**, 12191–12197 (2012).

74. A. Choudhary, A. A. Lagatsky, P. Kannan, W. Sibbett, C. T. A. Brown, and D. P. Shepherd, "Diode-pumped femtosecond solid-state waveguide laser with a 4.9 GHz pulse repetition rate," Opt. Lett. **37**, 4416–4418 (2012).

75. A. A. Lagatsky, A. Choudhary, P. Kannan, D. P. Shepherd, W. Sibbett, and C. T. A. Brown, "Fundamentally mode-locked, femtosecond waveguide oscillators with multi-gigahertz repetition frequencies up to 15 GHz," Opt. Express **21**, 19608–19614 (2013).

76. S. Pekarek, M. C. Stumpf, S. Lecomte, S. Kundermann, A. Klenner, T. Südmeyer, J. M. Dudley, and U. Keller, "Compact Gigahertz Frequency Comb Generation: How Short Do The Pulses Need To Be?," in *Lasers, Sources, and Related Photonic Devices*, OSA Technical Digest (CD) (Optical Society of America, 2012), p. AT5A.2.

77. S. Koke, C. Grebing, H. Frei, A. Anderson, A. Assion, and G. Steinmeyer, "Direct frequency comb synthesis with arbitrary offset and shot-noise-limited phase noise," Nat. Photonics **4**, 462–465 (2010).

78. A. L. Gaeta, "Nonlinear propagation and continuum generation in microstructured optical fibers," Opt. Lett. **27**, 924–926 (2002).

79. G. Chang, T. B. Norris, and H. G. Winful, "Optimization of supercontinuum generation in photonic crystal fibers for pulse compression," Opt. Lett. **28**, 546–548 (2003).

80. K. L. Corwin, N. R. Newbury, J. M. Dudley, S. Coen, S. A. Diddams, K. Weber, and R. S. Windeler, "Fundamental Noise Limitations to Supercontinuum Generation in Microstructure Fiber," Phys. Rev. Lett. **90**, 113904 (2003).

81. R. Paschotta, "Timing jitter and phase noise of mode-locked fiber lasers," Opt. Express **18**, 5041–5054 (2010).

82. C. Benko, A. Ruehl, M. J. Martin, K. S. E. Eikema, M. E. Fermann, I. Hartl, and J. Ye, "Full phase stabilization of a Yb:fiber femtosecond frequency comb via high-bandwidth transducers," Opt. Lett. **37**, 2196–2198 (2012).

83. K. L. Corwin, N. R. Newbury, J. M. Dudley, S. Coen, S. A. Diddams, B. R. Washburn, K. Weber, and R. S. Windeler, "Fundamental amplitude noise limitations to supercontinuum spectra generated in a microstructured fiber," Appl. Phys. B **77**, 269–277 (2003).

84. D. von der Linde, "Characterization of the noise in continuously operating mode-locked lasers," Appl. Phys. B **39**, 201–217 (1986).

85. H. A. Haus and A. Mecozzi, "Noise of mode-locked lasers," IEEE J. Quantum Electron. **29**, 983–996 (1993).

86. U. Demirbas, M. Schmalz, B. Sumpf, G. Erbert, G. S. Petrich, L. A. Kolodziejski, J. G. Fujimoto, F. X. Kärtner, and A. Leitenstorfer, "Femtosecond Cr:LiSAF and Cr:LiCAF lasers pumped by tapered diode lasers," Opt. Express **19**, 20444–20461 (2011).

87. U. Demirbas, D. Li, J. R. Birge, A. Sennaroglu, G. S. Petrich, L. A. Kolodziejski, F. X. Kärtner, and J. G. Fujimoto, "Low-cost, single-mode diode-pumped Cr:Colquiriite lasers," Opt. Express **17**, 14374–14388 (2009).

88. U. Demirbas, R. Uecker, D. Klimm, and J. Wang, "Low-cost, broadly tunable (375–433 nm & 746–887 nm) Cr:LiCAF laser pumped by one single-spatial-mode diode," Appl. Opt. **51**, 8440–8448 (2012).

89. P. C. Wagenblast, U. Morgner, F. Grawert, T. R. Schibli, F. X. Kärtner, V. Scheuer, G. Angelow, and M. J. Lederer, "Generation of sub-10-fs pulses from a Kerr-lens mode-locked Cr3+:LiCAF laser oscillator by use of third-order dispersion-compensating double-chirped mirrors," Opt. Lett. **27**, 1726–1728 (2002).

90. S. Uemura and K. Torizuka, "Generation of 12-fs pulses from a diode-pumped Kerr-lens mode-locked Cr:LiSAF laser," Opt. Lett. **24**, 780–782 (1999).

91. A. Chong, H. Liu, B. Nie, B. G. Bale, S. Wabnitz, W. H. Renninger, M. Dantus, and F. W. Wise, "Pulse generation without gain-bandwidth limitation in a laser with self-similar evolution," Opt. Express **20**, 14213–14220 (2012).

92. Y. Lan, Y. Song, M. Hu, B. Liu, L. Chai, and C. Wang, "Enhanced spectral breathing for sub-25 fs pulse generation in a Yb-fiber laser," Opt. Lett. **38**, 1292–1294 (2013).

93. N. Akhmediev and M. Karlsson, "Cherenkov radiation emitted by solitons in optical fibers," Phys. Rev. A **51**, 2602–2607 (1995).

94. P. K. A. Wai, C. R. Menyuk, Y. C. Lee, and H. H. Chen, "Nonlinear pulse propagation in the neighborhood of the zero-dispersion wavelength of monomode optical fibers," Opt. Lett. **11**, 464–466 (1986).

95. V. I. Karpman, "Radiation by solitons due to higher-order dispersion," Phys. Rev. E **47**, 2073–2082 (1993).

96. D. V. Skryabin, F. Luan, J. C. Knight, and P. S. J. Russell, "Soliton Self-Frequency Shift Cancellation in Photonic Crystal Fibers," Science **301**, 1705–1708 (2003).

97. J. N. Elgin, T. Brabec, and S. M. J. Kelly, "A perturbative theory of soliton propagation in the presence of third order dispersion," Opt. Commun. **114**, 321–328 (1995).

98. L. Tartara, I. Cristiani, and V. Degiorgio, "Blue light and infrared continuum generation by soliton fission in a microstructured fiber," Appl. Phys. B **77**, 307–311 (2003).

99. X. Liu, G. E. Villanueva, J. Laegsgaard, U. Moller, H. Tu, S. A. Boppart, and D. Turchinovich, "Low-Noise Operation of All-Fiber Femtosecond Cherenkov Laser," IEEE Photonics Technol. Lett. **25**, 892–895 (2013).

100. H. Tu and S. A. Boppart, "Optical frequency up-conversion by supercontinuum-free widely-tunable fiber-optic Cherenkov radiation," Opt. Express **17**, 9858–9872 (2009).

101. A. V. Mitrofanov, Y. M. Linik, R. Buczynski, D. Pysz, D. Lorenc, I. Bugar, A. A. Ivanov, M. V. Alfimov, A. B. Fedotov, and A. M. Zheltikov, "Highly birefringent silicate glass photonic-crystal fiber with polarization-controlled frequency-shifted output: A promising fiber light source for nonlinear Raman microspectroscopy," Opt. Express **14**, 10645–10651 (2006).

102. Y. Deng, F. Lu, and W. Knox, "Fiber-laser-based difference frequency generation scheme for carrier-envelope-offset phase stabilization applications," Opt. Express **13**, 4589–4593 (2005).

103. G. Chang, C.-H. Li, A. Glenday, G. Furesz, N. Langellier, L.-J. Chen, M. W. Webber, J. Lim, H.-W. Chen, D. F. Phillips, A. Szentgyorgyi, R. L. Walsworth, and F. X. Kärtner, "Spectrally flat, broadband visible-wavelength astro-comb," in *Conference on Lasers and Electro-Optics 2012*, OSA Technical Digest (online) (Optical Society of America, 2012), p. CF2C.4.

104. H. Tu and S. A. Boppart, "Ultraviolet-visible non-supercontinuum ultrafast source enabled by switching single silicon strand-like photonic crystal fibers," Opt. Express **17**, 17983–17988 (2009).

105. G. Chang, L.-J. Chen, and F. X. Kärtner, "Highly efficient Cherenkov radiation in photonic crystal fibers for broadband visible wavelength generation," Opt. Lett. **35**, 2361–2363 (2010).

106. G. Chang, L.-J. Chen, and F. X. Kärtner, "Fiber-optic Cherenkov radiation in the few-cycle regime," Opt. Express **19**, 6635–6647 (2011).

107. Q. Lin and G. P. Agrawal, "Raman response function for silica fibers," Opt. Lett. **31**, 3086–3088 (2006).

108. H.-W. Chen, H. Zia, J. Lim, G. Chang, and F. X. Kärtner, "Yb-fiber oscillator based, few-cycle ultrafast source at 850nm," in *2013 Conference on Lasers and Electro-Optics Pacific Rim (CLEO-PR)* (2013), pp. 1–2.

109. A. Chong, W. H. Renninger, and F. W. Wise, "Properties of normal-dispersion femtosecond fiber lasers," J. Opt. Soc. Am. B **25**, 140–148 (2008).

110. F. Ö. Ilday, J. R. Buckley, W. G. Clark, and F. W. Wise, "Self-Similar Evolution of Parabolic Pulses in a Laser," Phys. Rev. Lett. **92**, 213902 (2004).

111. A. Sell, G. Krauss, R. Scheu, R. Huber, and A. Leitenstorfer, "8-fs pulses from a compact Er:fiber system: quantitative modeling and experimental implementation," Opt. Express **17**, 1070 (2009).

112. A. Bartels, D. Heinecke, and S. A. Diddams, "Passively mode-locked 10 GHz femtosecond Ti:sapphire laser," Opt. Lett. **33**, 1905–1907 (2008).

113. L.-J. Chen, A. J. Benedick, J. R. Birge, M. Y. Sander, and F. Kärtner, "Octave-spanning, dual-output 2.166 GHz Ti:sapphire laser," Opt. Express **16**, 20699–20705 (2008).

114. R. R. Anderson and J. A. Parrish, "The Optics of Human Skin," J. Invest. Dermatol. **77**, 13–19 (1981).

115. J. H. Lee, J. van Howe, C. Xu, and X. Liu, "Soliton Self-Frequency Shift: Experimental Demonstrations and Applications," IEEE J. Sel. Top. Quantum Electron. **14**, 713–723 (2008).

116. H. Lim, J. Buckley, A. Chong, and F. W. Wise, "Fibre-based source of femtosecond pulses tunable from 1.0 to 1.3 μm," Electron. Lett. **40**, 1523–1525 (2004).

117. A. B. Fedotov, A. A. Voronin, I. V. Fedotov, A. A. Ivanov, and A. M. Zheltikov, "Powerful wavelength-tunable ultrashort solitons in a solid-core photonic-crystal fiber," Opt. Lett. **34**, 851–853 (2009).

118. J. Takayanagi, T. Sugiura, M. Yoshida, and N. Nishizawa, "1.0–1.7 μm Wavelength-Tunable Ultrashort-Pulse Generation Using Femtosecond Yb-Doped Fiber Laser and Photonic Crystal Fiber," IEEE Photonics Technol. Lett. **18**, 2284–2286 (2006).

119. M.-C. Chan, S.-H. Chia, T.-M. Liu, T.-H. Tsai, M.-C. Ho, A. A. Ivanov, A. M. Zheltikov, J.-Y. Liu, H.-L. Liu, and C.-K. Sun, "1.2- to 2.2-μm Tunable Raman Soliton Source Based on a Cr : Forsterite Laser and a Photonic-Crystal Fiber," IEEE Photonics Technol. Lett. **20**, 900–902 (2008).

120. J. P. Gordon, "Theory of the soliton self-frequency shift," Opt. Lett. **11**, 662–664 (1986).

121. A. A. Voronin and A. M. Zheltikov, "Soliton self-frequency shift decelerated by self-steepening," Opt. Lett. **33**, 1723–1725 (2008).

122. R. Pant, A. C. Judge, E. C. Magi, B. T. Kuhlmey, M. de Sterke, and B. J. Eggleton, "Characterization and optimization of photonic crystal fibers for enhanced soliton self-frequency shift," J. Opt. Soc. Am. B **27**, 1894–1901 (2010).

123. A. Bendahmane, O. Vanvincq, A. Mussot, and A. Kudlinski, "Control of the soliton self-frequency shift dynamics using topographic optical fibers," Opt. Lett. **38**, 3390–3393 (2013).

124. X.-H. Fang, M.-L. Hu, B.-W. Liu, L. Chai, C.-Y. Wang, H.-F. Wei, W.-J. Tong, J. Luo, C.-K. Sun, A. A. Voronin, and A. M. Zheltikov, "An all-photonic-crystal-fiber wavelength-tunable source of high-energy sub-100 fs pulses," Opt. Commun. **289**, 123–126 (2013).

125. J. M. Dudley, G. Genty, and S. Coen, "Supercontinuum generation in photonic crystal fiber," Rev. Mod. Phys. **78**, 1135–1184 (2006).

126. J. M. Dudley and S. Coen, "Coherence properties of supercontinuum spectra generated in photonic crystal and tapered optical fibers," Opt. Lett. **27**, 1180–1182 (2002).

127. J.-M. Dudley and S. Coen, "Numerical simulations and coherence properties of supercontinuum generation in photonic crystal and tapered optical fibers," IEEE J. Sel. Top. Quantum Electron. **8**, 651–659 (2002).

128. A. Ruehl, M. J. Martin, K. C. Cossel, L. Chen, H. McKay, B. Thomas, C. Benko, L. Dong, J. M. Dudley, M. E. Fermann, I. Hartl, and J. Ye, "Ultrabroadband coherent supercontinuum frequency comb," Phys. Rev. A **84**, 011806 (2011).

129. J. N. Ames, S. Ghosh, R. S. Windeler, A. L. Gaeta, and S. T. Cundiff, "Excess noise generation during spectral broadening in a microstructured fiber," Appl. Phys. B **77**, 279–284 (2003).

130. G. Genty, S. Coen, and J. M. Dudley, "Fiber supercontinuum sources (Invited)," J. Opt. Soc. Am. B **24**, 1771–1785 (2007).

131. F. Lu and W. H. Knox, "Generation of a broadband continuum with high spectral coherence in tapered single-mode optical fibers," Opt. Express **12**, 347 (2004).

132. K. Tai, A. Hasegawa, and A. Tomita, "Observation of modulational instability in optical fibers," Phys. Rev. Lett. **56**, 135–138 (1986).

133. U. Bandelow and A. Demircan, "Impact of the modulation instability on supercontinuum generation," in *2005 Conference on Lasers and Electro-Optics Europe, 2005. CLEO/Europe* (2005), p. 390.

134. F. W. Wise, A. Chong, and W. H. Renninger, "High-energy femtosecond fiber lasers based on pulse propagation at normal dispersion," Laser Photonics Rev. **2**, 58–73 (2008).

135. K. Kieu, W. H. Renninger, A. Chong, and F. W. Wise, "Sub-100 fs pulses at watt-level powers from a dissipative-soliton fiber laser," Opt. Lett. **34**, 593–595 (2009).

136. B. Ortaç, M. Baumgartl, J. Limpert, and A. Tünnermann, "Approaching microjoule-level pulse energy with mode-locked femtosecond fiber lasers," Opt. Lett. **34**, 1585–1587 (2009).

137. M. Baumgartl, B. Ortaç, C. Lecaplain, A. Hideur, J. Limpert, and A. Tünnermann, "Sub-80 fs dissipative soliton large-mode-area fiber laser," Opt. Lett. **35**, 2311–2313 (2010).

138. S. Lefrançois, K. Kieu, Y. Deng, J. D. Kafka, and F. W. Wise, "Scaling of dissipative soliton fiber lasers to megawatt peak powers by use of large-area photonic crystal fiber," Opt. Lett. **35**, 1569–1571 (2010).

139. Chi-Hung Liu, Guoqing Chang, Natasha Litchinister, Doug Guertin, Nick Jacobson, Kanishka Tankala, and Almantas Galvanauskas, "Chirally Coupled Core Fibers at 1550-nm and 1064-nm for Effectively Single-Mode Core Size Scaling," in *Conference on Lasers and Electro-Optics/Quantum Electronics and Laser Science Conference and Photonic Applications Systems Technologies*, OSA Technical Digest Series (CD) (Optical Society of America, 2007), p. CTuBB3.

140. A. Galvanauskas, M. C. Swan, and C.-H. Liu, "Effectively Single-Mode Large Core Passive and Active Fibers with Chirally Coupled-Core Structures," in *Conference on Lasers and Electro-Optics/Quantum Electronics and Laser Science Conference and Photonic Applications Systems Technologies*, OSA Technical Digest (CD) (Optical Society of America, 2008), p. CMB1.

141. C.-H. Liu, S. Huang, C. Zhu, and A. Galvanauskas, "High Energy and High Power Pulsed Chirally-Coupled Core Fiber Laser System," in *Advanced Solid-State Photonics*, OSA Technical Digest Series (CD) (Optical Society of America, 2009), p. MD2.

142. S. Huang, C. Zhu, C.-H. Liu, X. Ma, C. Swan, and A. Galvanauskas, "Power Scaling of CCC Fiber Based Lasers," in *Conference on Lasers and Electro-Optics/International Quantum Electronics Conference*, OSA Technical Digest (CD) (Optical Society of America, 2009), p. CThGG1.

143. R. Szipöcs, C. Spielmann, F. Krausz, and K. Ferencz, "Chirped multilayer coatings for broadband dispersion control in femtosecond lasers," Opt. Lett. **19**, 201–203 (1994).

144. V. Pervak, C. Teisset, A. Sugita, S. Naumov, F. Krausz, and A. Apolonski, "High-dispersive mirrors for femtosecond lasers," Opt. Express **16**, 10220–10233 (2008).

145. T. Suedmeyer, S. Marchese, S. Hashimoto, C. Baer, G. Gingras, B. Witzel, and U. Keller, "Femtosecond laser oscillators for high-field science," Nat. Photonics **2**, 599–604 (2008).

146. V. Pervak, I. Ahmad, S. A. Trushin, Z. Major, A. Apolonski, S. Karsch, and F. Krausz, "Chirped-pulse amplification of laser pulses with dispersive mirrors," Opt. Express **17**, 19204–19212 (2009).

147. J. R. Birge and F. X. Kärtner, "Phase distortion ratio: alternative to group delay dispersion for analysis and optimization of dispersion compensating optics," Opt. Lett. **35**, 2469–2471 (2010).

148. J. W. Nicholson, A. D. Yablon, S. Ramachandran, and S. Ghalmi, "Spatially and spectrally resolved imaging of modal content in large-mode-area fibers," Opt. Express **16**, 7233–7243 (2008).

149. M. Baumgartl, C. Lecaplain, A. Hideur, J. Limpert, and A. Tünnermann, "Fiber Oscillator producing 91fs Pulses with 0.8μJ at 60W of Average Power," in *Lasers, Sources, and Related Photonic Devices*, OSA Technical Digest (CD) (Optical Society of America, 2012), p. AT1A.2.

150. X. Ma, C.-H. Liu, G. Chang, and A. Galvanauskas, "Angular-momentum coupled optical waves in chirally-coupled-core fibers," Opt. Express **19**, 26515–26528 (2011).

151. S. Lefrancois, T. S. Sosnowski, C.-H. Liu, A. Galvanauskas, and F. W. Wise, "Energy scaling of mode-locked fiber lasers with chirally-coupled core fiber," Opt. Express **19**, 3464–3470 (2011).

152. C. Zhu, I.-N. Hu, X. Ma, L. Siiman, and A. Galvanauskas, "Single-frequency and single-transverse mode Yb-doped CCC fiber MOPA with robust polarization SBS-free 511W output," in *Advances in Optical Materials*, OSA Technical Digest (CD) (Optical Society of America, 2011), p. AMC5.

153. A. Chong, J. Buckley, W. Renninger, and F. Wise, "All-normal-dispersion femtosecond fiber laser," Opt. Express **14**, 10095–10100 (2006).

154. X. Liu, "Numerical and experimental investigation of dissipative solitons in passively mode-locked fiber lasers with large net-normal-dispersion and high nonlinearity," Opt. Express **17**, 22401–22416 (2009).

155. H. A. Haus, "Mode-locking of lasers," IEEE J. Sel. Top. Quantum Electron. **6**, 1173–1185 (2000).

156. T. Schreiber, B. Ortaç, J. Limpert, and A. Tünnermann, "On the study of pulse evolution in ultra-short pulse mode-locked fiber lasers by numerical simulations," Opt. Express **15**, 8252–8262 (2007).

157. K. M. Spaulding, D. H. Yong, A. D. Kim, and J. N. Kutz, "Nonlinear dynamics of mode-locking optical fiber ring lasers," J. Opt. Soc. Am. B **19**, 1045–1054 (2002).

158. O. V. Sinkin, R. Holzlohner, J. Zweck, and C. R. Menyuk, "Optimization of the Split-Step Fourier Method in Modeling Optical-Fiber Communications Systems," J. Light. Technol. **21**, 61 (2003).

159. Y. Logvin and H. Anis, "Similariton pulse instability in mode-locked Yb-doped fiber laser in the vicinity of zero cavity dispersion," Opt. Express **15**, 13607–13612 (2007).

160. K. Tamura, E. P. Ippen, H. A. Haus, and L. E. Nelson, "77-fs pulse generation from a stretched-pulse mode-locked all-fiber ring laser," Opt. Lett. **18**, 1080–1082 (1993).

161. T. Lei, F. Lu, C. Tu, Y. Deng, and E. Li, "Numerical study on self-similar pulses in mode-locking fiber laser by coupled Ginzburg-Landau equation model," Opt. Express **17**, 585–591 (2009).

162. M. A. Abdelalim, Y. Logvin, D. A. Khalil, and H. Anis, "Properties and stability limits of an optimized mode-locked Yb-doped femtosecond fiber laser," Opt. Express **17**, 2264–2279 (2009).